AN ABSTRACT OF THE
DISSERTATION OF

Heather M. Benway for the degree of Doctor of Philosophy in Oceanography presented on July 21, 2005.
Title: Modern and Past Climate Variability in the Eastern Pacific Warm Pool

Redacted for privacy

Abstract approved: _____
Alan C. Mix

Westward transport of water vapor across the Panama Isthmus helps to maintain the salinity contrast between the Atlantic and Pacific Oceans, important in thermohaline circulation and global climate. Relatively low sea-surface salinities and a strong, shallow pycnocline in the eastern Pacific warm pool (EPWP) region near Central America reflect high net precipitation. This dissertation includes a detailed analysis of the modern EPWP moisture budget, the development and application of a new technique for measuring Mg/Ca in fossil foraminifera, a commonly used paleotemperature proxy, and high resolution multi-proxy reconstructions of temperature, salinity, and pycnocline changes in the EPWP during key Pleistocene and Pliocene intervals.

A combination of meteorological data and oxygen isotope measurements of seawater and rainwater reveal primary moisture sources for the EPWP region. In addition to a northeasterly cross-isthmus component that is more dominant during boreal winter, southwesterly transport of local Pacific moisture prevails during boreal summer. Sensitivity tests indicate that the EPWP is most sensitive to changes in the average isotopic composition of rainfall, which is primarily controlled by the relative contributions of these moisture sources. This analysis of the modern moisture budget provides important constraints on the interpretation of paleoceanographic reconstructions from the EPWP.

Mg/Ca paleothermometry has played a pivotal role in developing temperature and salinity reconstructions in the EPWP. The commonly used batch method for Mg/Ca measurement is plagued by problems of dissolution and calcite phases that contaminate the environmental signal recorded in primary calcite. Here, the application of an alternative method involving flow-through technology to the measurement of foraminiferal Mg/Ca has provided the opportunity to monitor heterogeneity of Mg in foraminiferal calcite, and thus to isolate the Mg/Ca ratio of primary calcite.

This new Mg/Ca technology combined with stable isotope ($\delta^{18}O$) measurements of fossil foraminifera has yielded high resolution temperature and salinity reconstructions from sites in the EPWP for the late Pleistocene (0-30 ka), as well as key intervals spanning the mid-Pleistocene transition and the tectonic closure of the Panama Isthmus. These paleorecords provide compelling evidence of a climatic linkage between the tropics and the high latitudes involving vapor transport and deep ocean circulation.

©Copyright by Heather M. Benway
July 21, 2005
All Rights Reserved

Modern and Past Climate Variability in the Eastern Pacific Warm Pool

by
Heather M. Benway

A DISSERTATION

submitted to

Oregon State University

in partial fulfillment of
the requirements for the
degree of

Doctor of Philosophy

Presented July 21, 2005
Commencement June 2006

Doctor of Philosophy dissertation of Heather M. Benway presented on July 21, 2005.

APPROVED:

Redacted for privacy

Major Professor, representing Oceanography

Redacted for privacy

Dean of the College of Oceanic and Atmospheric Sciences

Redacted for privacy

Dean of the Graduate School

I understand that my dissertation will become part of the permanent collection of Oregon State University libraries. My signature below authorizes release of my dissertation to any reader upon request.

Redacted for privacy

Heather M. Benway, Author

ACKNOWLEDGMENTS

Firstly, I thank my advisor Alan Mix for being a true mentor and setting a fine example as a scientist and an educator. His boundless energy and enthusiasm for science is contagious. I appreciate his faith in me and his unwavering commitment to my development as a scientist.

I would like to thank my other committee members Gary Klinkhammer, Nick Pisias, Eric Maloney, and Steve Hostetler, as well as my graduate representative Dan Schafer. For all of the letters of recommendation, impromptu chats, paper reviews, long committee meetings, sound advice, and most importantly, for taking the time to do great science with me, I am very grateful to you all. Thanks especially to Nick for his endless reserve of patience when explaining statistics to me.

There are so many people in COAS who have contributed to this work and enriched my time here. For laboratory assistance and for taking the time to teach me how to be an even more anal geochemist, I thank Bill Rugh and Andy Ungerer, two of the most stellar faculty research assistants I've ever had the privilege of working with. They helped generate data shown throughout this entire dissertation. I learned micropaleontology from the masters, Maziet Cheseby and June Padman. Their guidance, patience, and friendship have been a tremendous source of comfort to me. Brian Haley, an endless source of wit and entertainment, helped generate the Mg/Ca data in Chapters 3 and 4. Andy Ross helped generate the Mg/Ca data in Chapters 4 and 5. For the GMT crash course and the maps shown in Chapters 2, 4, and 5, I thank Jason Chaytor. Chris Chickadel provided much needed Matlab guidance in Chapter 4. Molly Phipps, Stacy Kish, and many wonderful undergraduate work study students helped me wash samples. Marta Torres, Luis Torres, and Clayton Paulson helped me obtain seawater and rainwater samples for Chapter 2. For her review of Chapter 2 and many thoughtful conversations, I thank Kelly Falkner. Andreas Schmittner provided very insightful comments on Chapter 4. I thank Joe Stoner for many helpful and fun discussions about my data. Jane Fleischbein provided much time and assistance with

the Autosal. For his guidance in the Electron Microprobe Laboratory, which was a critical piece of Chapter 3, I thank Roger Nielson. I would also like to thank the shipboard participants of the NEMO-3 expedition (May-June 2000) and Ocean Drilling Program Leg 202 (April-June 2002). These cruises provided much of the material on which my dissertation is based.

I won't list all of the people who have blessed me with their friendships over the past 5 years, as I fear that I may forget a name. I am confident that you know who you are. You have all brought hope, meaning, and wonderful, necessary distractions into my world. I moved to Oregon five years ago, thousands of miles away from all that was familiar to me, and I have found a group of friends here that I am proud to call family.

My parents have been a continual source of support throughout this difficult and seemingly endless journey. Their love, wisdom, and encouragement have kept me going, and more importantly, they have helped me see the worth in who I am, not just in what I do. I love them dearly and hope to someday be such a source of comfort and wisdom to my own children.

Finally, for giving me the best reason in the world to come home at the end of the day, I thank Matthew, my best-friend/fiancé/life-partner/awesome-cook/voice-of-reason/inspiration and so many other things, Daisy, my favorite hiking partner and the BEST DOG EVER, and my charming little assassin parrot, Shasta. I love and treasure every moment with them, and my sanctuary will always be wherever they are.

CONTRIBUTION OF AUTHORS

Dr. Alan Mix was involved with all aspects of data analysis, interpretation, and publication of every chapter of this dissertation. Drs. Gary Klinkhammer and Brian Haley assisted with Mg/Ca measurements, data analysis, and publication of Chapters 3 and 4.

TABLE OF CONTENTS

TABLE OF CONTENTS (Continued)

LIST OF FIGURES

LIST OF FIGURES (Continued)

LIST OF APPENDICES

Modern and Past Climate Variability in the Eastern Pacific Warm Pool

1. INTRODUCTION

Instrumental and historical records of climate variability have greatly improved our understanding of seasonal/interannual to decadal climate rhythms in the earth system such as the El Niño/Southern Oscillation (ENSO), the North Atlantic Oscillation, and the Pacific Decadal Oscillation. Although these are dominant features of the modern climate system, the current state of knowledge on natural climate variability is not adequate to reliably predict future changes, particularly in an earth system that is being further influenced by anthropogenic activity. The field of paleoclimatology, based on the study of environmental archives from ice cores, marine and lacustrine sediments, tree-rings, corals, etc., has extended our knowledge of climate variability well beyond the temporal confines of the instrumental record, providing the opportunity to study longer period rhythms in the earth system, such as the orbital pacing of the ice ages. With the ultimate goals of understanding and predicting the interaction of the earth's various natural rhythms as well as anthropogenic changes, we must continue to broaden our temporal and spatial perspectives through the continued development of instrumental and paleoclimate archives.

Study Area and Climatic Significance

Changes in the eastern tropical Pacific surface ocean are strongly linked to variability in low latitude Atlantic freshwater export via the Panama Isthmus, Intertropical Convergence Zone (ITCZ) dynamics, and long-term El Niño/Southern Oscillation (ENSO) behavior. These processes all represent dominant features of modern tropical climatology, some rendering widespread extra-tropical climatic effects. However, very little is known about how these processes have varied on longer time scales and what their role has been in large-scale climate and ocean circulation changes of the past.

This dissertation focuses on identifying moisture sources and reconstructing surface ocean changes in the eastern Pacific warm pool (EPWP) region off the west coast of Central America. Currently, high net precipitation (Precipitation-Evaporation, or P-E) maintains a low surface salinity (~32-33 PSU) and a strong, shallow pycnocline in the EPWP region. Northeasterly trade winds carry evaporated moisture from the Caribbean and tropical Atlantic across the Panama Isthmus and into the EPWP, where atmospheric convection and heavy rainfall impart a measurable signature in the upper ocean. A positive feedback scenario develops as the upper ocean becomes more stable due to increased rainfall, sea surface temperatures (SSTs) rise in response to solar heating, and the warm SSTs attract moist air masses, setting the stage for increased convection (Magaña et al., 1999). The sensitivity of the EPWP to atmospheric forcing makes this region ideal for reconstructing upper ocean salinity changes related to cross-isthmus vapor transport.

Westward transport of water vapor across the Panama Isthmus helps to maintain the salinity contrast between the Atlantic and Pacific Oceans, a key driver of global thermohaline circulation (Zaucker and Broecker, 1992; Zaucker et al., 1994). Marine sediment records have shown evidence of strong linkages between disruptions of thermohaline circulation and large millennial-scale temperature changes of the past. Although melt water from high latitude glaciers has straightforward effects on the density-driven deep ocean circulation, very few studies have identified low latitude processes that might affect this circulation. Careful examination of these processes, as well as feedbacks between high and low latitudes will gradually improve our understanding of the role of thermohaline circulation in global climate.

Moisture Budget

A critical part of this dissertation is the development of a moisture budget for the EPWP region based on meteorological data, salinity, and oxygen isotope measurements of seawater and rainwater from the eastern tropical Pacific. During boreal summer, the ITCZ is positioned north of the equator, and strengthened

southeasterly trade winds curl as they cross the equator, delivering Pacific moisture via the southwesterly Choco Jet to the EPWP region (Martínez et al., 2003). In boreal winter, the ITCZ migrates southward, and northeasterly trade winds intensify and deliver Atlantic moisture to the EPWP region. Sensitivity tests of the modern $\delta^{18}O$-S relationship elucidate the relative roles of advection, river input, and precipitation in the modern EPWP moisture budget, and provide important constraints on the interpretation of paleosalinity reconstructions from the EPWP.

Multi-Proxy Approach

In this dissertation, a host of chemical measurements of foraminiferal shells preserved in marine sediments from the EPWP are used to reconstruct changes in sea-surface salinity and temperature. Two sediment cores from the same site provide well-preserved replicate records sampled at high resolution over the past 30,000 years.

Oxygen isotope measurements of fossil foraminifera are the basis for one of the most well established proxies in the field of paleoceanography. The oxygen isotope composition of foraminiferal calcite depends on both the temperature and the isotopic composition of the seawater ($\delta^{18}O_{sw}$) in which the organism calcified. $\delta^{18}O_{sw}$ is a conservative tracer that is modified on short time scales by physical processes such as evaporation, precipitation, advection, mixing, and river runoff, and on long time scales by the waxing and waning of ice sheets that change global ocean $\delta^{18}O$ budgets. Since the deep ocean is less variable (in temperature and salinity) through time than the upper ocean, oxygen isotope records from benthic foraminifera are typically dominated by these global fluctuations in ice volume. Therefore, benthic records from completely different parts of the world often show relatively consistent and predictable marine isotope stages, or periods of alternating warm and cold conditions. Radiocarbon dating and benthic isotope stratigraphy are two of the most powerful and commonly used paleoceanographic tools for age model development. In addition to ice volume, oxygen isotope records from planktonic foraminifera contain regional information about temperature and salinity changes in the upper ocean. Multi-species

reconstructions based on planktonic species that live at different depths in the water column are also useful for assessing changes in upper ocean structure. Here, dual measurements of a surface- and a thermocline-dwelling species reveal changes in pycnocline structure through time.

Paleosalinity reconstructions require independent estimates of temperature to deconvolve temperature and watermass ($\delta^{18}O_{sw}$) effects on $\delta^{18}O_c$. A fundamental part of developing temperature and salinity reconstructions from the EPWP has involved the development and application of a new technique for measuring Mg/Ca in fossil foraminifera, a commonly used paleotemperature proxy. The commonly used "batch method" for Mg/Ca measurement is plagued by problems of dissolution and calcite phases that contaminate the environmental signal recorded in primary calcite. An alternative method involving flow-through technology combines ion chromatography and inductively coupled plasma mass spectrometry (ICP-MS) in a series of cleaning and dissolution reactions monitored continuously with time-resolved analysis (TRA). This combination of slow, controlled dissolution and TRA provides a unique opportunity to closely monitor the removal of contaminant phases and assess heterogeneity of Mg in foraminifera, and thus to isolate the Mg/Ca ratio of primary calcite. This new Mg/Ca technology combined with stable isotope ($\delta^{18}O$) measurements of fossil foraminifera has yielded high resolution temperature and salinity reconstructions from the EPWP region spanning the past 30,000 years. Careful comparison of EPWP multi-proxy reconstructions to paleoclimate records from the Caribbean Sea, tropical and subtropical North Atlantic Ocean, and polar ice cores provides important insights into the role of vapor transport in millennial-scale temperature and deep ocean circulation changes.

Closure of the Panama Isthmus

A number of paleoclimate studies have focused on the closure of the Panama Isthmus and subsequent changes in global ocean circulation and northern hemisphere climate. Marine sediments from the eastern tropical Pacific (Shackleton et al., 1995;

Haug and Tiedemann, 1998), the Caribbean (Haug and Tiedemann, 1998), the equatorial west Atlantic (Tiedemann and Franz, 1997), and the Labrador Sea (Arthur et al., 1989) have all shown evidence of increased thermohaline circulation starting ~4.6 Ma, which coincides with the final stage of Isthmus closure. Modeling studies (Maier-Reimer et al., 1990; Mikolajewicz and Crowley, 1997) have further supported these findings. Changes in deep water formation can have a marked effect on global climate (Manabe and Stouffer, 1988). A stronger Gulf Stream (Kaneps, 1979) following the closure is thought to have transported warm, salty water to the high latitudes, which initiated North Atlantic Deep Water formation in the Labrador Sea. Increased Eolian grain size in the eastern tropical Pacific during both the mid-Pliocene closure of the Isthmus and the late Pliocene intensification of northern hemisphere glaciation (Hovan, 1991) suggests stronger trade winds during these times, which could have increased westward vapor transport.

Evidence of linkages between Isthmus closure and the initial onset of northern hemisphere glaciation ~3 Ma has also been identified in sites from the North Atlantic, eastern equatorial Pacific, and Caribbean (Shackleton et al., 1984; Shackleton et al., 1995; Haug and Tiedemann, 1998; Driscoll and Haug, 1998). Despite a considerable time lag between the initiation of NADW formation and the first northern hemisphere glaciation, Haug and Tiedemann (1998) argued that the closure of the Panama Isthmus provided the necessary increase in moisture supply to the high northern latitudes to gradually sustain a full glaciation. Driscoll and Haug (1998) proposed a mechanism involving sea ice formation and a gradual increase in obliquity (amplitude) to explain how increased northward heat transport associated with thermohaline circulation could eventually lead to a glaciation.

This dissertation includes multi-proxy reconstructions from the EPWP for brief Pliocene time slices spanning the final closure of the Panama Isthmus. Assessing the details of this closure based on the oceanographic effects in the EPWP region serves as a "fingerprint" for low latitude processes such as cross-isthmus vapor transport and

provides further constraints on the role of such processes in the northern hemisphere climate and global ocean circulation changes that followed the final isthmus closure.

2. OXYGEN ISOTOPES, UPPER-OCEAN SALINITY, AND PRECIPITATION SOURCES IN THE EASTERN TROPICAL PACIFIC

Heather M. Benway and Alan C. Mix

Earth and Planetary Science Letters
http://www.elsevier.com/locate/epsl
Volume 224 (2004), pp. 493-507

Abstract

Westward transport of freshwater across the Panama Isthmus helps to maintain the salinity (S) contrast between the Atlantic and Pacific Oceans, important in global thermohaline circulation and climate. Relatively low sea-surface salinities in the Panama Bight reflect high net precipitation. We infer sources of this freshwater input to the region based on oxygen isotopes ($\delta^{18}O$) of precipitation (δ_P) and seawater (δ_{SW}). The primary trend of the surface water δ_{SW}-S relationship implies a freshwater endmember $\delta^{18}O$ of -8.5 ± 0.3 ‰, significantly lower than the mean δ_P of rainwater we measured in the region (-4.8 ± 1.8 ‰), mixing with waters upwelled from the subsurface (S= 34.9 to 35.1 PSU, δ_{SW} = 0.3 to 0.4 ‰). Based on limited isotope and salinity data, these upwelling waters are a mixture of ~60% tropical waters, and ~40% subtropical mode waters. Three secondary trends in the surface water δ_{SW}-S distribution point to similar freshwater sources with $\delta^{18}O$ of -2.5 ± 1.2 ‰, -4.7 ± 0.5 ‰, and -4.8 ± 0.6 ‰, consistent with local precipitation sources. Accounting for the primary surface water trend, intermittent cross-isthmus transport of moist air masses from the Caribbean may introduce relatively ^{18}O-depleted rainfall due to a combination of recycling and orographic distillation. In addition, relatively infrequent but large tropical storms, which may contain freshwater of both Pacific and Caribbean origin, deliver rainfall with δ_P of -10 to -14 ‰. The primary trend of regional surface seawater data, which integrates the different sources over time, suggests that about half of the total precipitation reflects local sources, and half reflects a combination of cross-isthmus transport and large storms. The regional δ_{SW}-S distribution is sensitive to the relative contributions of these freshwater sources, which may change under different climate regimes.

Introduction

Net export of freshwater in the form of water vapor from the Atlantic Ocean Basin maintains the relatively high salinities needed for North Atlantic Deep Water formation (Broecker et al., 1990; Broecker, 1991; Zaucker and Broecker, 1992;

Zaucker et al., 1994). A significant portion of this net freshwater transport occurs across the Panama Isthmus (Oort, 1983; Weyl, 1968). Here, low-level (>850 mb) northeasterly winds transport water vapor from Atlantic and Caribbean sources into the eastern tropical Pacific, where it rains out (Joussaume et al., 1986). Estimates of this net freshwater transport based on modern atmospheric general circulation model (AGCM) simulations and climatologic data range from 0.13 Sv (Zaucker and Broecker, 1992) to 0.45 Sv (Baumgartner and Reichel, 1975; Manabe and Stouffer, 1988) (1 Sv = 10^6 m^3s^{-1}).

Even small changes in the transfer of freshwater across the Panama Isthmus associated with different climate regimes could affect the salt balance between the Atlantic and Pacific Oceans and influence global deep-ocean circulation, including the possible shut-down of North Atlantic Deep Water formation (Zaucker et al., 1994; Rahmstorf, 1996; Ganopolski and Rahmstorf, 2001; Schmittner et al., 2002; Schmittner and Clement, 2002). Some models suggest that relatively high Atlantic freshwater export occurs across the Panama Isthmus during El Niño events (ENSO warm phases) (Schmittner et al., 2000; Schmittner and Clement, 2002). If so, long-term variations (on the order of decades) in El Niño frequency could have global impacts through their role in modifying the distribution of salinity among ocean basins.

On longer time scales, enhanced water vapor transport during glacial periods could explain why long-term variations of Pleistocene $\delta^{18}O$ values of planktonic foraminifera in sediments from the Pacific have relatively low-amplitudes compared to those from the Atlantic Ocean (Broecker, 1989). In agreement with this concept, an AGCM simulation of the Last Glacial Maximum (LGM) suggested that increased wind speeds would support a two- to four-fold increase in net westward transport of water vapor across the Panama Isthmus relative to a modern simulation (Hostetler and Mix, 1999). In apparent conflict with this finding, an LGM simulation with a coupled two-dimensional ocean-energy balance atmosphere model yielded reduced Atlantic

freshwater export relative to present (Schmittner et al., 2002). Long-term changes in cross-isthmus water vapor transport remain uncertain.

To resolve this conflict and improve understanding of vapor transport processes associated with large-scale climate changes, measurements of paleosalinity are needed. Such estimates typically rely on measurements of oxygen isotopes ($\delta^{18}O$) in fossil shells, which reflect both temperature effects and the $\delta^{18}O$ of ambient seawater (δ_{SW}). Like salinity, δ_{SW} is a conservative tracer that is modified on short time scales by physical processes such as evaporation, precipitation, advection, mixing, and river runoff (Craig and Gordon, 1965), and on long time scales by the waxing and waning of ice sheets that change whole-ocean $\delta^{18}O$ budgets (Emiliani, 1955). All of these processes may vary independently of each other through space and time, so the relationship between δ_{SW} and S may also vary. Such variability in the δ_{SW}-S relationship provides useful clues to the sources and transports of water, but also is a possible problem for paleosalinity calculations if there is uncertainty about which δ_{SW}-S relationship to use. Here we provide new measurements of $\delta^{18}O$ in precipitation (δ_P) and seawater (δ_{SW}) in the Panama Bight and eastern tropical Pacific region, to assess the relative roles of advection, river input, and precipitation in determining the modern δ_{SW}-S relationship, and with this background we use model calculations to assess the likely errors on paleosalinity estimates in the region.

Methods and Data

Climatological monthly precipitation and latent heat fluxes for the Panama Bight region (1°-10° N; 75°-90° W) were obtained from the NCEP/NCAR Reanalysis (1.9° latitude x 1.9° longitude grids) provided by the NOAA/CIRES Climate Diagnostics Center (http://www.cdc.noaa.gov/). We converted the NCEP latent heat fluxes to evaporation rates using the latent heat of vaporization for water (2.25×10^6 J/kg). The annual mean precipitation minus evaporation (P-E) (Fig. 1a) was calculated by first averaging the mean monthly precipitation and evaporation data and then calculating the difference field (P-E).

We obtained marine- and land-based rainwater samples from the eastern tropical Pacific (Fig. 2.1a) intermittently over the period of about one year (September 2001 – June 2002). A simple manual rainwater trap employed a Nalgene^{TM} bottle topped with a narrow-mouthed funnel (to minimize evaporation). At sea, the trap was mounted on a forward rail, above the bridge, to avoid contamination with stack gases and to minimize the influence of sea spray. On land, the trap was positioned away from trees, rooftops, or any other potential sources of contamination. Glass sample vials were filled and sealed with screw-caps topped with Parafilm^{TM} as soon as possible after each rain event (<24 hr), and the collection device was emptied, so as not to mix samples between rain events.

Land-based rainwater samples were collected throughout October and November 2001 from two sites in Costa Rica: 1) Sarapiquí, near the Caribbean coast of Costa Rica (10°17'N, 84°01'W, elevation 30 m); and 2) San Jose, in the mountains near the Pacific coast of Costa Rica (9°59'N, 84°04'W, elevation 1200 m).

Marine-based rainwater samples come from two cruises, the EPIC survey (Eastern Pacific Investigation of Climate Processes in the Coupled Ocean-Atmosphere System, R/V New Horizon) in September-October of 2001, and Ocean Drilling Program Leg 202 (D/V JOIDES Resolution) in May of 2002. The EPIC cruise sampled a latitudinal transect (1° S -11° N) at 95° W at the western edge of the Panama Bight, while the ODP Leg 202 samples ranged from just off the Costa Rican coast to ~86° W (Fig. 2.1a).

We obtained seawater samples (Fig. 2.1b) from the Panama Bight region (here defined broadly to include latitudes from the equatorial cold tongue at 1.8° S to the Gulf of Tehuantepec at 15.7° N) in May and June of 2000 during the NEMO expedition (New Millennium of Oceanography, R/V Melville), and along 95° W from 1° S to 11° N in September and October of 2001 during the EPIC survey. On the NEMO expedition, seawater samples were collected from Niskin bottle casts at ~2 m and ~50-400 m. On the EPIC survey, surface seawater was sampled from the ship's continuously flowing seawater pump (nominal depth ~4 m). From both cruises,

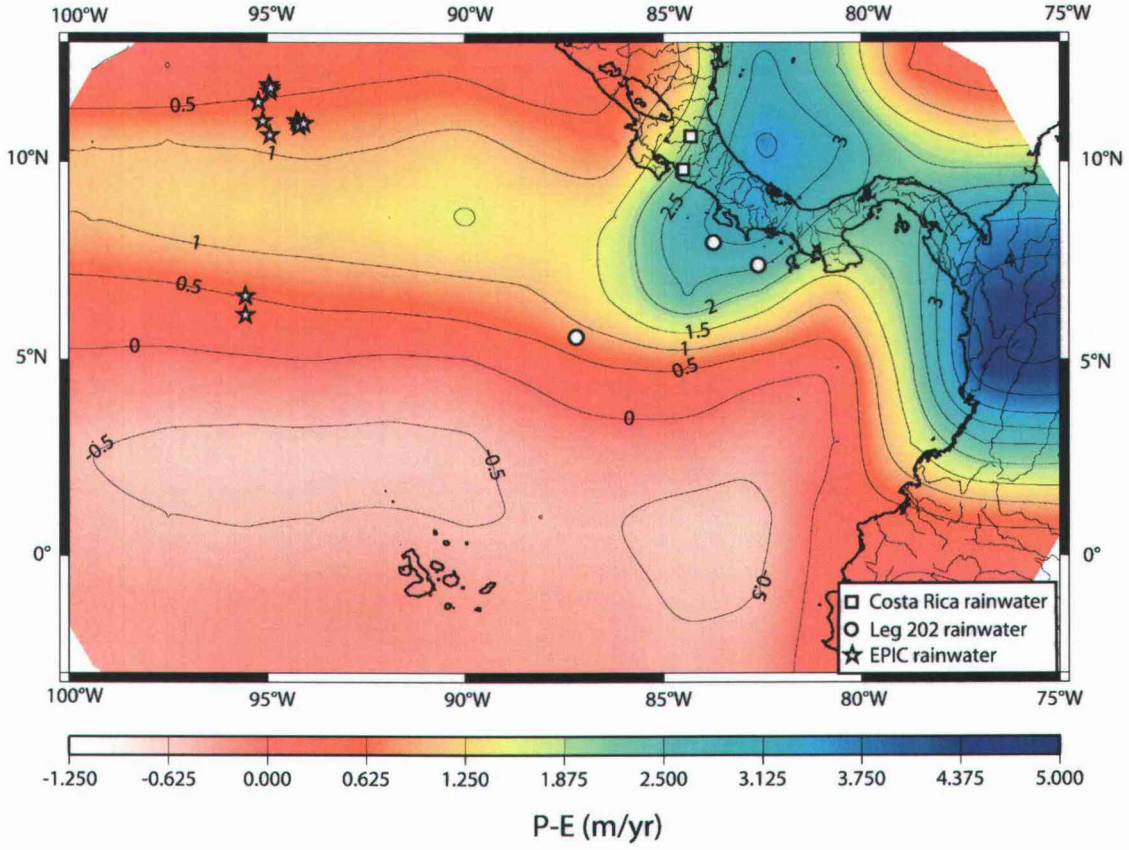

Figure 2.1. a. Annual mean precipitation – evaporation (P-E) based on NCEP/NCAR Reanalysis long-term monthly average precipitation rates and latent heat fluxes. Symbols indicate locations of rainwater samples. Satellite-borne (Quikscat) wind vectors for the Panama Bight are available in Rodríguez-Rubio et al. (2003).

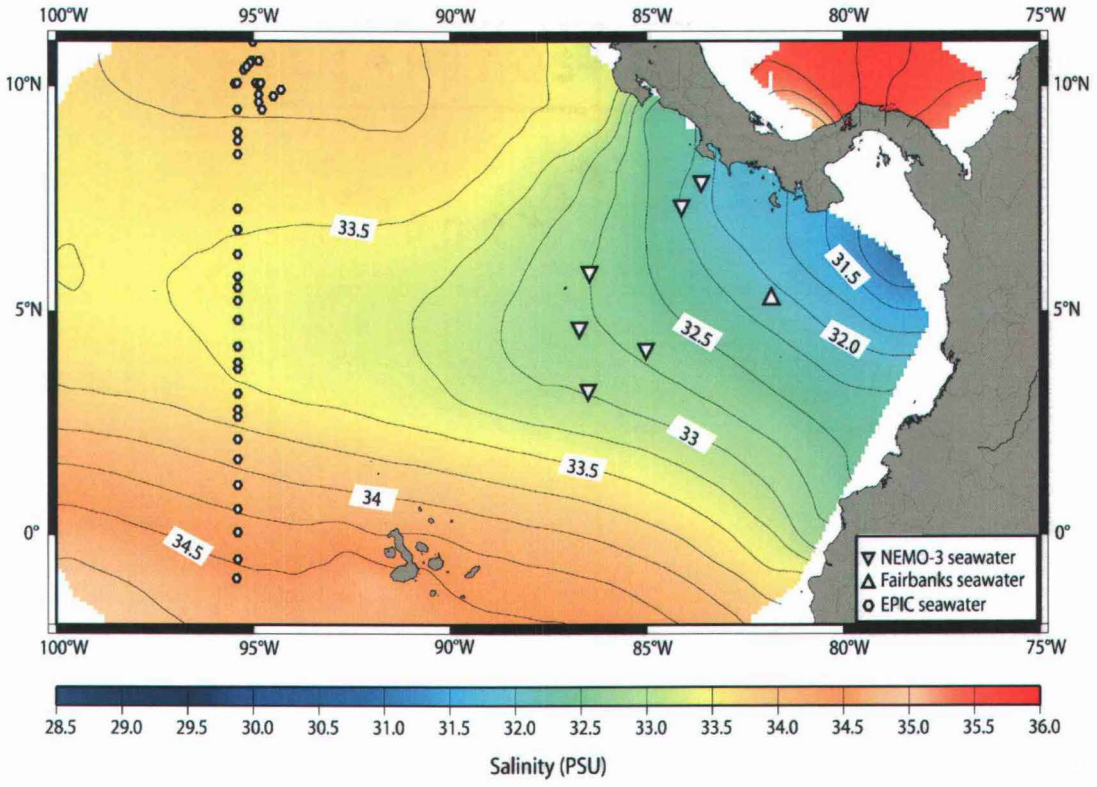

Figure 2.1. b. Annual mean sea-surface salinities (PSU) from Boyer et al. (1998). Symbols indicate locations of seawater samples. Mean geostrophic currents for the Panama Bight region are available in Kessler (2002) (calculated from XBT data) and Rodríguez-Rubio et al. (2003) (calculated from satellite data).

seawater samples were sealed in glass vials similar to the precipitation samples, filled carefully with some overflow to avoid air bubbles. The secondary seal of Parafilm^{TM} kept the caps tightly closed and provided a further barrier to evaporation.

Salinity measurements of discrete seawater samples were made using a Guildline 8400 AutoSal salinometer at Oregon State University. Precision of salinity measurements is ±0.01 PSU. Standardization is based on IAPSO (International Association for the Physical Sciences of the Ocean) seawater supplied by Ocean Scientific International.

δ_P and δ_{SW} (reported relative to V-SMOW, Vienna - Standard Mean Ocean Water) were measured using an on-line automated CO_2-water equilibration device coupled to a Finnigan/MAT 251 mass spectrometer at Oregon State University. Precision for water $\delta^{18}O$ analyses in fully automated mode is ±0.03 ‰ (1 standard deviation of local standards). Most of the seawater $\delta^{18}O$ analyses were replicated 2-4 times, bringing the average standard error to 0.02 ‰. Standardization of isotopic measurements was based on analyses of V-SMOW, GISP, and SLAP water standards provided by the U.S. National Institute of Standards and Technology (NIST), supplemented by daily analyses of local freshwater and saltwater standards.

Results

All seawater $\delta^{18}O$ and S data presented here have been submitted to the NASA/GISS Global Seawater Oxygen Isotope Database (http://www.giss.nasa.gov/data/o18data/) (Schmidt et al., 1999) and are also available in Appendix 1. Rainwater $\delta^{18}O$ data are available in Appendix 2.

Rainwater $\delta^{18}O$

The δ_P measurements from the central Panama Bight (ODP Leg 202) have a range similar to those collected on the westernmost edge of the Panama Bight (EPIC) in the eastern tropical Pacific along 95°W (Fig. 2.2). Most of the land-based samples from the Caribbean coast of Costa Rica had a higher δ_P than those collected from San Jose.

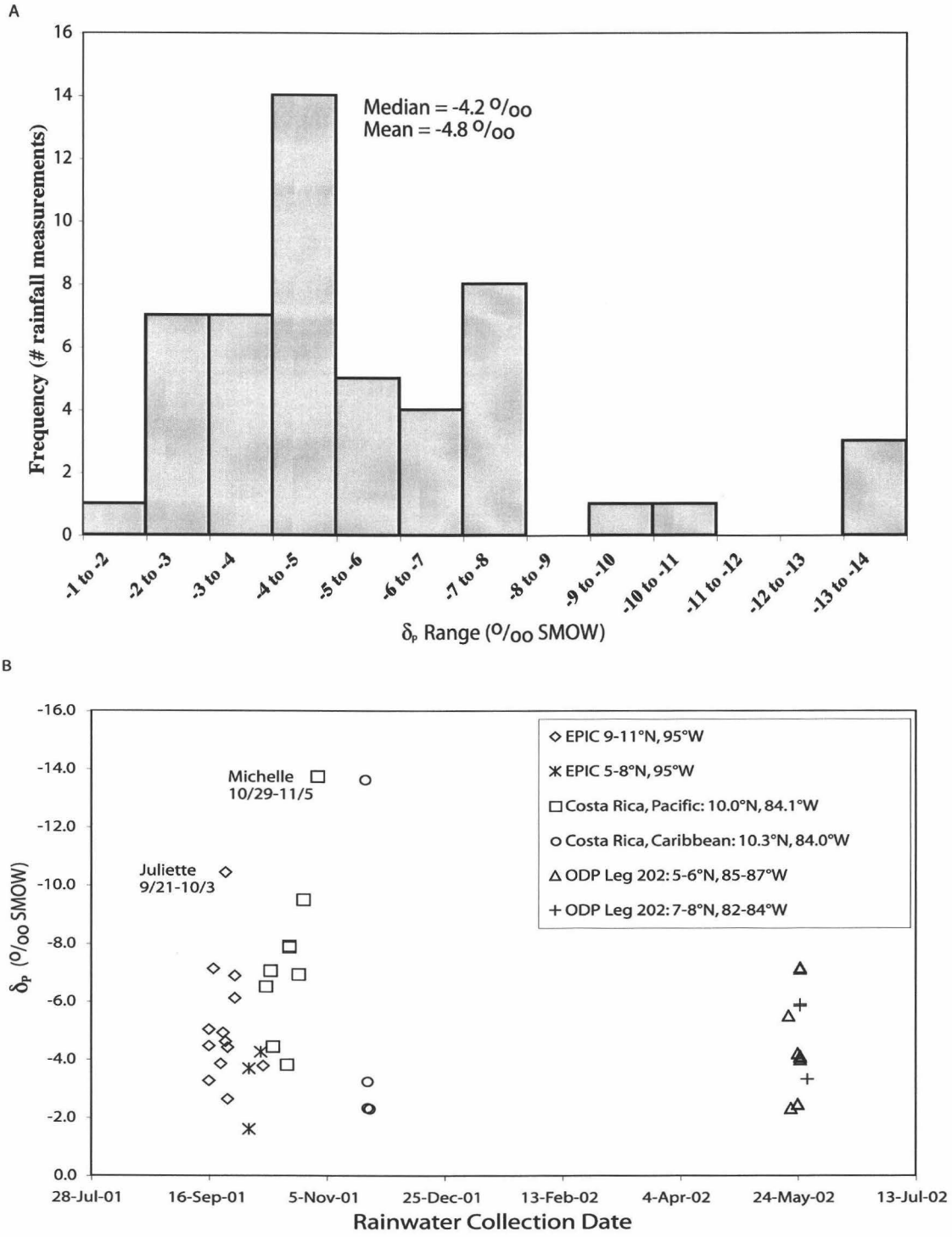

Figure 2.2. a. Histogram of δ_P reveals a distribution of typical precipitation events with median δ_P of -4.2 ‰, and rare storm events with δ_P of -10 to -14 ‰. **b.** Time series of δ_P from oceanographic surveys (EPIC, ODP Leg 202) and land-based measurements in Costa Rica. See Appendix 2 for δ_P data.

Excluding a few major storm events, the δ_P for typical rainfall events in the Panama Bight and Costa Rica (Fig. 2.2) averaged –4.8 ± 1.8 ‰ (1 standard deviation, range –1.6 to –9.5 ‰). The mean δ_P value is lower than average values previously reported for global-average open-ocean tropical sites (-2 ‰; a relatively crude estimate based on an assumed global average $\delta^{18}O$ of -4 ‰ for evaporated water (Craig and Gordon, 1965)).

Samples of precipitation from major storm events were significantly more depleted in ^{18}O (δ_P of -10 to -14 ‰) than typical local precipitation events (Fig. 2.2). A Category-4 hurricane (NOAA National Hurricane Center: http://www.nhc.noaa.gov) that originated in the Pacific (Juliette, sampled at 95°W, during the EPIC survey on 23 September 2001) yielded δ_P of -10.4 ‰. Another Category-4 hurricane, which originated in the Caribbean (Michelle, sampled in San Jose on 1 November, 2001) had δ_P of -13.7 ‰. Finally, just prior to the onset of Hurricane Olga, we sampled a tropical storm of Caribbean origin at Sarapiqui on 21 November 2001 that yielded δ_P of -13.7 ‰ and later crossed into the Pacific.

Seawater Data

Our new data from the Panama Bight yield a main trend in the δ_{SW}-S relationship within regional surface waters similar to that of the upper 50 m of the water column within a single depth transect (Fairbanks et al., 1982), but add detail and reveal multiple secondary trends (Fig. 2.3). Based on these limited measurements, the average $\delta^{18}O$ of surface seawater in the Panama Bight is –0.3 ± 0.2 ‰ (S of 32.2 ± 0.5 PSU) and that of subsurface water at 50-100 m depth is 0.35 ± 0.1 ‰ (S of 35.0 ± 0.1 PSU). This subsurface watermass, which upwells along the coast of Central and South America, is sometimes referred to as "13°C Water", which is thought to originate in the subpolar southern ocean, and is transported to the eastern tropical Pacific via the Equatorial Undercurrent, and modified along the way (Toggweiler et al., 1991; Tsuchiya and Talley, 1998). Based on Fig. 2.3, this upwelling water can be described as a mixture of ~60% South Pacific Tropical Waters (SPTW), a relatively high salinity

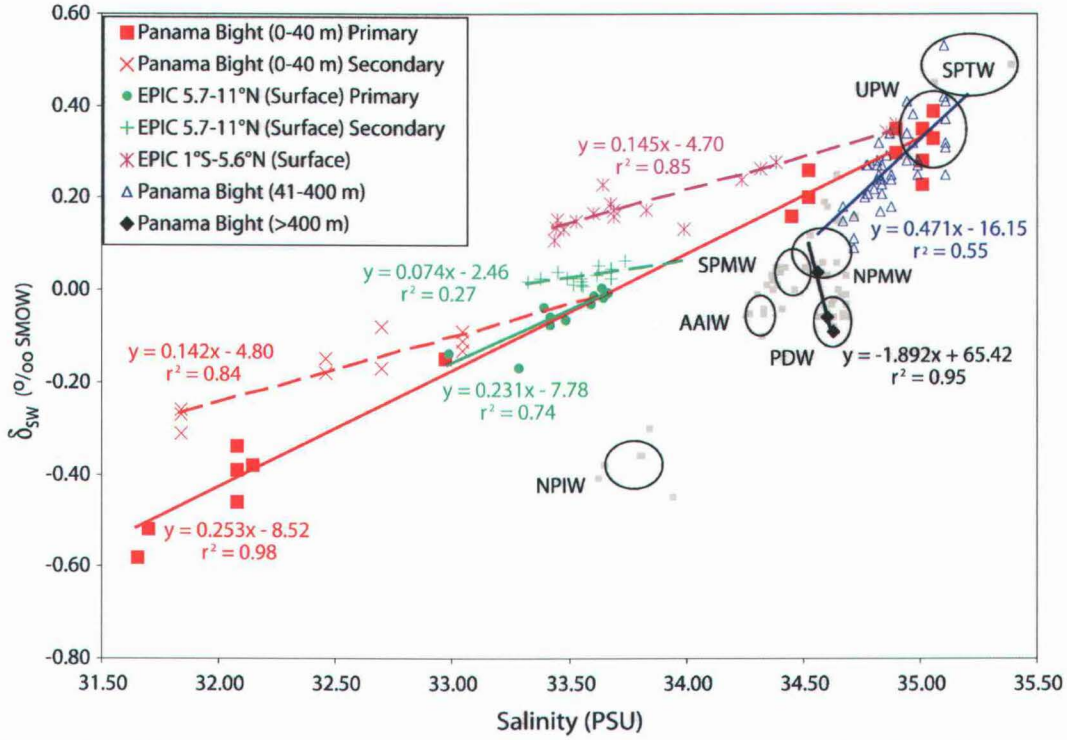

Figure 2.3. Measured δ_{SW}-S relationship in the eastern equatorial Pacific. The main trend of points within the Panama Bight, and in the eastern Pacific near the ITCZ (EPIC 5.7-11°N) has an apparent freshwater endmember of -7.8 to -8.5 ‰. Two distributions that splay off the main trend, in the EPIC survey near the equator (EPIC 1°S-5.6°N) and within the Panama Bight, project freshwater endmembers of -4.7 to -4.8 ‰, consistent with the measured average δ_P in the region (Fig. 2.2). Subsurface waters (41-400 m) define a relatively steep trend with an apparent freshwater endmember of -16.2 ‰, which is related to mixing with northern (NPMW) and southern (SPMW) subtropical mode waters. The intersection of subsurface and surface water points, with $\delta^{18}O$ of 0.3 ‰ and S of 34.9 PSU, documents mixing with water that upwells in the eastern equatorial Pacific and in the Costa Rica Dome. This upwelling component (UPW) is characteristic of "13°C Water" (Toggweiler et al., 1991; Tsuchiya and Talley, 1998), and can be described as a mixture of ~60% South Pacific Tropical Waters (SPTW) and ~20% subtropical mode waters of either South Pacific (SPMW) or North Pacific (NPMW) origin. Deep waters (>400 m) define a trend that is related to mixing between subtropical mode waters and Pacific Deep Water (PDW). Published data points (Schmidt et al., 1999) in light gray are used in combination with water mass definitions based on temperature, salinity, and depth (Toggweiler et al., 1991; Tsuchiya and Talley, 1998) to characterize the following regional water masses in δ_{SW}-S space: South Pacific Tropical Water (SPTW), South Pacific Mode Water (SPMW), North Pacific Mode Water (NPMW), Pacific Deep Water (PDW), Antarctic Intermediate Water (AAIW), and North Pacific Intermediate Water (NPIW). Ellipses represent average δ_{SW} and S ± one standard deviation.

water mass that forms in low-latitude regions of net evaporation, and ~40% subtropical mode waters of either South Pacific (SPMW) or North Pacific (NPMW) origin.

The primary δ_{SW}-S trend for the Panama Bight surface waters (Fig. 2.3) yields an apparent freshwater component with $\delta^{18}O$ of –8.5 ± 0.3 ‰ (r^2=0.98). This pattern is also visible at 95° W under the intertropical convergence zone (ITCZ), where the primary trend in the EPIC data (5.7-11°N) yields an apparent freshwater component with δ_{SW} of -7.8 ± 1.5 ‰ (r^2=0.74), which is statistically indistinguishable from the Panama Bight trend. Three secondary trends splay off the main trend with a lower slope, pointing toward similar freshwater end members with $\delta^{18}O$ of -2.5 ± 1.2 ‰ (r^2=0.27, EPIC data from 5.7-11°N), -4.7 ± 0.5 ‰ (r^2=0.85, EPIC data from near the equator (1°S-5.6°N), mixing directly with upwelling waters), and -4.8 ± 0.6 ‰ (r^2=0.84, selected NEMO data from the Panama Bight noted in Fig. 2.3). These secondary trends are consistent with the typical δ_P values we measured in the region (Fig. 2.2), suggesting that they reflect transient freshening of the sea surface following common small rainfall events of relatively local origin.

Discussion

Evaporation and Precipitation in the Panama Bight

High net precipitation (P-E > 0) maintains low surface salinities (Fig. 2.1a, b) and a strong, shallow pycnocline in the Panama Bight. In contrast, the Caribbean has high salinity due to high net evaporation (P-E < 0). Northeasterly trade winds carry water vapor across the Panama Isthmus and to the eastern Pacific warm pool of the Panama Bight. The high sea-surface temperature (SST) here helps to sustain atmospheric convection, resulting in heavy rainfall on the Pacific side of the Isthmus (Magaña et al., 1999).

Two distinct seasonal maxima in precipitation track seasonal SSTs in this region. SSTs rise in mid- to late May, as the ITCZ migrates northward from its boreal winter position at ~2° N, toward its boreal summer position at 8-10° N (Rodríguez-Rubio et

al., 2003). Atmospheric convection is initiated by the high SSTs, and the first rainy season persists through the end of June. Cloud cover during this first rainy season reduces radiative heating at the surface, however, causing SSTs to fall, and convection to diminish, in July and August, a time period known as the midsummer drought (Magaña et al., 1999). By August, the northeasterly trade winds strengthen, solar warming gradually heats the sea surface, and another phase of convective activity yields a second rainy season in September/October. Independent estimates of precipitation for this region from the NCEP/NCAR Reanalysis and the GOES Precipitation Index (Joyce and Arkin, 1997) confirm that ~80% of the annual rainfall in the Panama Bight region occurs between the months of May and December. Our limited sampling of rainfall includes the majority of this time period, excluding the midsummer drought months of July and August. Despite being termed a drought period, ~20-25% of the region's annual rainfall occurs during these months. Although we were unable to obtain rainwater samples during these months, the subset of seawater samples collected in August (Fairbanks et al., 1982) are consistent with the primary δ_{SW}-S trend (Fig. 2.3), suggesting that the isotopic signature of rainfall during these months falls within the range of our δ_P measurements.

The low salinity region of the Panama Bight (Fig. 2.1b) corresponds generally to the region of high net precipitation near the Panama Isthmus, and extends westward under the ITCZ at 8-10° N. However, on an annual average, two separate regions of highest net precipitation are found (near Costa Rica at roughly 5-9° N, 82-87° W, and near Colombia at roughly 4-7° N, 75-79° W). In contrast to these distinct net fresh water sources, a single region of low salinity appears in the eastern Panama Bight, and a low salinity tongue extends westward in the surface ocean in the latitude band 3-7° N, well south of the mean position of the ITCZ (although uncertainties in the salinity distribution reflect limited data (Bingham et al., 2002)). Misfits between the maps of P-E and sea-surface salinity indicate that advection and mixing of ocean waters are important processes that must be considered in the salinity balance.

4.2 Salinity Balance - Advection and Mixing

The largest advective components for the Panama Bight include the eastward flowing North Equatorial Countercurrent (NECC, roughly from 4-7° N) and the westward flowing South Equatorial Current (SEC, south of 4° N), each with mean geostrophic flows of ~15 Sv in the central Pacific (Wyrtki, 1966), but substantially weaker flows east of 110° W (Kessler, 2002). The westward flowing North Equatorial Current (NEC) is found north of 7° N. Upwelling through the base of the thermocline in the cyclonic Costa Rica Dome (with a center near 7° N, 90-95° W) represents a vertical flux of ~3.5 Sv (Kessler, 2002) although not all of this water reaches the sea surface. Substantial seasonal variability in currents and mixing occurs in the Panama Bight, with anticyclonic circulation in boreal winter and cyclonic circulation in boreal summer (Rodríguez-Rubio et al., 2003).

Not all of these fluxes modify the salinities of surface waters significantly in the Panama Bight. To estimate the effective rate of mixing on the sea-surface salinity and isotope budgets of the region, we calculate a salinity mass balance,

$$S_{PB} = [(F_{MIX})(S_{MIX})]/(F_P - F_E + F_{MIX} + F_{RIVER}) \qquad \textbf{(2.1)}$$

in which S_{PB} is the surface salinity of Panama Bight, F_{MIX} is the effective mixing flux, S_{MIX} is the average salinity of upwelled and advected water, F_P is the total precipitation over the Panama Bight, F_{RIVER} is the total runoff from regional rivers, and F_E is the total evaporation from the Panama Bight.

The mean annual salinity of Panama Bight surface waters is 32.7 PSU, which is based on the average of 12 analyzed monthly mean fields from 1°x1° grid boxes (Boyer et al., 1998) over the same area as the precipitation and evaporation fluxes (1-10° N, 75-90° W, excluding grid points on land or in the Caribbean Sea). The mean salinity of upwelled water is 34.9 PSU, and for advected water is 34.5 PSU (Boyer et al., 1998), but to test the sensitivity to a range of water masses we use values for S_{MIX} ranging from 34 to 35 PSU. We calculated an average F_P of 0.20 Sv and F_E of 0.09 Sv

over the Panama Bight region from the NCEP/NCAR Reanalysis. Freshwater fluxes for rivers can be ignored in this calculation, as they are two to three orders of magnitude smaller than marine precipitation in this region (SAGE River Discharge Database; http://www.sage.wisc.edu/riverdata).

Solving for F_{MIX}, we calculate a range of ~1.3-1.9 Sv for the effective mixing of upwelled and advected waters into surface waters of the Panama Bight, in the context of our box model. Next we use F_{MIX} to calculate the isotope mass balance in upper-ocean waters.

4.3 Isotope Balance and Precipitation

Using a simple box model extended from equation 2.1, we diagnose changes in δ_{SW} and S of the Panama Bight in response to varying precipitation (δ_P and F_P) using the following equation for calculating the isotope balance:

$$\delta_{SW} = ((F_P)(\delta_P) - (F_E)(\delta_E) + (F_{MIX})(\delta_{MIX}) + (F_{RIVER})(\delta_{RIVER}))/(F_P + F_{MIX} + F_{RIVER} - F_E) \quad \textbf{(2.2)}$$

in which for the modeled region, δ_{SW} is the mean $\delta^{18}O$ value of surface waters, δ_P is the mean $\delta^{18}O$ value of precipitation, δ_E is the mean $\delta^{18}O$ value of water evaporated, δ_{MIX} is the mean $\delta^{18}O$ value of ocean water that mixes with surface waters (for the modern ocean, 0.3 ‰, which corresponds to upwelling waters of salinity 34.9 PSU and a F_{MIX} of 1.3 Sv calculated from equation 2.1), and δ_{RIVER} is the mean $\delta^{18}O$ value of regional rivers. Other terms are as in equation 2.1.

The largest river inputs are from Colombia and Ecuador. For the modern annual average, F_{RIVER} is ~0.002 Sv (http://www.sage.wisc.edu/riverdata). We estimate the maximum possible isotopic contribution from these rivers by assigning a value for δ_{RIVER} that is based on the range of lowest regional δ_P measurements (-10 to -20 ‰) from high altitude sites in northern South America (IAEA/WMO (2001) Global Network of Isotopes in Precipitation, GNIP Database: http://isohis.iaea.org)).

The value of δ_E-δ_{SW} is uncertain. The equilibrium isotopic difference between vapor and liquid water at ~25°C is about -9 ‰, but actual fractionation factors are governed by kinetic effects of evaporation followed by slow molecular exchanges between the water and vapor phases (Craig et al., 1963). Relative humidity is an important factor, while wind speed effects seem to be negligible (Merlivat and Jouzel, 1979). To develop a plausible empirical estimate for δ_E, we use equation 2.2 with a range of δ_P values based on actual rainfall measurements (Fig. 2.2). The best fit to the main trend in the regional δ_{SW}-S distribution occurs when δ_P = -8.5 ‰ and δ_E-δ_{SW} is –8 ‰ (i.e., if Panama Bight surface water $\delta^{18}O$ is –0.3 ‰, then δ_E = -8.3 ‰) (Fig. 2.4). The response of the δ_{SW}-S relationship suggests that the isotopic endmember in the Panama Bight is largely determined by average δ_P. The overall effect of atmospheric freshwater fluxes (F_P, F_E) on surface salinity and δ_{SW} in the Panama Bight is an order of magnitude greater than the effect of F_{MIX}.

Freshwater Sources and Isotopic Endmembers

Some surface ocean samples from the Panama Bight exhibit a secondary trend of δ_{SW}-S, which points to an apparent $\delta^{18}O$ value for the freshwater component of –4.8 ± 0.6 ‰ (Fig. 2.3). Such a value is consistent with the average δ_P of -4.8 ± 1.8 ‰ we measured in the region. The primary δ_{SW}-S trend for the Panama Bight, however, predicts a freshwater component with $\delta^{18}O$ of –8.5 ± 0.3 ‰ (Fig. 2.3), which is not consistent with the average of local δ_P measurements (Fig. 2.2). A relatively ^{18}O-depleted freshwater source is needed to explain this main trend.

Water vapor that is transported from the Caribbean across Central America is lower in $\delta^{18}O$ than locally recycled Pacific water vapor because of long distance transport and orographic distillation. Costa Rican surface water $\delta^{18}O$ decreases by 6 to 8 ‰ upon crossing the Central American Cordillera, and values remain low along the Pacific coast relative to the Caribbean coast (Lachniet and Patterson, 2002). Our precipitation data also reveal significantly lower δ_P associated with relatively rare but

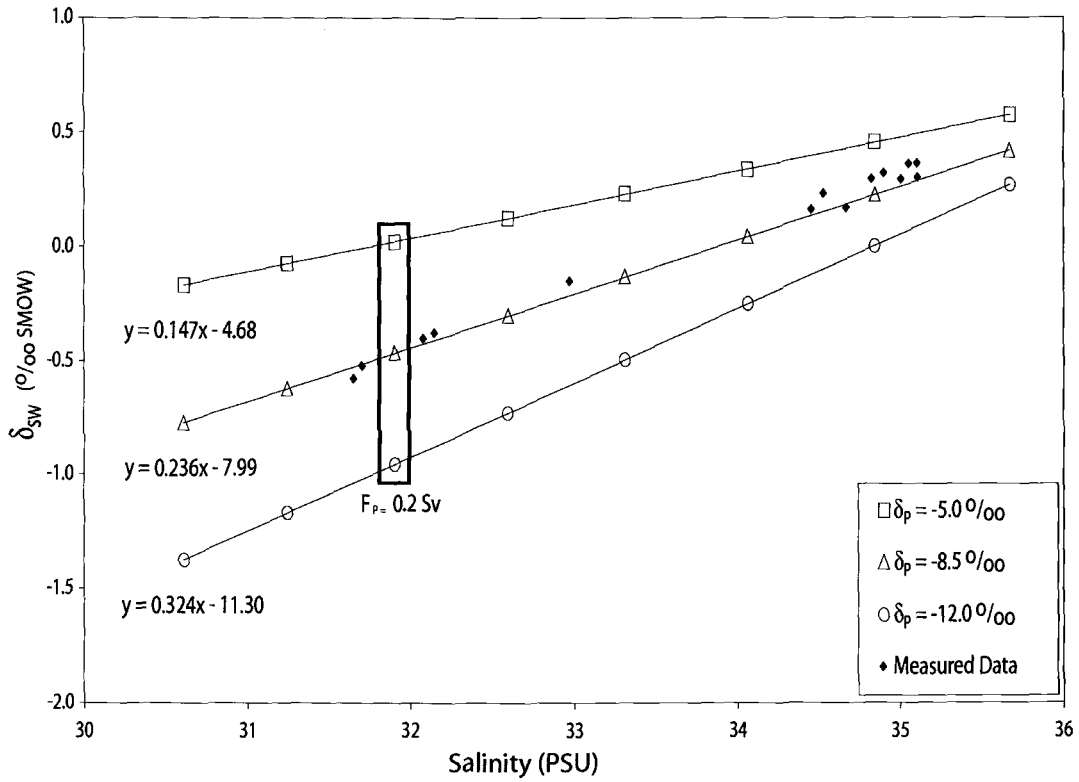

Figure 2.4. A comparison of seawater data from the Panama Bight and isotope mass balance calculations from a simple box model. A range of δ_P values are shown based on actual δ_P measurements from the region. Average surface δ_{SW} and S values based on a modern F_P of 0.2 Sv are indicated by the box.

intense rainfall events associated with tropical storms, some of which cross the isthmus from the Caribbean to the Pacific, and have δ_P values consistent with the primary δ_{SW}-S trend. A possible explanation for the apparent discrepancy between measured average δ_P in the Panama Bight and the $\delta^{18}O$ of the freshwater component predicted by the primary δ_{SW}-S trend is that a significant portion of the freshwater budget is comprised of these cross-isthmus and tropical storm sources, which were only sampled a few times in our limited data set.

Zonal winds have a net easterly component across the Panama Isthmus, which make the Caribbean a likely source for westward water vapor transport and excess Panama Bight precipitation (Peixoto and Oort, 1992; Zaucker and Broecker, 1992). Meridional transport of water vapor also occurs along the eastern Pacific boundary both from the south and the north (Peixoto and Oort, 1992). Variations in the δ_{SW}-S distribution in the Panama Bight may reflect changes in the relative contributions of Caribbean and Pacific water sources to this region.

Satellite wind and altimetry observations in the Panama Bight document seasonal variations in winds, which are associated with the meridional migration of the ITCZ (Rodríguez-Rubio et al., 2003). During boreal summer, the ITCZ is in its northernmost position, and the southeasterly trades become southwesterly upon crossing the Equator. A brief intensification of the northeasterly trades occurs during the midsummer drought in July and August (Magaña et al., 1999). In October, the ITCZ begins to migrate southward, and by boreal winter, the center of convective activity has shifted toward northern South America.

In addition to the seasonal migration of the ITCZ, smaller-scale wind jets and convective systems may affect the freshwater budget of the Panama Bight. Throughout the year, the westerly Chocó Jet brings atmospheric moisture from a Pacific source to coastal Colombia (Poveda and Mesa, 2000; Martínez et al., 2003), where annual rainfall totals are the highest for this region. The diurnal cycle of rainfall for coastal Colombia involves the development and offshore migration of convective systems that are related in size to local geographic features (Mapes et al., 2003). The

northerly Panama Jet (Chelton et al., 2000), which is strongest during northern hemisphere winter, travels from the Caribbean into the Pacific through topographic gaps in the Panama Isthmus.

Monthly average (1991-1998) δ_P measurements from Costa Rica along the western side of the Central American Cordillera (IAEA/WMO (2001) Global Network of Isotopes in Precipitation. The GNIP Database: http://isohis.iaea.org) reveal an isotopic seasonal cycle that tracks the cycle of precipitation amount. Relatively low δ_P values of -5 to –11 ‰ correspond with periods of maximum rainfall in May/June and September/October, when vapor transport from Caribbean sources is relatively strong (Lachniet and Patterson, 2002). These seasonal δ_P variations are consistent with the so-called "amount effect", which is commonly observed in tropical precipitation (Dansgaard, 1964).

Water Budget

A water and isotope budget for the Panama Bight can be constructed using a weighted sum of freshwater sources based on our new rainfall and seawater measurements. Our measured average δ_P for the Panama Bight is approximately –5 ‰, but cross-isthmus transport and tropical storms deliver freshwater with a much lower δ_P (average δ_P of -12 ‰ based on our measurements of large storm events). We can approximate the relative contributions of these freshwater sources to the Panama Bight in a simple isotope balance,

$$\delta_{P\ INTERCEPT} = (f_{PACIFIC})(\delta_{P\ PACIFIC}) + (f_{CARIB/STORM})(\delta_{P\ CARIB/STORM}) \qquad \textbf{(2.3)}$$

in which $\delta_{P\ INTERCEPT}$ is the average freshwater component predicted by the primary δ_{SW}-S trend (-8.5 ‰), $f_{PACIFIC}$ is the fraction of freshwater contributed by local Pacific sources, $\delta_{P\ PACIFIC}$ is the average δ_P of local Pacific rainfall (-5 ‰), $f_{CARIB/STORM}$ is the fraction of freshwater contributed by Caribbean and/or tropical storm sources (1-

$f_{PACIFIC}$), and $\delta_{P\ CARIB/STORM}$ is the average δ_P of Caribbean and/or tropical storm rainfall (-12 ‰).

This simple calculation suggests that about half of the rainfall in the Panama Bight region may be of Caribbean and/or tropical storm origin. Based on the integrated net precipitation in this region of 0.2 Sv (NCEP/NCAR Reanalysis), this weighting suggests that ~0.1 Sv of Panama Bight rainfall has a lower $\delta^{18}O$ indicative of long distance transport. This estimate is at the low end of AGCM and climatologic estimates of net cross-isthmus vapor transport of 0.13 Sv (Zaucker and Broecker, 1992) to 0.45 Sv (Baumgartner and Reichel, 1975; Manabe and Stouffer, 1988; Hostetler and Mix, 1999), but is fully consistent with these estimates if some of the isthmus-crossing vapor rains out at sites beyond the region we examined.

Paleoceanographic Implications

Our analysis of water sources and the controls on the regional δ_{SW}-S relationship is important to paleoceanographers who seek to reconstruct paleosalinity based on measurements of $\delta^{18}O$ and paleotemperature in fossil shells. A common assumption underlying paleosalinity reconstructions is that the modern δ_{SW}-S relationship applies through time. Here we employ model equations 2.1 and 2.2 to assess the sensitivity of the Panama Bight δ_{SW}-S relationship to plausible changes in individual flux (F_P, F_{MIX}, F_E) and isotopic (δ_P, δ_E) parameters and estimate the corresponding paleosalinity error. Here, a paleosalinity error refers to the discrepancy in salinity that occurs when the modern δ_{SW}-S relationship is assumed rather than applying the δ_{SW}-S that corresponds with potential flux and/or isotopic changes. We then modify multiple parameters simultaneously to test the sensitivity of the Panama Bight surface ocean to potential climate-driven changes in the water budget.

The calculations from equations 2.1 and 2.2 suggest that the modern δ_{SW}-S relationship in the Panama Bight is primarily controlled by variations in F_P and δ_P. Sensitivity tests (not shown here) indicate that a two-fold change in any of the flux parameters, with no change in the isotopic composition of precipitation, yields only a

minor change in the δ_{SW}-S relationship, producing a typical paleosalinity error of <0.1 PSU. However, changes in the isotopic composition of evaporation or precipitation moves the mixing line up or down which would induce substantial errors in paleosalinity estimates if the incorrect modern δ_{SW}-S relationship was applied. For example, an undetected two-fold change in δ_E-δ_{SW} would produce a paleosalinity error of ~1-2 PSU. Likewise, a 3.5 ‰ change in average δ_P (Fig. 2.4), which is within the range of our modern measurements, would result in a paleosalinity error of ~2 PSU. We expect that major changes in δ_E-δ_{SW} are unlikely, because such evaporation effects are relatively insensitive to wind speed, and water vapor near the sea surface approaches saturation. Long-term variations in δ_P, plausibly linked to changes in the relative weighting of local versus long-distance sources of fresh water, are more likely to change the δ_{SW}-S relationship in the Panama Bight. The total range of paleosalinity errors we observe for all parameters (0.1 to 2 PSU) is comparable to previously published error margins (Rohling and Bigg, 1998).

In a series of sensitivity tests, we modify various parameters in the freshwater budget to predict how the Panama Bight δ_{SW}-S might evolve temporally in response to changing climate conditions. AGCM simulations of the LGM predict increased mid-troposphere wind speeds in the tropical Pacific, and thus water vapor transport across the Panama Isthmus increased by a factor of two to four relative to the modern simulation (Hostetler and Mix, 1999). According to our freshwater budget (equation 2.3), this climate scenario would significantly affect the average δ_P in the Panama Bight region. If we hypothetically attribute all changes in F_P to changes in cross-isthmus transport and hold the local Pacific freshwater component constant at its modern value of ~0.1 Sv, we can calculate δ_P as a function of F_P based on equation 2.3. In this experiment, we assume no change in the average δ_P of local Pacific (-5 ‰) and cross-isthmus (-12 ‰) freshwater sources. If all other variables (F_E, δ_E-δ_{SW}, F_{RIVER}, δ_{RIVER}, F_{MIX}, S_{MIX}, δ_{MIX}) remain constant, the temporal change in surface ocean δ_{SW}-S relationship varies along a steeper apparent trendline than the modern

data (Fig. 2.5). In response to stronger LGM winds and cooler tropical SSTs (Hostetler and Mix, 1999), we also apply hypothetical two-fold changes in mixing (2 x F_{MIX}) and evaporative fluxes (0.5 x F_E), both of which increase the slope slightly and shift the surface ocean trendline towards higher δ_{SW} and S values (Fig. 2.5), although this effect is small relative to changes in δ_P. We also test wind speed-induced changes in the kinetic fractionation factor (Merlivat and Jouzel, 1979) by modifying δ_E-δ_{SW}, but the resulting isotopic shift in the δ_{SW}-S relationship is insignificant, so it is not shown here. This finding is consistent with previous modeling work (Schmidt, 1999), which shows that constant vs. wind speed-dependent formulations of the kinetic fractionation factor ultimately result in only a 0.01 ‰ discrepancy in δ_{SW}.

Using a similar approach, we explore an alternate scenario in which we maintain a constant cross-isthmus component (~0.1 Sv) and attribute all changes in F_P to changes in the local Pacific freshwater component. Such a scenario may be manifested in changes in mean ITCZ position and/or intensity. The resulting surface ocean δ_{SW}-S relationship (Fig. 2.5) is very similar to that of the Panama Bight off-trend data (Fig. 2.3), which shows a significantly higher $\delta^{18}O$ value for the freshwater endmember than the primary δ_{SW}-S trend.

Our model sensitivity experiments with hypothetical changes in water sources and isotope budgets indicate that the largest errors in isotopic paleosalinity estimates occur when isotopic compositions of precipitation are changed. Experiments involving plausible climate-driven variations in the freshwater budget provide insight into how the Panama Bight surface ocean δ_{SW}-S relationship may evolve temporally. These model sensitivity tests apply to the main regional trend of the δ_{SW}-S relationship, which is based on modern upper ocean measurements. However, in any climate scenario the kind of transient variability associated with the secondary trends we have observed that splay off the main trend (Fig. 2.3) may also apply. It is uncertain how important the secondary trends in the δ_{SW}-S relationship are for paleosalinity estimates. If these features are relatively rare or transient, then it is likely that the $\delta^{18}O_{carbonate}$ of mixed layer-dwelling planktonic foraminifera would reflect conditions

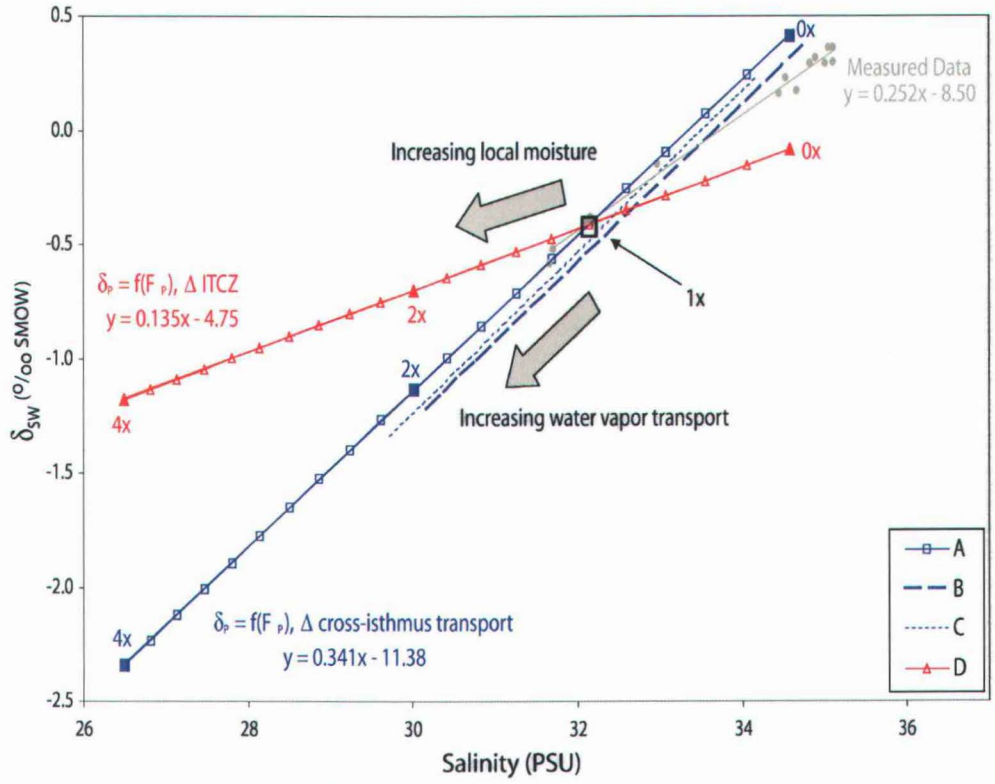

Figure 2.5. Panama Bight surface ocean δ_{SW}-S response to potential climate-induced changes in the water budget. **A:** A hypothetical LGM simulation in which the local Pacific freshwater component is held constant at its modern value (~0.1 Sv) while variations in cross-isthmus water vapor flux control the total F_P. δ_P is calculated as a function of F_P based on a flux-weighted freshwater budget (equation 2.3), and all other parameters, including the average δ_P of the two primary atmospheric moisture sources, are unchanged from modern values; **B:** In addition to precipitation variations described in **A**, we apply a two-fold increase in F_{MIX} in response to increased wind speeds; **C:** In addition to the conditions outlined in **B**, we apply a 2-fold decrease in F_E in response to lower LGM temperatures; **D:** A hypothetical climate simulation in which the cross-isthmus component is held constant at its modern value (~0.1 Sv) while variations in the local Pacific freshwater flux control the total F_P. Again, δ_P is calculated as a function of F_P based on equation 2.3, and all other parameters are unchanged from modern values. The δ_{SW}-S values corresponding to 0x-4x changes in the cross-isthmus and local Pacific freshwater fluxes (relative to modern) are highlighted. The box encompasses modern δ_{SW}-S (1x) conditions, which represents a 50:50 combination of the two sources.

represented by the main δ_{SW}-S trend. We consider this the most likely scenario. Alternatively, if the secondary trends are stable features, then isotopic paleosalinity estimates based on a correct main trend in δ_{SW}-S would still only provide reasonable upper-limit estimates of paleosalinities.

Conclusions

The main trend of upper ocean $\delta^{18}O$ and S measurements indicates that the average $\delta^{18}O$ of freshwater delivered to the Panama Bight is about –8.5 ‰, which is lower than the mean isotopic value of typical rainfall events in the region. Some of the surface ocean data splay off the primary δ_{SW}-S trend, and reveal a secondary freshwater component with $\delta^{18}O$ of about –4.8 ‰, which is consistent with the average of our δ_P measurements from this region.

Specific humidity and modern seasonal wind field data reveal variations in wind patterns and the position of the ITCZ that help to identify potential freshwater sources for Panama Bight rainfall. A strong low-level northeasterly component crosses the Panama Isthmus and introduces water vapor from Caribbean sources, in addition to southwesterly and meridional components that introduce water vapor from regional Pacific sources. The primary freshwater endmember ($\delta^{18}O$ of -8.5 ‰) likely represents a ~50:50 combination of relatively local precipitation sources (δ_P of –5 ‰) and more ^{18}O-depleted water vapor that combines sources from the Caribbean and from tropical storms originating on either side of the Isthmus (δ_P of -10 to -14 ‰).

Mass balance equations in a simple box model quantify the relative importance of precipitation, advection/upwelling, and rivers in the Panama Bight isotope and water budget, and help to predict plausible changes in δ_{SW}-S distributions under different climate regimes. Long-term changes in the upper ocean δ_{SW}-S distribution of the Panama Bight are relatively insensitive to changes in the rate of oceanic advection and upwelling. Significant changes in average δ_P, which may reflect changes in the relative contributions of distant (Caribbean and/or large storms) versus local (Pacific) freshwater sources, produce the largest changes in the δ_{SW}-S relationship and the

largest systematic errors in paleosalinity estimates based on analyses of fossil shells. This study of the modern water and isotope budgets will help to constrain the interpretation of the geologic record of paleosalinity based on $\delta^{18}O$ measurements in fossil carbonates.

3. ADAPTATION OF A FLOW-THROUGH LEACHING PROCEDURE FOR MG/CA PALEOTHERMOMETRY

Heather M. Benway, Brian A. Haley, Gary P. Klinkhammer, and Alan C. Mix

Geochemistry Geophysics Geosystems G^3
http://www.agu.org/journals/gc/
Volume 4, Number 2
8403, doi: 10.1029/2002GC000312

Abstract

Mg/Ca ratios in planktonic foraminifera reflect calcification temperatures and are thus useful for sea surface temperature (SST) reconstructions. Despite the obvious utility of this paleoceanographic tracer, problems of dissolution, gametogenic calcification, and contaminant phases have thus far limited confidence in Mg/Ca-based reconstructions. Here we show strong evidence of Mg heterogeneity in foraminiferal calcite by sequentially measuring the composition of different forms of calcite (ontogenetic, gametogenic, diagenetic) in the same shells, while monitoring and removing contaminant phases. A new flow-through method combines chromatographic technology and inductively coupled plasma mass spectrometry (ICP-MS) in a series of cleaning and dissolution reactions monitored continuously with time-resolved analysis (TRA). This combination of slow, controlled dissolution and TRA provides a complete elemental description of contaminant phases and sorts the cleaned calcium carbonate based on dissolution sensitivity.

Examination of partially dissolved shells with electron microscopy suggests that the flow-through method simulates the natural dissolution sequence and effectively separates the different calcite domains within a single foraminiferal shell. Heterogeneity of Mg/Ca in foraminiferal calcite is clearly demonstrated in flow-through analysis. Foraminiferal shells have initially high Mg levels that decrease steadily throughout dissolution. Later dissolution yields lower Mg/Ca, which is likely due to a combination of subsurface calcification and biomineralization effects. Mg/Ca ratios from the most dissolution-sensitive (high-Mg) portions of surface dwelling species in core tops are used to calculate calcification temperatures. A comparison of late Holocene core top data with World Ocean Atlas SST data indicates that the flow-through method does yield viable SST estimates. Furthermore, a depth transect in the eastern tropical Pacific suggests that this approach provides the opportunity to extract initial calcification temperatures despite partial dissolution of foraminiferal shells.

Introduction

Mg is a conservative element in the world's oceans with a residence time of ~13 million years (Broecker and Peng, 1982). Despite a nearly constant Mg/Ca ratio in seawater, Mg distribution in biogenic calcite is heterogeneous (Bender et al., 1975). This heterogeneity may be attributed to the differences in the Mg partition coefficients between inorganically and biogenically precipitated calcite (Katz, 1973; Mucci and Morse, 1990), as well as the large range of temperatures over which calcification occurs (Nürnberg et al., 1996). A discrepancy between relatively high Mg/Ca predicted by thermodynamics and low Mg content measured in foraminifera suggests that Mg substitution is physiologically controlled.

Evidence from recent laboratory cultures (Nürnberg et al., 1996; Lea et al., 1999) and core top studies (Hastings et al., 1998; Lea et al., 2000; Nürnberg et al., 2000) of different species of foraminifera has identified temperature as a primary environmental controlling factor on Mg/Ca. Other parameters, such as light, nutrient levels, and growth rate may also affect Mg substitution in biogenic calcite (Delaney et al., 1985; Nürnberg et al., 1996; Lea et al., 1999), but appear to be less important than temperature. For example, salinity effects are relatively minor, and have only proven significant for large salinity changes on the order of 10 ‰, which are highly unrealistic for the open ocean over time scales of paleoceanographic interest (10^4-10^5 years).

Several studies have shown evidence of Mg heterogeneity in foraminiferal tests (Brown and Elderfield, 1996; Nürnberg et al., 1996; Jha and Elderfield, 2000), but there is still uncertainty about the mechanisms responsible for this heterogeneity. In addition to environmental variables (ie., temperature), physiologically controlled biomineralization processes may regulate Mg distribution in foraminiferal calcite (Elderfield et al., 1996). In a culture experiment, Nürnberg et al. (1996) showed significant differences in the Mg content between ontogenetic and gametogenic calcite. In the case of a culture experiment, which maintains a constant temperature, these differences cannot be attributed to calcification at depth (ie., lower

temperatures). Regardless of the controlling mechanism (physiological vs. environmental), Mg/Ca in secondary crust may not accurately reflect the initial calcification temperature that is sought after in paleoceanographic studies. Since gametogenesis can contribute a considerable proportion of the total foraminiferal weight (Bé, 1980, Erez and Honjo, 1981), it is likely that calculations of calcification temperature based on the Mg/Ca of the whole test are biased by the Mg/Ca of the secondary crust toward subsurface temperatures or by physiological conditions that do not represent primary calcification in near surface waters. In the case of the Nürnberg et al. (1996) culture experiment, in which secondary crust showed higher Mg/Ca, this would bias towards a higher calcification temperature. Given our limited understanding of the physiological controls on foraminiferal calcite, we also recognize that the Mg/Ca of primary calcite may not be exclusively related to calcification temperature. Nevertheless, known heterogeneity may be a fatal flaw in the Mg/Ca paleotemperature method, which must be addressed before Mg/Ca can become a fully reliable paleoceanographic tool.

A major problem with applying Mg/Ca paleothermometry to geologic samples is dissolution (Lohmann, 1995; McCorkle et al., 1995), both in the water column and in the sediment. Experimentation with artificial seawater indicates that the solubility of pure calcite is influenced by the degree of supersaturation, surface area exposure, and Mg content (Rushdi et al., 1998). Since high-Mg calcite is more soluble than low-Mg calcite (Brown and Elderfield, 1996; Rushdi et al., 1998; Davis et al., 2000), partial dissolution of foraminiferal shells on the seafloor selectively preserves calcite with lower Mg/Ca, biased to reflect colder calcification temperatures. Core top Mg/Ca measurements in planktonic foraminifera confirm this effect; Mg/Ca is correlated with water depth (Rosenthal and Boyle, 1993; Russell et al., 1994). Lea et al. (2000) calculated a decrease in Mg/Ca of 12% for each kilometer of water depth for cores in the equatorial Pacific, which translates to a temperature bias of $-1.3°C$ per kilometer for modern conditions.

In the following experiments, we focus on eastern tropical Pacific core top specimens of *Globigerinoides ruber* and *Globigerinoides sacculifer*, which are commonly used in ocean temperature reconstructions because of their near surface habitats. Core top Mg/Ca and $\delta^{18}O$ measurements of *G. ruber* and *G. sacculifer* from Ontong Java Plateau, Ceara Rise, and Sierra Leone Rise depth transects have shown significant dissolution effects (Rosenthal et al., 2000; Dekens et al., 2002). Others have addressed the dissolution problem in different ways, by applying statistical correction terms to calibration equations based on water depth (Dekens et al., 2002), or by developing dissolution proxies (Bassinot et al., 2001). Here we address issues of dissolution and shell heterogeneity more directly with an innovative chemical technique that cleans and sequentially dissolves biogenic calcite and thus allows Mg/Ca heterogeneity within shells to be analyzed and better understood.

Methods

In previous studies of Mg/Ca in foraminifera, a batch dissolution method has been used. In this method, cleaning is done "offline," and dissolution occurs in a single step prior to analysis. This yields one Mg/Ca value per calcite sample, essentially representing a Ca-weighted average over the entire sample. This method cannot directly assess heterogeneity of Mg within shells. To address this problem, we have applied a new automated flow-through dissolution method (Haley and Klinkhammer, 2002) developed for rare earth element (REE) analysis. This method interfaces a customized Dionex Ion Chromatograph (IC) with a VG PQ ExCell quadrupole Inductively Coupled Plasma-Mass Spectrometer (ICP-MS) with Time Resolved Analysis (TRA). TRA generates multiple Mg/Ca measurements per sample, thus providing a high-resolution breakdown of cleaning and dissolution reactions from start to finish.

Flow-through cleaning passes a steady stream of reagents over the calcite sample. In this stream, the calcite is cleaned and then dissolved. The IC system is fitted with an Advanced Gradient Pump (AGP), which precisely regulates the flow (pressure) and

eluant concentration, and a Dionex LC25 Ion Chromatography heater to control the temperature of the reactions (here, 80°C). Internal standardization (Falkner et al., 1994) with ^{9}Be and ^{115}In (bracketing the mass range for Mg and Ca measurement) continuously corrects for quadrupole drift. These standards are introduced to the eluate as it flows from the IC into the ICP-MS. $^{25,26}Mg$ and $^{43,48}Ca$ are measured using ICP-MS, and Mg/Ca ratios are calculated from standard curves for each isotope. The method can also be run in a different mode using a fraction collector with the Dionex system. In this mode, the dissolution product is collected in a series of fraction collector tubes, and the standards are added to each tube manually prior to analysis on the ICP-MS. To obtain blank corrections, an empty sample column is run using the same flow-through cleaning and dissolution procedures outlined above. This yields a time-resolved blank correction that is applied to each corresponding time step of the sample data.

We pick approximately 20-30 foraminiferal shells from each sample and place them in 63-μm sieves, where they are cracked just enough to break open the chambers. To remove clays, the shells are sonicated in deionized water and ethanol. The samples are inspected under microscopy for cleanliness, and sonication is repeated if necessary. Clean shells are loaded by hand into disposable sample columns and cleaned and dissolved with the following sequence of reagents using the flow-through method. First, Hydroxylamine HCl (pH>9) is used to remove a coating phase, which contains Mn, Cd, and Mg. During method development, Mg was monitored via TRA during this cleaning step to insure that the contaminant phase had been completely removed (Haley and Klinkhammer, 2002). To remove build-up of elements that may adsorb to the tubing walls (in a high-pH environment), the system is then rinsed with strong acid (1 M HNO_3), bypassing the sample to avoid premature dissolution. Then the sample itself is rinsed with deionized water prior to dissolution. Finally, dilute acid (0.01 N HNO_3) is used to dissolve the sample at a controlled rate. Since the calcite of different foraminiferal species dissolves at different rates, as observed with dissolution in the ocean (Berger, 1970), it is sometimes necessary to adjust acid

strength (and thus, the dissolution time) accordingly. The acid strength can be adjusted easily via the programmable AGP, which can mix acid and deionized water prior to entering the sample column.

In replicate samples, dissolution proceeds from start to finish in approximately the same amount of time, regardless of sample size, providing evidence that the system is in steady state. The benefit of being in steady state is that cleaning and dissolution reactions are consistent and regulated to a high degree of accuracy, regardless of variability between samples. Standard error of Mg/Ca measurements using the flow-through method is ~2.5%. A more complete description of the analytical details of the method, including comparisons of batch (Lea et al., 1999) and flow-through Mg/Ca results, is available in Haley and Klinkhammer (2002).

Results and Discussion

Quenched Dissolution Experiment:

Does our flow-through system dissolve different parts of the foraminifera in a way that mimics the natural dissolution process? Foraminifera have complex shells. They tend to calcify in discrete layers, and although the shell is entirely composed of calcite, the layers may take different crystal forms that dissolve at different rates. For example, Bé and Lott (1964) illustrate two layers of calcite in living foraminifera from plankton tow samples – in each chamber two layers are deposited, a thin inner layer, and a thicker layer with prismatic crystals oriented perpendicularly to the test surface. The outer lamella envelops the exterior of earlier chambers, making these primary biogenic structures difficult to see in the early chambers. In specimens recovered from water depths of more than several hundred meters, these lamellae are typically covered by a third layer, a calcite "crust" formed of randomly oriented euhedral crystals. Bé et al. (1975) refer to these three discrete layers of calcite (in order of decreasing dissolution sensitivity) as the "microgranular layer", the "subrhombic layer", and the "euhedral layer," respectively (or alternatively, the first two layers are "ontogenetic calcite" and the third layer is "gametogenic calcite").

To test whether foraminifera dissolve sequentially in our apparatus as they do on the seafloor, we performed partial dissolution experiments, which were quenched at different stages of dissolution. The partially dissolved shells were then compared visually (using electron microscopy) to naturally dissolved shells from a depth transect of sediment cores. For our partial dissolution experiments, we selected well-preserved shells of *Globigerinoides sacculifer* from the top of multicore MW9720-MC1, recovered from 1775 m water depth on Ontong Java Plateau (1° 29.75' S, 157° 30.20' E). These shells were cleaned ultrasonically (without crushing, so we could see the reasonably complete shells after our experiments), and then subjected to sequential dissolution in our normal online reaction chamber. After partial dissolution, the reactions were quenched with dilute NH_4OH, and the shells were removed and prepared for observation with a CAMECA SX-50 electron microprobe. For comparison, we also observed shells that dissolved naturally on the sea floor, hand picked from the top of multicore MW9720-MC37, recovered from 3707 m water depth on Ontong Java Plateau (0° 00.36' S, 161° 23.28' E). This is the deepest available multicore on Ontong Java Plateau that contains identifiable (although often fragmented) shells of *G. sacculifer*. In cores from deeper sites, we observed only shell fragments, with no identifiable *G. sacculifer*.

Results from our partial dissolution experiments are illustrated in Fig. 3.1. In the top two panels (Fig. 3.1A, B), pristine shells taken from 1775 m water depth were cleaned ultrasonically (three times, five minutes each, in ethanol) but otherwise were unprocessed. These panels show all three layers of the test wall. The surface of the interior microgranular layer is smooth (Fig. 3.1A). The exterior of the test shows pitted areas and pores (Fig. 3.1B) that were associated with the bases of spines shed from the living cell. Note especially the complete interior layer and smooth periphery of the pores.

In Fig. 3.1C, cleaned shells were subjected to partial dissolution for one minute, removing about 5% of the total calcite (based on weight loss). Note here the enlargement of the pores, their ragged edges, and apparent thinning of the interior

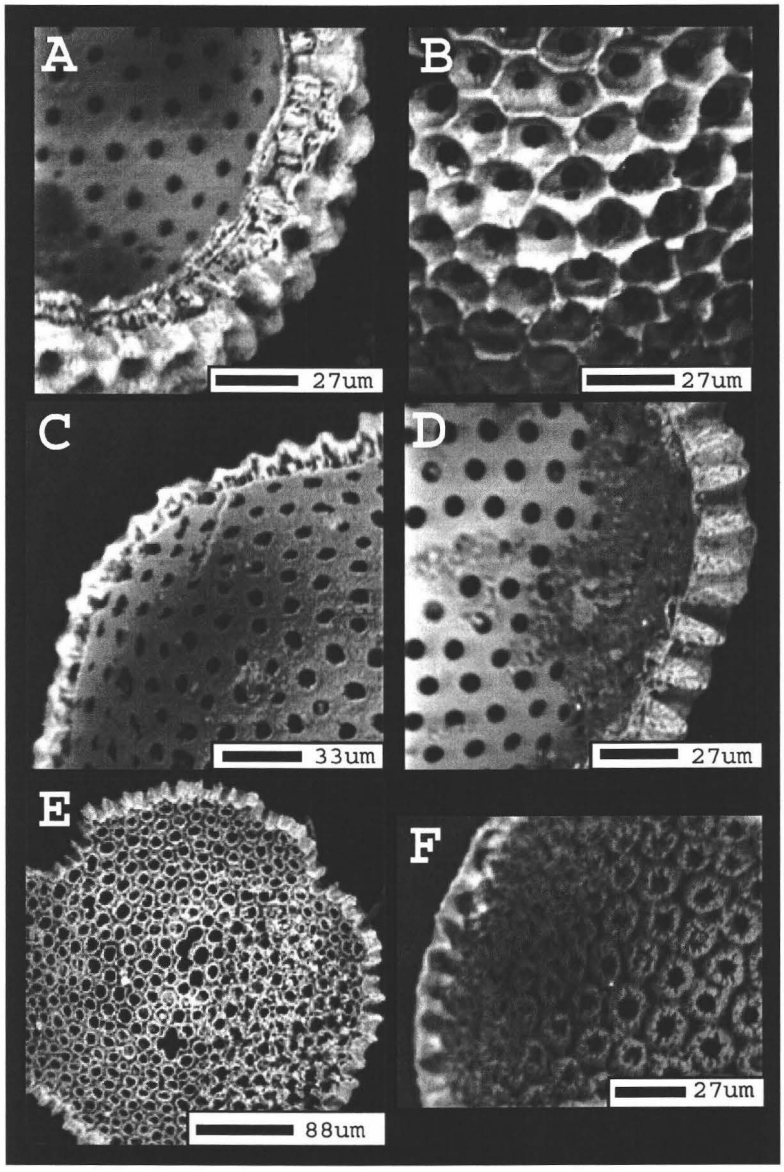

Figure 3.1: Backscatter scanning electron micrographs of *G. sacculifer* shells to illustrate continuous dissolution in our reaction chamber vs. nature: A) Interior; and B) Exterior of ultrasonically cleaned shells picked from 1775 m water depth on Ontong Java Plateau (MW9720-MC1: 1° 29.75' S, 157° 30.20' E, 1775 m) - note pristine appearance and interior layers; C) Experiment in which partial dissolution removed ~5% of the total calcite - note enlargement and corrosion of the interior layer around the pores; D) A relatively complete shell from 3707 m water depth on Ontong Java Plateau (MW9720-MC37: 0° 00.36' S, 161° 23.28' E, 3707 m) illustrating similar interior corrosion on sea floor; E) Experiment in which partial dissolution removed ~60% of the total calcite - note interior layer gone, pores in exterior layer now corroding; F) Shell fragments from 3707 m water depth illustrating similar removal of interior layer under severe dissolution.

layer. This represents early dissolution of the shell, from the inside out. Compare Fig. 3.1C to the seafloor specimen of Fig. 3.1D, a relatively complete shell picked from 3707 m water depth, which we cracked open to observe the interior – note similar thinning and apparent corrosion of the interior microgranular layer.

In a more severe dissolution experiment, shells similar to those of Fig. 3.1A were subjected to dissolution for 6 minutes, removing about 60% of the total calcite. In the shell fragments remaining from this dissolution (Fig. 3.1E) note that the interior microgranular layer is essentially gone, and that the exterior layer is now corroding as the pores expand to yield a "lacy" appearance. We observed a similar dissolution pattern in naturally dissolved seafloor shell fragments from 3707 m water depth (Fig. 3.1F). Similar to the specimen dissolved in the laboratory, the interior microgranular layer is essentially gone, and the pores are corroding. At greater degrees of dissolution, the shells fragment and become difficult to recognize or pick without falling apart.

The point of this experiment is that the dissolution sequences in our experimental chamber and on the sea floor are quite similar. The early dissolution tends to remove the interior microgranular layer first, and the exterior layers dissolve later. This is important, because it shows that our method does simulate the sequential dissolution process that occurs on the seafloor, chemically sorting genetically distinct layers of calcite. The earliest calcite dissolved appears to be the inner calcite layers, which are most likely to have formed in warmer, near-surface waters. The late-stage dissolution products are the outer layers and "crusts" that tend to form in deeper waters.

A similar order of dissolution was found by Bé et al. (1975) -- first the microgranular layer, followed by subrhombic layer, and finally the euhedral layer (although their illustrations show only exterior surfaces). Hecht et al. (1975) argued that foraminifera dissolve from the outside layers in, and from final chambers to the earlier chambers. Our observations of shell interiors at first glance appear to disagree with their suggested order of layers. Note, however, that Hecht et al. (1975) only examined the exterior of the shells and illustrated only cases in which 70% or more of

the calcite was dissolved from *G. sacculifer*. In this range, which we could call severe dissolution, our results are consistent. We agree that when the outer chambers dissolve, they tend to fragment from the terminal chambers first, but in our observations this only seems to occur *after* the inner microgranular layer is essentially gone.

Results from these quenching experiments suggest that sequential dissolution discriminates between genetically distinct calcite domains in the foraminiferal shells. We expect that the main reason the inner layers dissolve more quickly is that they have a higher Mg/Ca ratio. If sequential dissolution can sort calcite by its Mg content, we hypothesize that the earliest dissolution we observe is from microgranular layers formed in the warmest (near-surface) water.

Mg heterogeneity and estimates of calcification temperature:

To test for heterogeneity of the Mg/Ca ratio in foraminifera, we analyzed specimens of *G. ruber* (250-355 μm size fraction) and *G. sacculifer* (355-425 μm size fraction, no terminal sac-like chamber) from core tops in the eastern tropical Pacific. Deeper sites showed some fragmentation of the foraminifera, suggesting that partial dissolution had occurred. In all analyses, Mg/Ca in *G. ruber* and *G. sacculifer* declined as the dissolution progressed (Fig. 3.2), providing strong evidence of Mg heterogeneity in foraminiferal calcite. We show Sr/Ca data for the same samples for comparison. Sr/Ca ratios remain relatively constant throughout the dissolution with the exception of minor (~0.1-0.2 mmol/mol) step changes near the middle to the end of the run that are still not fully understood. Haley and Klinkhammer (2002) observed the same trends in Mg/Ca in earlier analyses of *G. sacculifer*. A small spike (~2-3 ppb) in Mg is observed near the beginning of the run in samples ME0005A-15MC *G. ruber* and Y69-106P *G. sacculifer* (Fig. 3.2). This Mg spike occurs during the deionized water flush of the sample column (prior to the introduction of the dilute acid), which removes any remaining traces of contaminant phases from sample cleaning. These small spikes are not accompanied by significant Ca or Sr increases, and thus do not

Figure 3.2: Sequential dissolution of specimens of *G. ruber* and *G. sacculifer* from three cores in the eastern tropical Pacific: **a.** ME0005A-14MC (5° 50.79' N, 86° 26.94' W, 2045 m), **b., c.** ME0005A-15MC (4° 36.82' N, 86° 42.24' W, 904 m), and **d.** Y69-106P (2° 59' N, 86° 33' W, 2870 m). The x-axis shows time in seconds with time zero representing the start of time resolved analysis, after the sample has been cleaned. The advantage of TRA is demonstrated by the multiple data points produced in the sequential dissolution, which reveals significant heterogeneity in these foraminiferal specimens. The y-axes show Mg/Ca and Sr/Ca (left axis) and Ca (ppm), Mg (ppb), and Sr (ppb) (right axis). The Sr/Ca in these specimens appears to be homogeneous relative to Mg/Ca. The calcification temperature is calculated based on the average of the five Mg/Ca values associated with the peak in Ca that appears near the beginning of the sequential dissolution. These Mg/Ca values are highlighted in yellow for each site. The Mg/Ca ratios near the ends of the runs are different between sites. This is probably due to incomplete dissolution of the samples, as suggested by Ca and Sr concentrations that are still significantly higher than blank values.

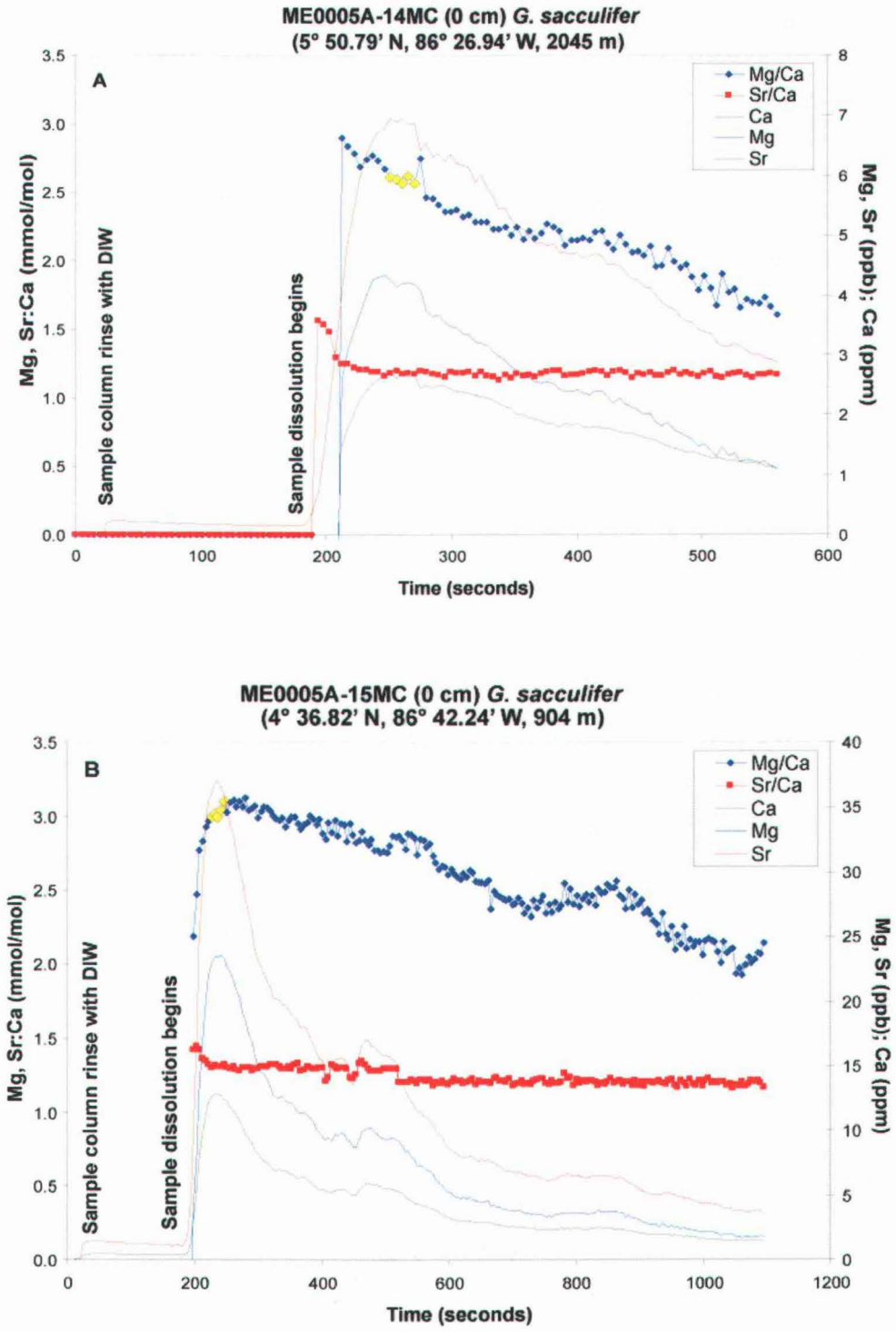
ME0005A-14MC (0 cm) G. sacculifer
(5° 50.79' N, 86° 26.94' W, 2045 m)
A
Mg/Ca
Sr/Ca
Ca
Mg
Sr
Sample column rinse with DIW
Sample dissolution begins
Mg, Sr:Ca (mmol/mol)
Mg, Sr (ppb); Ca (ppm)
Time (seconds)
ME0005A-15MC (0 cm) G. sacculifer
(4° 36.82' N, 86° 42.24' W, 904 m)
B
Mg/Ca
Sr/Ca
Ca
Mg
Sr
Sample column rinse with DIW
Sample dissolution begins
Mg, Sr:Ca (mmol/mol)
Mg, Sr (ppb); Ca (ppm)
Time (seconds)

Figure 3.2

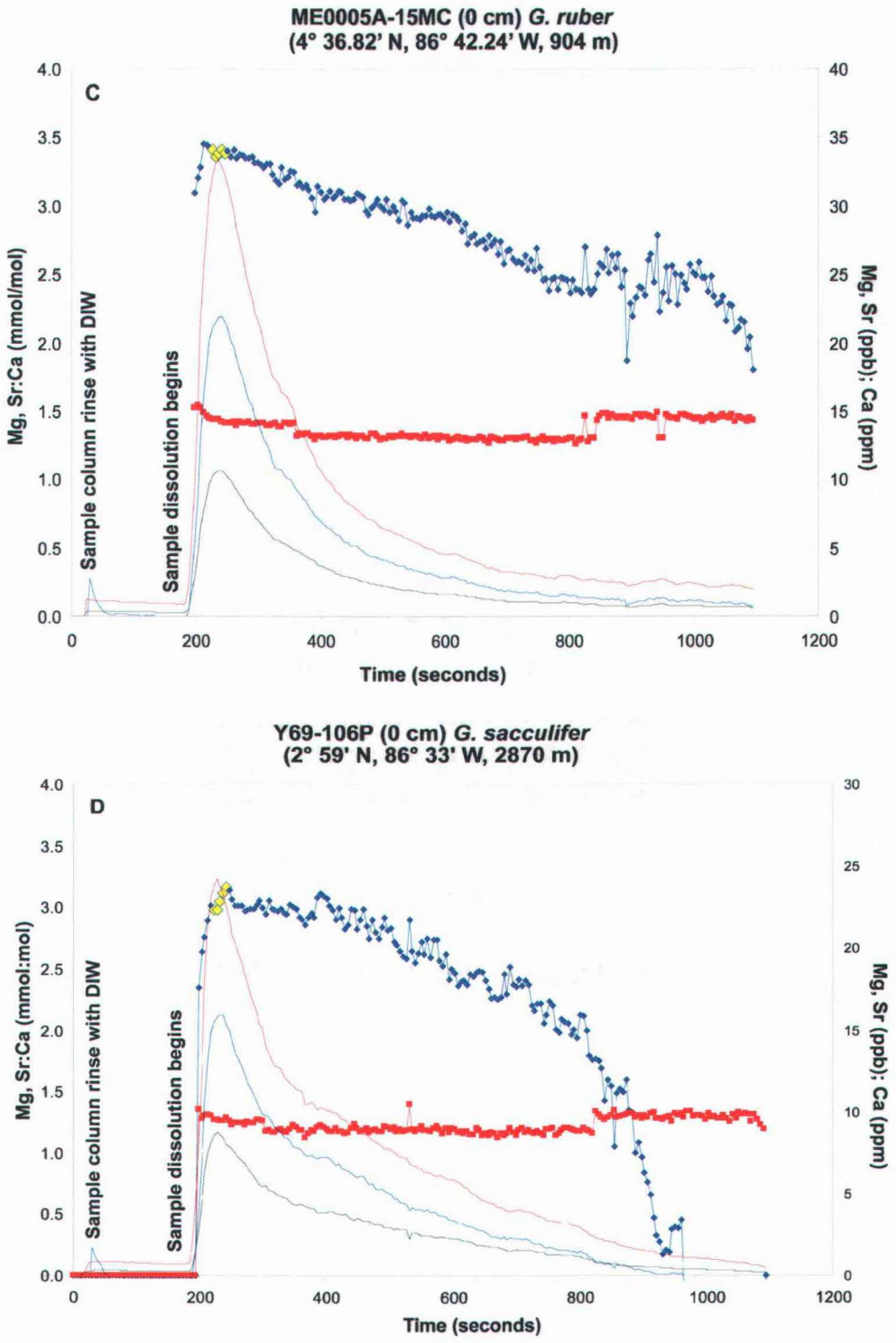

Figure 3.2 (cont'd.)

represent significant dissolution of calcite for these shells. Early ramp-up of Mg/Ca occurs in most samples at the beginning of dissolution. This is characteristic of a continuous flow system, and reflects diffusive mixing in the reagent stream, not a true change in shell Mg/Ca. As dilute acid is first introduced to the sample chamber, shell dissolution begins, and there is a gradual displacement of the blank eluate from the sample chamber.

One possible hypothesis to explain the gradual decline we observe in Mg/Ca is incongruent dissolution, in which the $MgCO_3$ that is present as a minor component within the test dissolves at a faster rate than $CaCO_3$. An alternative hypothesis is that the gradual decline in Mg/Ca is a result of ordered dissolution of different types of calcite in the test based on Mg content. Earlier experiments by Haley and Klinkhammer (2002) showed similar dissolution patterns for *G. sacculifer* from the Ontong Java Plateau. Their measurements of the planktonic foraminifer *Orbulina universa* consistently yielded distinct Mg/Ca "plateaus" that would not likely be generated by incongruent dissolution. Based on these observations and results of our partial dissolution experiment, which demonstrates that sequential dissolution is actually removing different forms of calcite in an ordered sequence (ie., primary calcite first, followed by secondary calcite), we prefer the latter hypothesis.

Under the assumption that Mg/Ca variability in the shells is primarily related to temperature, we calculated the Mg/Ca temperature using the culture calibration equation of Nürnberg et al. (1996) for *G. sacculifer* (Mg/Ca (mmol/mol) = 0.39exp[0.089 x T (°C)]) and a recent core top calibration (Lea et al., 2000) from the tropical Pacific for *G. ruber* (Mg/Ca (mmol/mol) = 0.30exp[0.089 x SST (°C)]; standard error = ±0.6°C). Eventually, we plan to develop species-specific calibrations based on our flow-through technique, but in the meantime we must apply existing calibrations. Since we expect that this method can extract calcification temperatures for a range of calcite concentrations, despite partial dissolution, it would be appropriate to apply culture calibrations, which do not contain built-in dissolution biases. In the absence of a recent culture calibration for *G. ruber*, we applied a recent

core top calibration (Lea et al., 2000) that is specific to our study region. However, we recognize that the use of this core top calibration introduces a dissolution bias that does not exist in our Mg/Ca data set.

In this experiment, we calculated "initial" calcification temperatures based on the average of the five Mg/Ca values associated with the peak in Ca that appears near the beginning of the sequential dissolution (Fig. 3.2). We choose these points because if there is high-Mg calcite remaining within a specimen (ie., it hasn't all been dissolved away), then it should dissolve first, thus corresponding to the Ca peak near the beginning of sequential dissolution. We also calculated the Ca-weighted mean temperature within the entire dissolution, excluding the initial "ramp-up" data. This mimics the value that would be determined in traditional batch dissolutions, assuming that the batch samples were cleaned properly.

Calcification temperatures for *G. ruber* and *G. sacculifer* calculated from the batch vs. the flow-through method using different published calibration equations are reported in Table 3.1. The calcification temperatures calculated from the flow-through method are consistently higher than those calculated from the batch method. Based on the calcification temperatures derived from the various calibration equations, *G. ruber* calcifies within the mixed layer, whereas *G. sacculifer* seems to calcify within the thermocline at this site, which is consistent with previously published plankton tow data from this region (Fairbanks et al., 1982).

To examine the effects of selective dissolution in seafloor samples, we compared core top Mg/Ca measurements in *G. sacculifer* from continuous and batch dissolution methods at three nearby sites with different water depths: ME0005A-15MC (904 m), ME0005A-14MC (2045 m), and Y69-106P (2870 m) (Fig. 3.3). Oxygen isotope measurements indicate that the multicore tops from 14MC and 15MC are late Holocene in age. The piston core top from Y69-106P is at least mid-Holocene in age. *G. sacculifer* (355-425 μm size fraction) is analyzed in all cores (*G. ruber* is essentially absent in the deeper cores due to dissolution). Core top ME0005A-14MC yields a slightly lower initial Mg/Ca ratio, and immediately shows a steep decline in

Table 3.1. Mg/Ca measurements (batch / **flow-through**) and comparison of batch vs. flow-through Mg/Ca-based calcification temperatures for samples shown in Fig. 2 using different existing calibration equations for *G. sacculifer* and *G. ruber*. Calculations based on the flow-through Mg/Ca ratio are in bold.

		CALCIFICATION TEMPERATURE (°C) (Batch method / **Flow-through method**)			
Sample (°C)	Mg/Ca (mmol/mol)	Lea et al. (2000)[a]	Nürnberg et al. (1996)[b]	Dekens et al. (2002)[c]	Actual SST[d] (WOA 98)
ME0005A-14MC (0 cm)					27.7
G. sacculifer	2.16 / **2.60**	N/A	19.2 / **21.3**	22.3	
ME0005A-15MC (0 cm)					27.4
G. sacculifer	2.63 / **3.03**	N/A	21.5 / **23.0**	N/A[c]	
G. ruber	2.68 / **3.39**	24.6 / **27.2**	N/A	N/A[c]	
Y69-106P (0 cm)					26.5
G. sacculifer	2.57 / **3.06**	N/A	21.2 / **23.1**	24.6	

a. Lea et al. (2000) represents a core top calibration for *G. ruber* (Mg/Ca (mmol/mol) = 0.30exp[0.089 x SST (°C)]) in the equatorial Pacific.
b. Nürnberg et al. (1996) represents a culture calibration for *G. sacculifer* (Mg/Ca (mmol/mol) = 0.39exp[0.089 x T (°C)]).
c. Dekens et al. (2002) represents a core top calibration for *G. sacculifer* (Mg/Ca (mmol/mol) = 0.37exp 0.09[T – 0.36(core depth km – 2.0°C]) from the equatorial Pacific. The Dekens et al. (2002) calibration could not be applied to Site ME0005A-15MC because the site is too shallow (904 m); this calibration equation only applies to depths > 1.6 km. Also, since this calibration contains a dissolution correction, it was unnecessary to apply it to flow-through Mg/Ca ratios.
d. Annual average SST for each site taken from World Ocean Atlas (1998).

Figure 3.3. Depth transect showing **a.** Mg/Ca and **b.** Calcification temperatures from *G. sacculifer* for batch vs. flow-through in three cores from the eastern tropical Pacific: ME0005A-15MC (4° 36.82' N, 86° 42.24' W, 904 m), ME0005A-14MC (5° 50.79' N, 86° 26.94' W, 2045 m), and Y69-106P (2° 59' N, 86° 33' W, 2870 m). Mg/Ca was converted to calcification temperature using the culture calibration equation of Nürnberg et al. (1996) for *G. sacculifer* (Mg/Ca (mmol/mol) = 0.39exp[0.089 x T (°C)]). The batch dissolution values (large symbols on the y-axis) were obtained by calculating a Ca-weighted average for each sample.

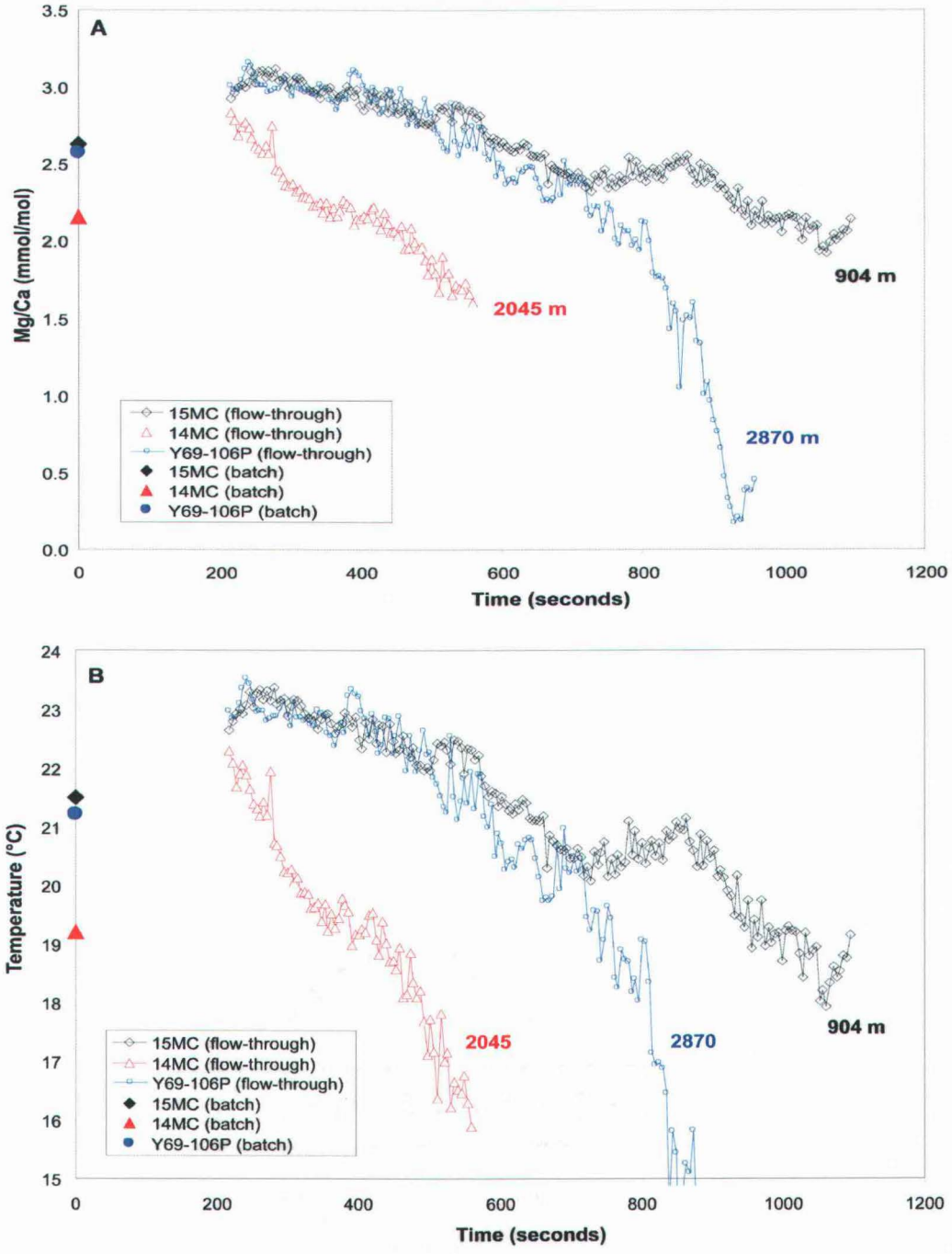
A
Mg/Ca (mmol/mol)
3.5
3.0
2.5
2.0
1.5
1.0
0.5
0.0
0
200
400
600
800
1000
1200
Time (seconds)
904 m
2045 m
2870 m
15MC (flow-through)
14MC (flow-through)
Y69-106P (flow-through)
15MC (batch)
14MC (batch)
Y69-106P (batch)
B
Temperature (°C)
24
23
22
21
20
19
18
17
16
15
0
200
400
600
800
1000
1200
Time (seconds)
904 m
2045
2870
15MC (flow-through)
14MC (flow-through)
Y69-106P (flow-through)
15MC (batch)
14MC (batch)
Y69-106P (batch)

Figure 3.3.

Mg/Ca during sequential dissolution. The other two cores shown in Fig. 3.3 have a modest plateau in Mg/Ca at the beginning of the dissolution, followed by a steeper decline resembling that of 14MC. Although not the deepest site, it might be that 14MC is showing a larger dissolution effect than the other two cores. The enhanced dissolution in 14MC relative to the deeper site (Y69-106P) may reflect a core top age difference, since the deep Pacific is thought to have undergone a mid-Holocene change in dissolved carbonate ion concentration (Keir, 1984). We would expect that if specimens from 14MC are slightly more dissolved, they would contain less primary calcite, thus yielding less of a "plateau" near the beginning of dissolution, as seen in the other cores. The Mg/Ca pattern in14MC resembles the latter parts (from ~550 seconds to the end) of the sequential dissolution series in the other two cores (Fig. 3.3). It is likely that the majority (though not all, or we would not obtain an initial Mg/Ca ratio that is so close to that of the other cores) of the early-stage calcite in 14MC has dissolved on the seafloor.

The Mg/Ca ratios near the end of the analysis are notably different between sites (Figs. 3.2, 3.3). Lower Mg/Ca ratios may be attributed to lower calcification temperatures, biomineralization effects, or a combination of both. Increased noise occurs in the system after the majority of the sample has dissolved (after the initial peaks in Ca), making the true endpoint (complete dissolution) very difficult to identify. Incomplete sample dissolution would likely explain these differences in the Mg/Ca ratios between sites. We are addressing this problem with further experimentation.

Using the culture calibration equation of Nürnberg et al. (1996) for *G. sacculifer* to calculate temperature, we observe a ~1.5-2.0°C discrepancy between batch and continuous temperatures at all three sites shown in Fig. 3.3. Since our primary goal for purposes of estimating paleotemperature is to extract the highest Mg/Ca values remaining in the calcite samples, we are encouraged that the initial temperatures in the core tops from all three sites are quite similar and reflect a depth habitat within the thermocline, which is typical for *G. sacculifer* (Fairbanks et al., 1982). This suggests

that as long as some of the dissolution-sensitive (ontogenetic) calcite is preserved, even in moderately to heavily dissolved samples, it can still be detected via sequential dissolution.

To test the accuracy of the flow-through technique, we compared Mg/Ca-based temperature estimates from *G. ruber* (based on the preliminary temperature calibration of Lea et al., 2000) in the core top ME0005A-15MC with a series of World Ocean Atlas (WOA 98) temperature profiles (annual, seasonal, and flux-weighted averages) from the same site and determined the corresponding calcification depths of this species for batch vs. continuous methods (Fig. 3.4). The calcification temperature derived from sequential dissolution was in good agreement (within 0.2°C) with WOA 98 SST data, and corresponded to a calcification depth range of ~0-20 m, which is typical for *G. ruber*, a mixed layer-dwelling organism (Fairbanks et al., 1982; Faul et al., 2000). In this experiment, ~75-80% of the calcite had a Mg/Ca ratio consistent with mean annual temperature in the upper ~30 m. The remaining calcite had a Mg/Ca ratio consistent with calcification between 30-50 m. The Ca-weighted "batch" SST estimate of 25.9°C was within the range of that calculated by Lea et al. (2000) for this region, and corresponded to a depth of ~35 m, which lies within the thermocline at this site. This lower SST estimate may reflect the contribution of secondary calcite. There is also a bias associated with applying a core top calibration to these data, since the "initial" Mg/Ca ratios used in our temperature calculation do not contain the dissolution effect that is inherent in a core top calibration. Therefore, our SST estimates from *G. ruber* are probably slightly higher than the true calcification temperatures (also see Table 3.1).

These results are not significantly affected by seasonality at the study site. Despite seasonal upwelling, the seasonal SST range (shown in Fig. 3.4) in this region is only ~1.5°C (ranging from a low of ~26.5°C in October/November/December, to a high of ~28°C in April/May/June) owing to a strong, shallow pycnocline that hinders vertical mixing, and there is essentially no seasonal variability at depths greater than 30 m (WOA 1998). Previous studies (Curry et al., 1983; Thunell et al., 1983; Thunell and

Figure 3.4: Comparison of batch and continuous Mg/Ca-based temperature estimates for *G. ruber* from a late Holocene Cocos Ridge core top (ME0005A-15MC, 4°36.82'N, 86°42.24'W, 904 m) against World Ocean Atlas (1998) temperature profiles. The blue line represents the initial Mg/Ca values obtained during sequential dissolution (see text for explanation of calculations). The red line represents the batch (Ca-weighted average) dissolution Mg/Ca value. The annual average temperature profile is encompassed by the warmest (April/May June, or AMJ) and coldest (October/November/December, or OND) seasonal profiles, so as to demonstrate the potential error associated with seasonal variability in this region. The thick black dotted line represents the flux-weighted temperature profile, which is based on the seasonal flux of *G. ruber* in the Panama Basin region (data from Thunell et al., 1983; see Fig. 3.5). When seasonal variability is taken into account, the calcification depth of *G. ruber*, as predicted by the batch dissolution is 30 ± 1 m, and the continuous dissolution predicts a calcification depth of 10 ± 10 m. Even when seasonality is taken into account, the continuous method still predicts *G. ruber* calcification within the upper 20 m.

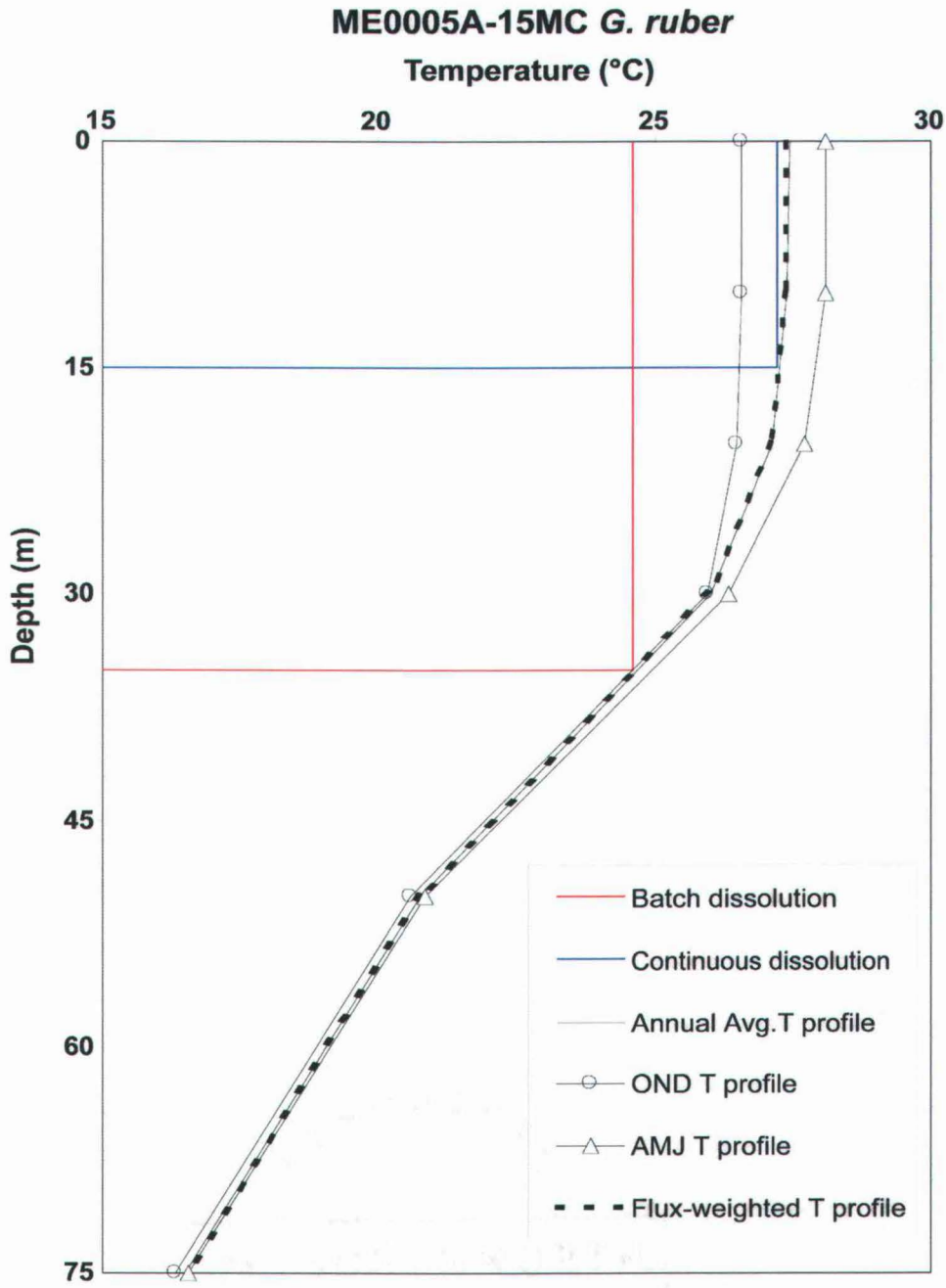
ME0005A-15MC G. ruber
Temperature (°C)
15
20
25
30
0
15
30
45
60
75
Depth (m)
Batch dissolution
Continuous dissolution
Annual Avg.T profile
OND T profile
AMJ T profile
Flux-weighted T profile

Figure 3.4:

.

Reynolds, 1984) have documented seasonal changes in foraminiferal flux in the Panama Basin region (Fig. 3.5). The seasonal fluxes for *G. ruber* were used to calculate a flux-weighted temperature profile in Fig. 3.4, which is essentially identical to the annual average temperature profile.

Conclusions

The flow-through leaching procedure allows us to directly observe heterogeneity of Mg/Ca in biogenic calcite, and addresses issues of contaminant phases and dissolution in the measurement of Mg/Ca. Multiple cleaning experiments monitored with TRA have enabled us to optimize the system for complete removal of contaminant-phase Mg prior to dissolution. Preliminary experiments suggest that 1) The flow-through leaching method closely mimics sea floor dissolution, effectively separating different calcite domains (primary vs. secondary) based on Mg content; 2) Mg distribution in foraminiferal calcite is heterogeneous with primary calcite yielding a higher Mg content than secondary calcite; 3) The flow-through leaching method yields reliable estimates of calcification temperature, despite partial dissolution of foraminiferal shells. Although we cannot presently rule out the incongruent dissolution hypothesis, the body of evidence shown here strongly favors our hypothesis that ordered dissolution during flow-through analysis removes high-Mg (primary) calcite first, followed by low-Mg (secondary) calcite, which provides a unique opportunity to extract initial calcification temperature (based on the Mg/Ca of the primary calcite), despite problems of shell heterogeneity and dissolution.

These results are preliminary, and only represent regional (eastern tropical Pacific) findings from two species of planktonic foraminifera. Different species have different calcification schemes that affect the relative abundances of primary and secondary calcite. In addition to Mg content, physical factors such as shape, morphology, and crystallinity may play a role in the observed order and patterns of dissolution (Rushdi et al., 1998). Further work is needed to deconvolve temperature and biomineralization effects on the Mg content of primary versus secondary calcite. Additional testing will

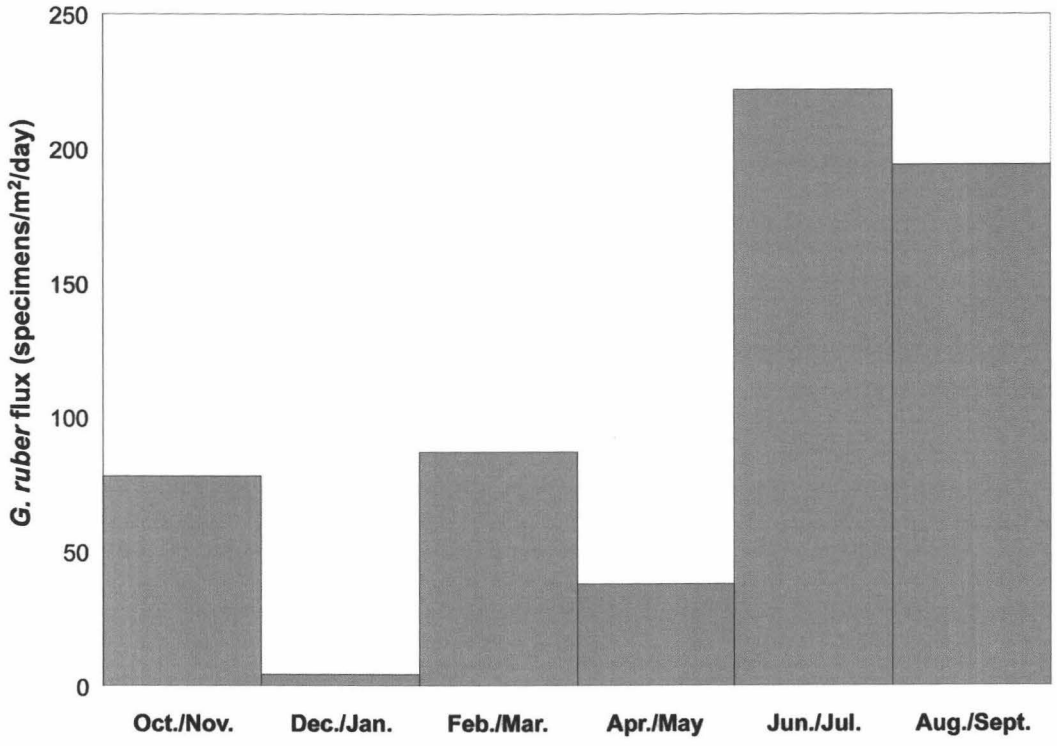

Figure 3.5: Seasonal flux data from Thunell et al. (1983) for *G. ruber* from a sediment trap at 890 m in the Panama Basin region (5° 21' N, 81° 53' W). Foraminiferal specimens are from the 250-500 μm size fraction. These flux data were used to calculate the flux-weighted temperature profile in Fig. 3.4.

also involve measuring core top Mg/Ca from several other depth transects in different ocean basins to see if the flow-through method consistently documents Mg heterogeneity in foraminiferal tests and yields accurate SST estimates despite exposure to water column and seafloor dissolution.

4. EASTERN TROPICAL PACIFIC PALEOSALINITY AND GLOBAL CLIMATE CHANGE

Heather M. Benway, Alan C. Mix, Brian A. Haley, and Gary P. Klinkhammer

Science
http://www.sciencemag.org
To be submitted August 2005

Abstract

Relatively low sea-surface salinities west of Central America (Fig. 4.1) reflect high net precipitation, supported in part by vapor transport across the Panama Isthmus (Zaucker et al., 1994; Benway and Mix, 2004). Such transport helps to maintain the salinity contrast between the Atlantic and Pacific Oceans, an important control of global thermohaline circulation, oceanic heat transport, and climate (Zaucker et al., 1994; Rahmstorf, 1995). Here we report changes in temperature, salinity, and pycnocline structure in the Eastern Pacific Warm Pool (EPWP) over the last 30,000 years, based on oxygen isotopes and Mg/Ca ratios in foraminifera. Comparison of these records to paleoclimate reconstructions from the Caribbean Sea, Atlantic Ocean, and polar ice cores suggests that variations in net precipitation over the EPWP are associated with millennial-scale climate changes in the northern hemisphere. Lack of significant glacial-interglacial salinity contrast suggests that tropical changes operate independently of high-latitude ice sheets. Although models (Zhang and Delworth, 2005) predict ITCZ and salinity responses to changes in North Atlantic Deep Water formation, tropical Pacific paleosalinity changes lead North Atlantic circulation changes by ~500 years, suggesting that low-latitude mechanisms and an inter-ocean salt oscillator may also contribute to millennial-scale global climate variability.

Introduction

Although the role of vapor transport in maintaining salinity contrast between oceans is known (Zaucker et al., 1994), variations through time are unconstrained. Models suggest that vapor transport increases during warm phases of the El Niño-Southern Oscillation (ENSO) (Schmittner et al., 2000), that long-term ENSO variability may modify ocean salt balance and North Atlantic Deep Water formation (Schmittner and Clement, 2002), and that vapor transport increased during glacial times due to stronger winds (Hostetler and Mix, 1999).

Chemical measurements of foraminiferal shells preserved in marine sediments help to constrain changes in sea-surface salinity, and by inference, net precipitation in

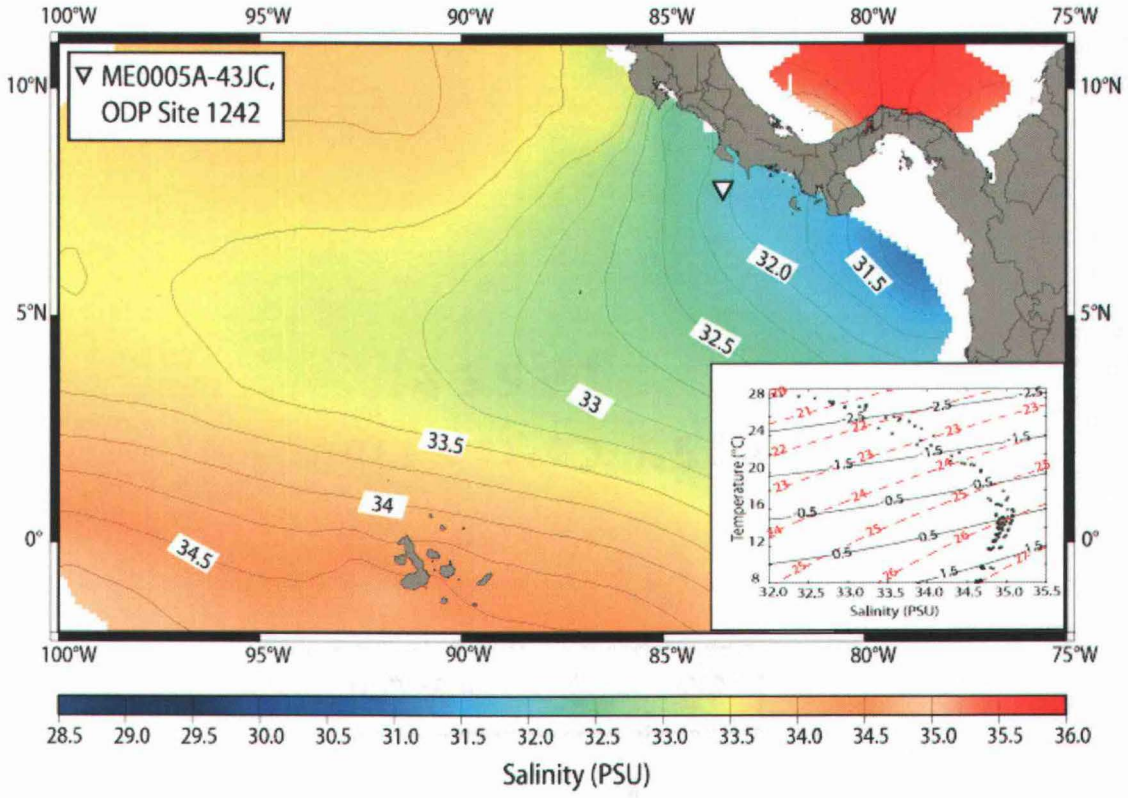

Figure 4.1. Annual average salinity (PSU) for the Panama Bight and western Caribbean (World Ocean Atlas, 1998). Pacific sites (ME0005A-43JC: 7° 51.35'N, 83° 36.50'W, 1,368 m and ODP Site 1242: 7° 51.35'N, 83° 36.42'W, 1,364 m) used in this study are indicated. **Inset.** T-S diagram (World Ocean Atlas, 1998) of the Panama Bight region with isopycnals (red dotted) and predicted $\delta^{18}O_c$ isolines (black solid) calculated from temperature and salinity (Bemis et al., 1998; Thunell et al., 1999) assuming modern regional $\delta^{18}O_{sw}$-S (Benway and Mix, 2004).

the EPWP and its relationship to global climate and deep ocean circulation. Sediment cores ME0005A-43JC (7° 51.35'N, 83° 36.50'W, 1,368 m) and Ocean Drilling Program (ODP) Site 1242 (7° 51.35'N, 83° 36.42'W, 1,364 m) (Fig. 4.1) provide well-preserved replicate records sampled at ~200 year intervals over the past 30,000 years. Radiocarbon chronologies are expressed as calendar ages between 0 and 20 ka (Stuiver and Reimer, 1993), and correlation of stable isotope records to other well dated records extends age control to 30 ka (Shackleton et al., 2000) (Appendix 3). Sedimentation rates are 10-12 cm ky^{-1}, sufficient to resolve millennial-scale events.

The oxygen isotope composition of foraminiferal calcite ($\delta^{18}O_c$) reflects both temperature and ambient seawater composition ($\delta^{18}O_{sw}$). Estimates of calcification temperature from Mg/Ca measurements of *Globigerinoides ruber*, based on flow-through leaching (Haley and Klinkhammer, 2002; Benway et al., 2003) deconvolve the temperature and watermass effects on $\delta^{18}O_c$, and modern $\delta^{18}O_{sw}$ –S relationships (Benway and Mix, 2004) provide a basis for estimating paleosalinity. Over the past ~30 ky, changes in global sealevel provide reasonable corrections for the global changes in $\delta^{18}O_{sw}$ driven by changing ice volume (Waelbroeck et al., 2002; Clark and Mix, 2002).

Regional core-top $\delta^{18}O_c$ and Mg/Ca measurements confirm near-surface calcification for *G. ruber* (Fig. 4.2). The $\delta^{18}O_c$ contrast between two species of planktonic foraminifera, *G. ruber* and *Neogloboquadrina dutertrei*, which lives in the thermocline (Spero et al., 2003) (Fig 4.2) provides an estimate of upper ocean density gradients. The primary control of $\delta^{18}O_c$ in regional surface waters is salinity (driven by net precipitation), whereas in subsurface waters it is temperature (related to upwelling; Fig. 4.1, inset).

Results and Discussion

Over the past 30 ky, sharp decreases in *G. ruber* $\delta^{18}O_c$ reflect the deglacial transition at 11.2 ka and 16.3 ka (Fig. 4.3a). The isotopic contrast between *G. ruber* and *N. dutertrei* (Fig. 4.3b) reveals significant differences between glacial (15-25 ka,

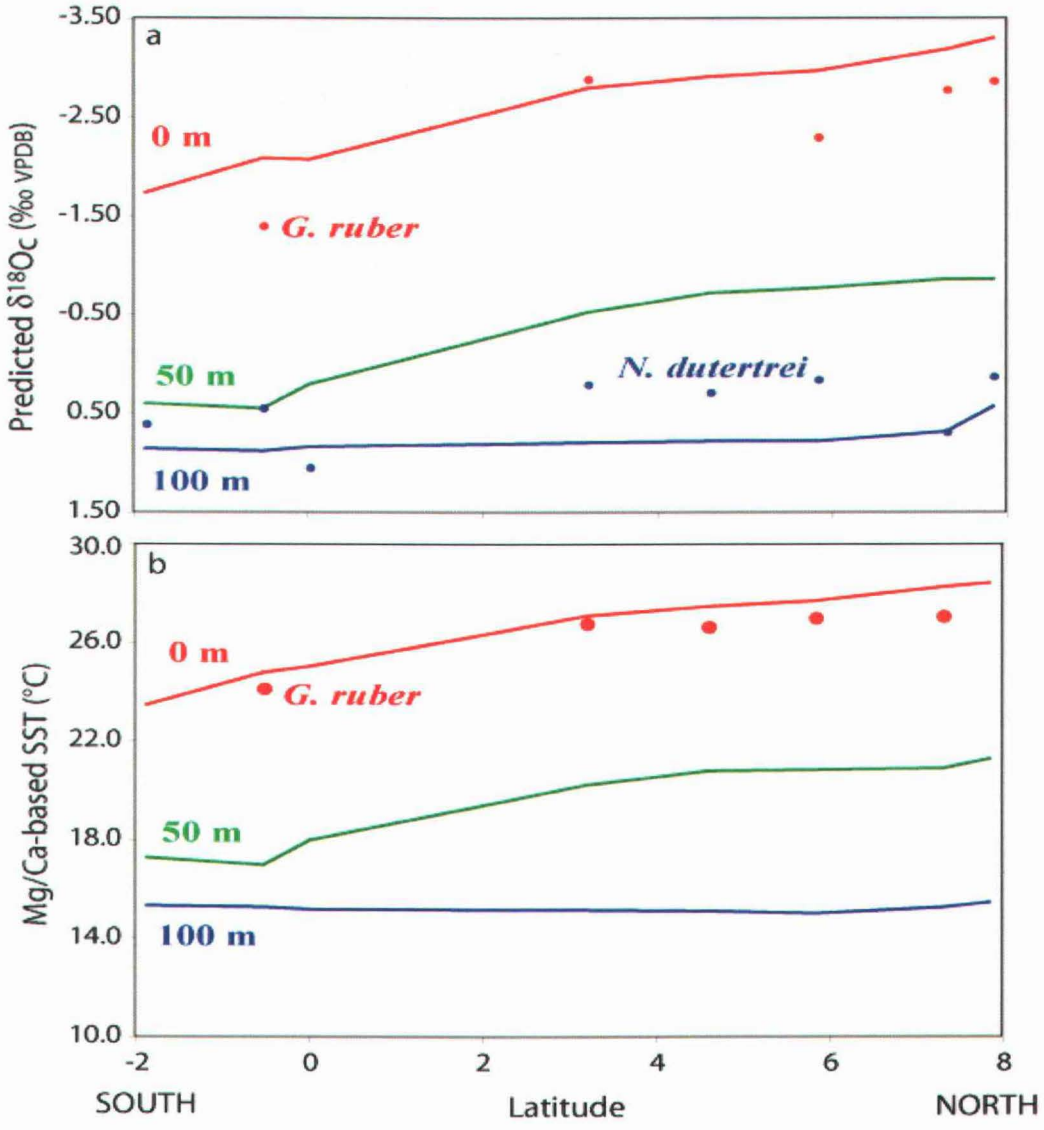

Figure 4.2. A north-south transect of sites in the eastern tropical Pacific with corresponding profiles (World Ocean Atlas (WOA), 1998) of **a.** Predicted $\delta^{18}O_c$ at 0, 50, and 100 m, which is calculated from cultured *O. universa* high light (0 m) and low light (50 and 100 m) equations (Bemis et al., 1998). Red (blue) symbols indicate measured $\delta^{18}O_c$ of *G. ruber* (*N. dutertrei*) in multi-core tops at each site. **b.** Annual average temperature at 0, 50, and 100 m (World Ocean Atlas, 1998). Red symbols indicate Mg/Ca-based temperature estimates from *G. ruber* in multi-core tops at each site. Core top Mg/Ca and $\delta^{18}O_c$ measurements verify that the depth habitat of *G. ruber* is in the upper mixed layer. The $\delta^{18}O_c$ multicore data for *N. dutertrei* verify that the depth habitat of this species is near the base of the thermocline, which is ~50-75 m at our coring sites (ME0005A-43JC, ODP 1242). All multicore core top data are available in Appendix 4.

Figure 4.3. Data from ME0005A-43JC (filled symbols) and ODP Site 1242 (unfilled symbols). Ages reported in calendar ky before present. AMS ^{14}C dates for ME0005A-43JC are indicated by filled circles on age axis with 2-sigma error bars (see Appendix 3). **a,** $\delta^{18}O_c$ for *G. ruber* (white) and *N. dutertrei*. **b,** $\delta^{18}O_c$ difference between *G. ruber* and *N. dutertrei*, indicating upper ocean contrast above the pycnocline. **c,** Mg/Ca-based temperature for *G. ruber*. Mg/Ca was converted to temperature using Mg/Ca = 0.38Exp(0.090T) (Anand et al., 2003). Modern annual average surface temperature (World Ocean Atlas, 1998) is indicated on the y-axis. **d,** $\delta^{18}O_{sw}$ estimates calculated from *G. ruber* Mg/Ca and $\delta^{18}O_c$ (Bemis et al., 1998; Thunell et al., 1999) and corrected for ice volume changes (Waelbroeck et al., 2002; Clark and Mix, 2002). The potential range of $\delta^{18}O_{sw}$ uncertainty associated with ice volume change is indicated by the two red curves. The bold curve indicates a scaling of 0.01‰ m^{-1} while the thin dashed curve indicates a scaling of 0.0075‰ m^{-1} decrease in relative sea level (RSL). The resulting range of uncertainty in the corrected $\delta^{18}O_{sw}$ is indicated by the corresponding bold and thin dashed black smoothed $\delta^{18}O_{sw}$ records. The modern measured $\delta^{18}O_{sw}$ (Benway and Mix, 2004) is indicated on the y-axis. For the combined records of the two sites a Gaussian smoothing function (time step = 0.2 ky; filter width = 0.8 ky) was applied. All data for both cores are available in Appendices 5 and 6.

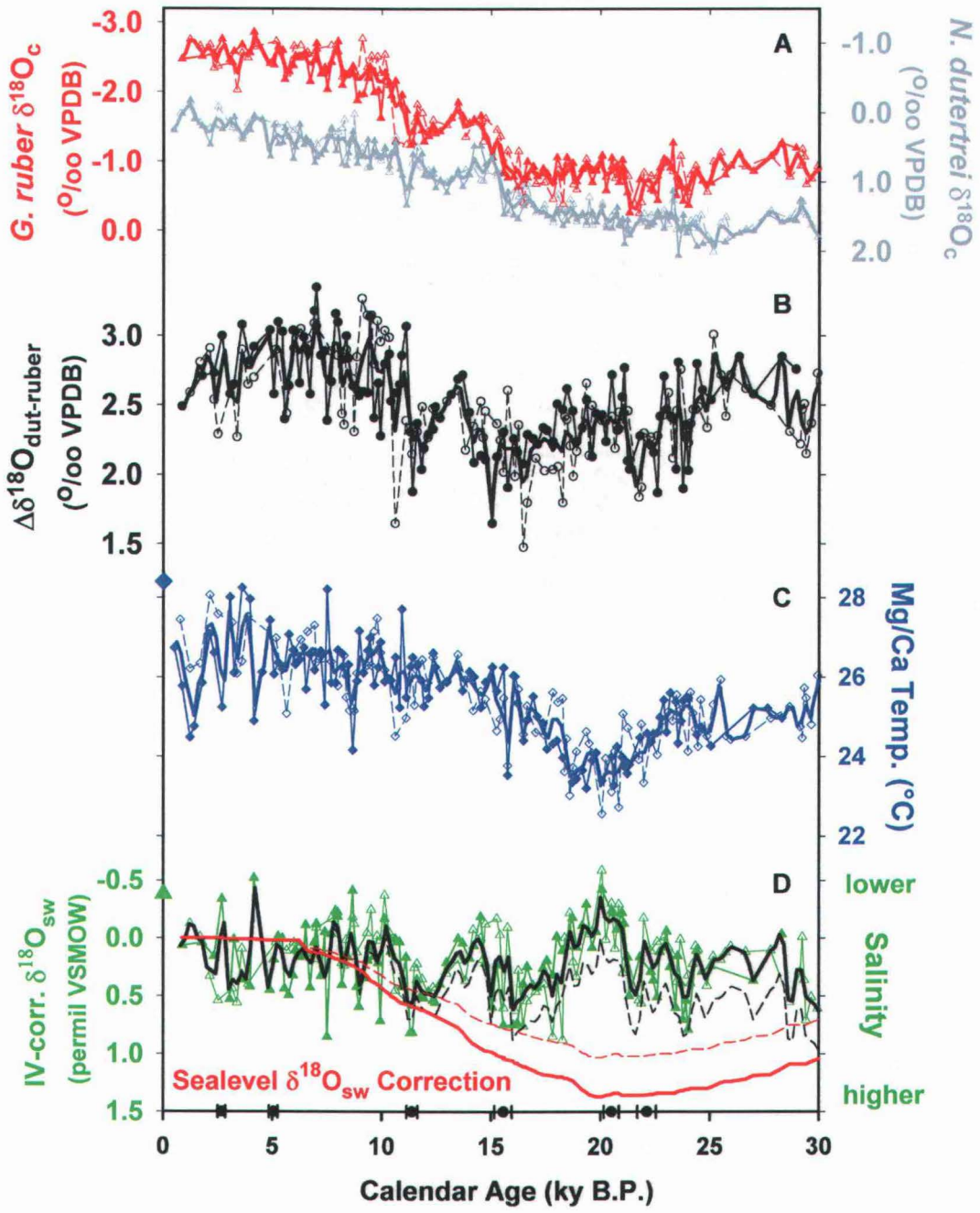
G. ruber δ18Oc (‰ VPDB)
N. dutertrei δ18Oc (‰ VPDB)
Δδ18Odut-ruber (‰ VPDB)
Mg/Ca Temp. (°C)
IV-corr. δ18Osw (permil VSMOW)
Salinity
lower
higher
Sealevel δ18Osw Correction
A
B
C
D
Calendar Age (ky B.P.)

Figure 4.3.

2.3 ± 0.3 ‰) and Holocene (0-10 ka, 2.8 ± 0.3 ‰) times, with low but variable contrast during the deglacial transition (10-15 ka, 2.4 ± 0.3 ‰). Mg/Ca in *G. ruber* (Fig. 4.3c) reveals a glacial (19-23 ka) to late Holocene (3-5 ka) temperature change of 2.8° ± 0.8°C. Abrupt warming of ~1-2°C, which started at ~19 ka, would reduce *G. ruber* $\delta^{18}O_c$ by ~0.6 ‰, suggesting that much of the glacial-interglacial change in the isotopic difference between *G. ruber* and *N. dutertrei* may reflect changes in sea-surface temperatures. The implied lack of glacial-interglacial temperature changes in pycnocline waters helps to explain apparent conflicts between chemical and faunal paleotemperature proxies in the equatorial cold tongue upwelling system (Koutavas et al., 2002; Feldberg and Mix, 2003). The difference in timing of changes in Mg/Ca temperature and $\Delta\delta^{18}O_{dut\text{-}ruber}$, however, indicates that changes in subsurface watermasses were decoupled from changes in sea-surface temperature; for example, an increase in $\delta^{18}O$ of *N. dutertrei* and relatively high $\Delta\delta^{18}O_{dut\text{-}ruber}$ from 13-14 ka coincides with the Antarctic Cold Reversal, consistent with transmission of southern ocean climate changes in subsurface watermasses.

Removal of local Mg/Ca temperature and global ice volume (Waelbroeck et al., 2002; Clark and Mix, 2002) effects on *G. ruber* $\delta^{18}O_c$ yields an estimate of near-surface ocean $\delta^{18}O_{sw}$ (Fig. 4.3d). Uncertainties in ice-volume corrections have negligible effects on the timing or amplitude of the observed millennial-scale $\delta^{18}O_{sw}$ changes (Fig. 4.3d). Presently, about half of the precipitation in the EPWP region reflects long-distance transport (Benway and Mix, 2004). Under this assumption, sea-surface paleosalinity changes (Fig. 4.4c) are large (up to ~4-5 PSU) and occur every ~3-5 ky during glacial time (~15-25 ka), and more frequently during the Holocene (0-10 ka). Paleosalinity (or $\delta^{18}O_{sw}$) changes in the EPWP exceed those of the Caribbean (Schmidt et al., 2004) and the western Pacific (Stott et al., 2002). They are weakly linked to pycnocline intensity changes (r= -0.6) during the glacial interval (Figs. 4.3, 4.4). No significant contrast is found between paleosalinities averaged over the glacial (~15-25 ka, 34.8 ± 1.2 PSU) and Holocene (~0-10 ka, 34.5 ± 1.1 PSU) intervals,

Figure 4.4. Comparison of EPWP paleosalinity to other paleoclimate reconstructions. **a.** Sea-surface temperature (SST) reconstructions from Cariaco Basin core PL07-39PC (Lea et al., 2003) based on Mg/Ca (red) and subtropical northeast Atlantic core SU8118 (Bard, 2002) based on alkenones (black). **b,** Measured color reflectance (550 nm) (Peterson et al., 2000) and % Ti (Haug et al., 2001) of Cariaco Basin sediments, ODP Site 1002 Lower reflectance (darker, clay-rich sediment) and higher % Ti (increased terrigenous sediment) implying wetter conditions in northern South America. **c,** $\delta^{18}O_{sw}$ and estimated paleosalinity from the EPWP (ME0005A-43JC and ODP Site 1242) (Benway and Mix, 2004) and the Caribbean (Schmidt et al., 2004). The same ice volume correction is applied to both records (see bold red curve, Fig. 4.3d), and two separate salinity scales are shown, based on regional $\delta^{18}O$-S (Benway and Mix, 2004; Schmidt et al., 2004). Black circles indicate Caribbean radiocarbon age control points with 2-sigma error bars. Pacific radiocarbon age control points are shown in Fig. 4.3d. **d,** Estimates of interbasin salinity contrast based on differencing Pacific and Caribbean (Schmidt et al., 2004) $\delta^{18}O_{sw}$. The higher resolution Pacific record was first placed on the Caribbean time scale using Gaussian interpolation, and then the records were differenced and the result smoothed (0.2 ky time step, filter width = 0.8 ky). The gray lines reflect maximum age model error in the interbasin contrast record, based on 2-sigma ranges in Pacific and Caribbean radiocarbon dates. **e,** $^{231}Pa/^{230}Th$ ratios (calculated from measured ^{238}U activity) from Bermuda rise (McManus et al., 2004), indicating strength of Atlantic meridional overturning circulation (MOC). The gray lines reflect maximum age model error in the MOC record, based on 2-sigma ranges in Bermuda Rise radiocarbon dates. **f,** GISP2 $\delta^{18}O_{ice}$ (Grootes and Stuiver, 1997), indicating high latitude air temperatures. Cold (blue shaded bars) and warm (or sealevel rise) events (red shaded bars) of the last 30 ky are indicated, with cold (warm) events corresponding to high (low) salinity and reduced (increased) MOC. 8 ka = 8.2 ka event; YD = Younger Dryas; HE-1, 2, 3 = Heinrich events; 19 ka = earliest postglacial sealevel rise; T-1A = Termination or meltwater pulse (MWP)-1A; T-1B = Termination or MWP-1B.

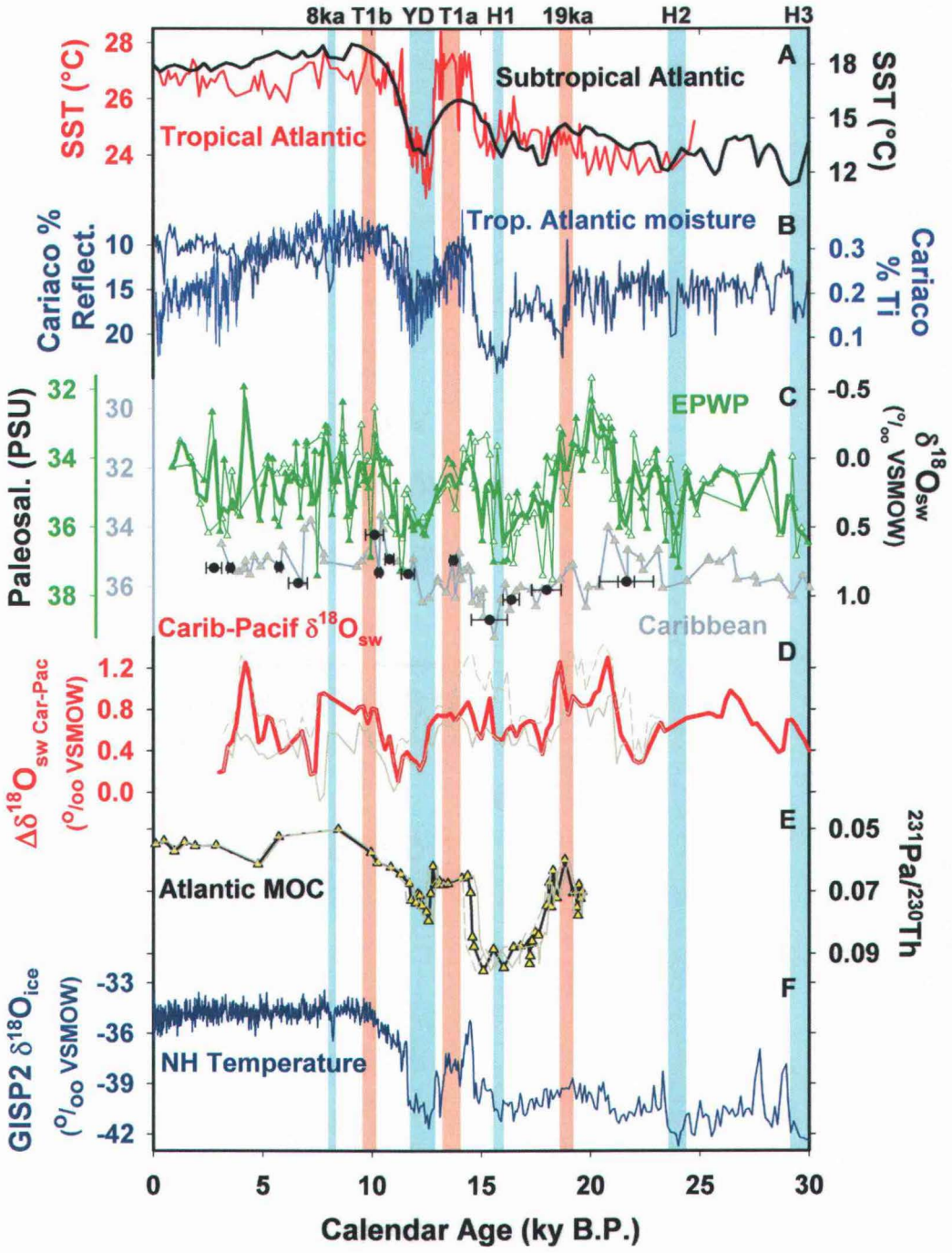
8ka T1b YD T1a H1 19ka H2 H3
SST (°C)
28
26
24
Tropical Atlantic
Subtropical Atlantic
A
18
15
12
SST (°C)
Cariaco % Reflect.
10
15
20
Trop. Atlantic moisture
B
0.3
0.2
0.1
Cariaco % Ti
Paleosal. (PSU)
32
34
36
38
30
32
34
36
EPWP
C
-0.5
0.0
0.5
1.0
δ18Osw (‰ VSMOW)
Carib-Pacif δ18Osw
Caribbean
D
Δδ18Osw Car-Pac (‰ VSMOW)
1.2
0.8
0.4
0.0
E
Atlantic MOC
0.05
0.07
0.09
231Pa/230Th
GISP2 δ18Oice (‰ VSMOW)
-33
-36
-39
-42
F
NH Temperature
0
5
10
15
20
25
30
Calendar Age (ky B.P.)

Figure 4.4.

suggesting that there is little or no direct effect of glacial boundary conditions on surface ocean salinities in the EPWP.

A calculation of differences between EPWP $\delta^{18}O_{sw}$ and Caribbean $\delta^{18}O_{sw}$ (Schmidt et al., 2004) provides an estimate of changing interbasin salinity contrast that, if representative of basin-scale trends, qualitatively reflects changes in vapor transport (Fig. 4.4d). Comparison of changes in Pacific paleosalinity and interbasin salinity contrast with climatic events elsewhere (Fig. 4.4) points toward plausible climate mechanisms. Relatively low paleosalinities in the EPWP are associated with key climate events documented in the northern hemisphere, including intervals of sea-level rise (the 19 ka early rise and Terminations 1a and 1b (Clark and Mix, 2002)), warmth in the tropical (Lea et al., 2003) and subtropical (Bard, 2002) North Atlantic and in Greenland (the early Holocene, the Bølling/Allerød interval, and a weak event near 19 ka) (Grootes and Stuiver, 1997), increased terrigenous flux in the Cariaco Basin (Peterson et al., 2000; Haug et al., 2001), and high rates of Atlantic meridional overturning circulation (MOC) indicated by $^{231}Pa/^{230}Th$ (McManus et al., 2004) (Fig. 4.4). High Pacific paleosalinities are associated with cooling in the North Atlantic and Greenland and reduced Atlantic thermohaline overturn, including Heinrich Events 1, 2, and 3, the Younger Dryas period, and possible Holocene events near 4-5 ka and 8-8.5 ka.

Variations of terrigenous sediments in Cariaco Basin have been linked to high interstadial rainfall in northern South America and a higher net export of moisture from the Atlantic to the Pacific during northward excursions of the ITCZ (Peterson et al., 2000). In a modeled response to reduced Atlantic meridional overturning circulation (MOC), North Atlantic cooling displaces the ITCZ southward, bringing cool, dry conditions to northern South America and the EPWP (Zhang and Delworth, 2005), consistent at first glance with our observation of higher EPWP paleosalinity during cold events (Fig. 4.4c). However, in modern boreal summer, when the ITCZ moves northward, the westerly Choco Jet delivers Pacific moisture to northern Columbia (Martínez et al., 2003), whereas in boreal winter, the ITCZ migrates

southward, northeasterly trades intensify, westward vapor transport increases (Weyl, 1968), and salinities in the EPWP region are at a seasonal minimum (World Ocean Atlas, 1998). If the modern seasonal cycle serves as a model for past variations, it is unlikely that ITCZ migration alone can explain the Pacific paleosalinity variations.

Cross-spectral analysis reveals that interbasin salinity contrast (inferred vapor transport) leads changes in Atlantic MOC (McManus et al., 2004) at periods of 3-5 ky and Greenland temperature (Grootes and Stuiver, 1997) at periods of 1.0-1.5 ky, suggesting that the observed paleosalinity changes are not simple responses to events in the North Atlantic. Potential errors in the Pacific and Caribbean chronologies are calculated from 2-sigma ranges in the radiocarbon dates. The lead of interbasin salinity contrast over Atlantic MOC is robust, but the lead over Greenland temperature is sensitive to age model errors. Given this phasing, it is likely that North Atlantic circulation is influenced by changes in westward vapor transport, via control of the North Atlantic salinity budget and thermohaline overturn, as originally suggested by Weyl (1968). The sensitivity of this coupled system may depend on climate stability and the mean state of the North Atlantic (Schmittner and Clement, 2002); for example additional responses of the ITCZ to North Atlantic cooling may also contribute to the coupled system.

Because the Pacific and Caribbean sites are in the same latitudinal band, changes in mean ITCZ position and/or intensity would yield a similar paleosalinity response at both sites (and thus little or no change in the interbasin contrast), whereas changes in westward vapor transport would increase the inter-basin salinity contrast. Although variations in EPWP and Caribbean (Schmidt et al., 2004) $\delta^{18}O_{sw}$ are similar for some millennial events, they diverge near Heinrich-1 (15.5-16.5 ka) and for part of the LGM (19-21 ka) (Fig. 4.4c), suggesting that both mechanisms contribute to salinity variations at these sites.

A plausible tropical mechanism for changing Atlantic-Pacific vapor transport calls on the relative roles of atmospheric moisture content and tropospheric wind speed (Hostetler and Mix, 1999). Cooling of the tropical and subtropical oceans

would reduce moisture content of the lower atmosphere. Reduced evaporation and export of freshwater would over time decrease Atlantic salinity, thereby reducing North Atlantic Deep Water (NADW) formation (Zaucker et al., 1994; Rahmstorf, 1995). A diminished supply of Atlantic moisture to the EPWP region would result in less rainfall and higher Pacific salinities, with potential to support more rapid ventilation of intermediate and/or deep waters of the North Pacific (Zheng et al., 2000). Tropical cooling (relative to mid-to-high latitudes) would also reduce trade wind intensities and cyclogenesis, which both play a role in westward vapor transport (Benway and Mix, 2004), and such effects offer the potential to amplify effects of atmospheric moisture. Following reduction of Atlantic meridional overturning circulation, buildup of oceanic heat in the tropical and subtropical Atlantic would increase atmospheric moisture and net westward vapor transport, eventually leading to increased Atlantic salinities and a return to the "NADW-on" mode. This set of connections based on varying cross-isthmus vapor transport could conceivably form an Atlantic-Pacific Salt Oscillator, analogous to a salt oscillator previously envisioned within the North Atlantic (Broecker et al., 1990).

Methods

Stable Isotopes

Isotope measurements were made at 2-3 cm intervals in ME0005A-43JC and 4-cm intervals in ODP 1242. Sediment samples were cleaned and sieved with deionized water and calgon, and coarse fractions were dried at 40°C. Specimens of *G. ruber* (*N. dutertrei*) were picked from the 250-355 μm (355-425 μm) size fraction. 15 (10) specimens of *G. ruber* (*N. dutertrei*) were used for each stable isotope measurement. In preparation for stable isotope analysis, samples were sonicated in deionized water and 95% ethanol. Samples were dried at 40°C for 12-24 hours, and analyzed at Oregon State University on a Finnigan-MAT 252 stable isotope ratio mass spectrometer equipped with a Kiel III carbonate device. Samples were reacted at 70°C in phosphoric acid, and all data are reported relative to the Pee Dee Belemnite (PDB)

standard via our internal standard, which is regularly calibrated against NBS-19 and NBS-20.

Mg/Ca

Mg/Ca ratios were measured on *G. ruber* (~10-20 specimens) collected from the same samples as those measured for stable isotopes using a flow-through technique (Haley and Klinkhammer, 2002; Benway et al., 2003) that combines ion chromatography and inductively coupled plasma mass spectrometry (ICP-MS) in a series of cleaning and dissolution reactions monitored continuously with time-resolved analysis (TRA). Daily analysis includes measurement of internal standards (covering the mass range of interest) to monitor instrument drift, as well as a suite of standards (Ca, Mg, Sr, Al, Mn) covering a reasonable concentration range for biogenic calcite. Two existing standards, NIST-1c argillaceous limestone and a homogeneous marble called the "Wiley standard," serve as additional monitors of intra- and inter-run consistency. Standardization is carefully checked by analysis of overlapping sections of core and replication between days, with minor adjustments (within the errors of daily calibration) to minimize daily offsets. Calcification temperature was calculated from Mg/Ca using SST = ln (Mg/Ca/0.38)/0.09 (Anand et al., 2003). Samples from ME0005A-43JC were cracked and sonicated in deionized water and 95% ethanol to remove clays. The homogenized samples were then split between stable isotope and Mg/Ca analysis. Samples from ODP Site 1242 were analyzed according to recent developments in the flow-through technique (Klinkhammer et al., 2004). A correction was applied to older Mg/Ca data to account for a systematic offset of 0.3 mmol/mol related to recent advances in the flow-through methodology. To calculate $\delta^{18}O_{sw}$, we used a paleotemperature equation (Thunell et al., 1999) specifically for *G. ruber*, which is the same as the *O. universa* high light equation from Bemis et al. (1998).

Sealevel Correction

We applied an ice volume correction based on coral (Clark and Mix, 2002) (0-21 ka) and benthic foraminiferal isotope (Waelbroeck et al., 2002) (21-30 ka) sealevel

reconstructions to our $\delta^{18}O_{sw}$ records using Gaussian interpolation. To demonstrate the potential uncertainty associated with the ice volume calculation, we show a range of corrected $\delta^{18}O_{sw}$ (Fig. 4.3d) estimates based on a $\delta^{18}O_{sw}$-sealevel scaling range of 0.0075-0.0100 ‰ m^{-1} decrease in relative sea level (RSL).

Age Model

Age models for ME0005A-43JC and ODP 1242 are based on a combination of $\delta^{18}O$ stratigraphy (Grootes and Stuiver, 1997; Shackleton et al., 2000) and six accelerator mass spectrometry (AMS) ^{14}C dates (*N. dutertrei*) from ME0005A-43JC. The Calib (version 5.0.1) program (Stuiver and Reimer, 1993) was used to convert ^{14}C ages to calendar ages, assuming a reservoir age of 558 years, the regional average for the west coast of Central America (Stuiver and Reimer, 1993). To apply the radiocarbon dates from 43JC to Site 1242, 1242 data were first expressed on 43JC pseudodepths, based on variations in stable isotope, Mg/Ca, and sediment density data. All age model data are listed in Appendix 3.

Error Analysis

Analytical precision of $\delta^{18}O_c$ measurements is ± 0.06 ‰, and that of flow-through Mg/Ca measurements is ± 0.10 mmol/mol, which translates to ± 0.3°C for the temperature range considered here. In addition, the error associated with the Mg/Ca-temperature calibration equation (Anand et al., 2003) is ± 0.5°C. The compounded (analytical + calibration) temperature error is ± 0.6°C. The slope error in the paleotemperature equation (Bemis et al., 1998) used to calculate $\delta^{18}O_{sw}$ yields an additional error of ± 0.07 ‰. Assuming a 1σ normal distribution in the Mg/Ca and $\delta^{18}O_c$ measurements, the compounded $\delta^{18}O_{sw}$ error is ± 0.3 ‰. Standard error of paleosalinity estimates based on the modern $\delta^{18}O_w$-S relationship for the EPWP region (Benway and Mix, 2004) is ± 0.2 PSU. Deviations in the $\delta^{18}O_w$-S relationship through time would generate paleosalinity errors ranging from 0.1-2.0 PSU with the largest errors attributed to changes in mean $\delta^{18}O_{precipitation}$ (Benway and Mix, 2004).

5. EASTERN TROPICAL PACIFIC TEMPERATURE AND $\delta^{18}O_{sw}$ DURING THE CLOSURE OF THE PANAMA ISTHMUS

Heather M. Benway

Schlanger Ocean Drilling Fellowship profile
Joint Oceanographic Institutions/U.S. Science Advisory Committee Newsletter
www.joiscience.org
Spring 2005

The westward transport of water vapor across the Panama Isthmus represents one of the most significant Atlantic freshwater export pathways. This process affects the salt balance between the Atlantic and Pacific Oceans, posing implications for deep ocean circulation and global climate variability. Eastern Pacific warm pool (EPWP) salinity is very sensitive to changes in rainfall, the dominant freshwater source to this region. A modern regional moisture budget (Benway and Mix, 2004) indicates that at least 50% of EPWP rainfall is of Caribbean origin, making this region a potential recorder of changes in cross-isthmus transport. A number of paleoclimate studies have focused on the Neogene closure of the Panama Isthmus and subsequent changes in global ocean circulation and northern hemisphere climate (Haug and Tiedemann, 1998). Planktonic oxygen isotope records from the Caribbean and eastern tropical Pacific show that a $\delta^{18}O_{calcite}$ gradient between the Caribbean and the Pacific developed between 4.6 and 4.2 Ma (Haug et al., 2001), and the Pacific thermocline shoaled ~4.2 Ma (Cannariato and Ravelo, 1997).

The primary goal of my Schlanger fellowship was to reconstruct changes in surface ocean temperature and salinity ($\delta^{18}O_{sw}$) in specific time windows immediately preceding and following the closure of the Panama Isthmus to determine the eastern Pacific response to the closure of this major ocean gateway. I sampled sediment cores from two sites in the EPWP region (Fig. 5.1) that were drilled on ODP Leg 202, focusing on two Pliocene time slices spanning the final closure of the Panama Isthmus (3.5-3.7 Ma, 4.7-4.9 Ma) and two Pleistocene time slices (0-30 ka; ~1.4-1.6 Ma) spanning the mid-Pleistocene transition from 41-ky to 100-ky cycles. Combined stable isotope analysis and Mg/Ca measurements (Benway et al., 2003) of three species of upper mixed layer-dwelling planktonic foraminifera (*G. ruber, G. obliquus, G. extremus*) yield a record of surface ocean $\delta^{18}O_{sw}$ changes. Mg/Ca is converted to temperature using the calibration of Anand et al. (2003), and $\delta^{18}O_{sw}$ is calculated using the high light *O. universa* culture equation from Bemis et al. (1998). I have applied a published ice volume correction (Waelbroeck et al., 2002) to the late Pleistocene interval (0-30 ka). Ice volume corrections for the ~1.4-1.6-Ma interval were

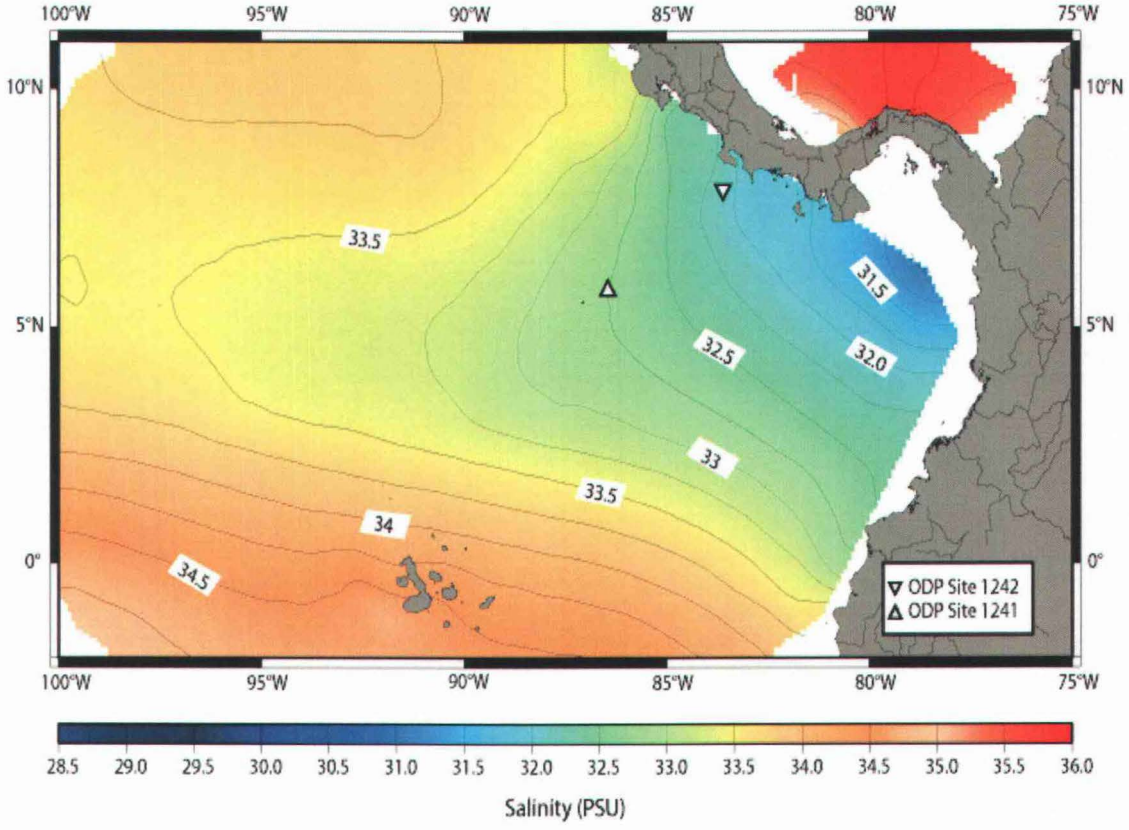

Figure 5.1. Salinity map (World Ocean Atlas, 1998) indicating site locations for this study.

approximated based on the benthic isotope records from ODP Sites 849 (Mix et al., 1995) and 1242. Pliocene intervals do not contain an ice volume correction, as benthic $\delta^{18}O_{calcite}$ is comparable to late Holocene benthic $\delta^{18}O_{calcite}$, suggesting a negligible ice volume contribution. The age model for Site 1242 is based on radiocarbon dates and benthic isotope stratigraphy. Pliocene age intervals from 1241 are based on the orbitally tuned age model of Tiedemann et al. (submitted).

A comparison of the two Pliocene time slices indicates only minor changes in mean surface ocean $\delta^{18}O_{calcite}$, Mg/Ca temperature, and $\delta^{18}O_{sw}$ in the EPWP (Fig. 5.2) in response to the final closure of the Panama Isthmus ~4.6 Ma, suggesting that the initial establishment of the Caribbean-Pacific isotopic gradient between 4.7 and 4.2 Ma (Haug et al., 2001) was mostly due to changes in the Caribbean. Recent temperature and $\delta^{18}O_{sw}$ reconstructions (Steph et al., submitted; Groeneveld et al., submitted) confirm this result, revealing Caribbean surface temperature and salinity increases soon after the isthmus closure and a delayed salinity response (decrease) in the eastern tropical Pacific. Generally, Pleistocene $\delta^{18}O_{calcite}$, Mg/Ca temperature, and $\delta^{18}O_{sw}$ show much higher amplitude variability, particularly in the 0-30 ka interval, relative to the Pliocene. Mean temperature is ~3°C higher and mean $\delta^{18}O_{sw}$ is comparable for the early Pleistocene relative to the Pliocene intervals (Fig. 5.2). There is a significant decrease in mean $\delta^{18}O_{sw}$ and Mg/Ca temperature associated with the mid-Pleistocene transition.

Although eastern Pacific thermocline changes occur ~4.2 Ma (Cannariato and Ravelo, 1997), the negligible Pacific surface ocean response immediately following the isthmus closure suggests that there was still some exchange of surface waters with the Caribbean. The transition from Pliocene to Pleistocene intervals introduces higher amplitude variability in these proxy records, which may suggest an increasingly important role for cross-isthmus vapor transport in colder, less stable ice age climates. However, higher resolution Pliocene proxy records are necessary to make a more robust comparison across these intervals.

Figure 5.2. $\delta^{18}O_{sw}$ (top), Mg/Ca temperature (middle), and $\delta^{18}O_{calcite}$ (bottom) records for from ODP Leg 202 Sites 1241 (*G. ruber*, *G. obliquus*, *G. extremus*) and 1242 (*G. ruber*) comparing Pliocene and Pleistocene time windows. Precise ages in the interval of 1.4-1.6 Ma (Site 1242) are not yet available, so the data interval spanning this age range is approximate. No ice volume correction was applied to Pliocene intervals. Ice volume corrections for the early Pleistocene interval are approximated from benthic isotope records. See Chapter 4 for information on ice volume corrections in the late Pleistocene interval. The benthic isotope record from ODP Site 849 (Mix et al., 1995) is shown on the bottom of the figure for temporal context, with significant climate events and transitions indicated (NHG = northern hemisphere glaciation). Data are available in Appendices 5, 6 (late Pleistocene), and 7 (Pliocene and early Pleistocene).

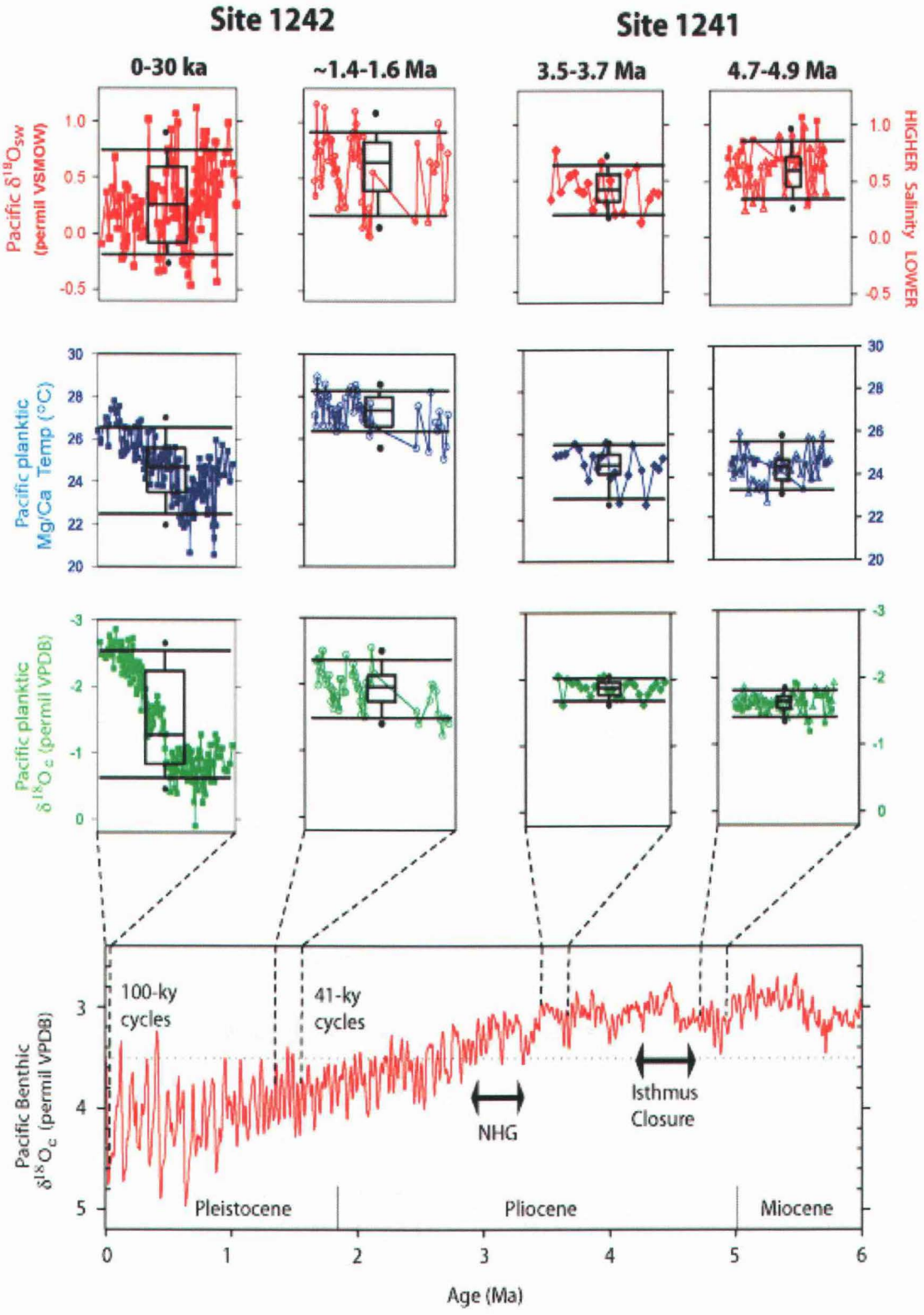
Site 1242
Site 1241
0-30 ka
~1.4-1.6 Ma
3.5-3.7 Ma
4.7-4.9 Ma
Pacific δ18Osw (permil VSMOW)
HIGHER Salinity LOWER
Pacific planktic Mg/Ca Temp (°C)
Pacific planktic δ18Oc (permil VPDB)
Pacific Benthic δ18Oc (permil VPDB)
100-ky cycles
41-ky cycles
NHG
Isthmus Closure
Pleistocene
Pliocene
Miocene
Age (Ma)

6. CONCLUSIONS

The findings in this dissertation are of great importance to a wide scientific audience, as they address fundamental research questions in paleoclimatology, climate dynamics, and oceanography. There have been countless debates in the paleoclimate community regarding the mechanisms behind millennial-scale climate variability. This work addresses mechanisms of tropical climate change and provides a new conceptual model about how variations in vapor transport serve as a globally important climate feedback.

Improved understanding of past climate variability requires accurate interpretations of paleorecords, which in part depend on and are constrained by a robust characterization of modern climate variability. The application of stable isotope tracers ($\delta^{18}O$) to rainwater and seawater samples to fingerprint present-day atmospheric moisture and ocean water mass sources was a critical component of this study. These measurements are becoming increasingly important as more general circulation models incorporate isotopic fractionation cycles to better characterize the dynamics of the hydrologic cycle. Isotope and salt balance calculations were estimated to assess the relative roles of atmospheric and oceanic processes in modulating the regional $\delta^{18}O_{sw}$-S relationship. A simple moisture budget and an understanding of the modern seasonality and dominant meteorological processes of the EPWP region became the foundation of the interpretation of the EPWP paleosalinity records.

The flow-through technique described in Chapter 3 has become a powerful tool to characterize heterogeneity in foraminiferal calcite, which represents an important opportunity to build on our current understanding of the complex calcification mechanisms in foraminifera. This new analytical approach employs a highly controlled acid gradient that effectively separates contaminant, clay, and calcite phases. Highly resolved dissolution profiles based on varying acid strength address two of the greatest challenges of measuring Mg/Ca: clay contamination and partial dissolution. The unique opportunity to extract only the primary calcite signal, which

most closely reflects calcification temperature, is a great step forward in Mg/Ca paleothermometry, as single point batch measurements are biased by other calcite phases that do not reflect environmental conditions. A series of multi-core top depth transects (Klinkhammer et al., 2004) confirms the capacity of flow-through to yield accurate temperatures, despite partial dissolution of deep samples. Automation of the flow-through system and development of a custom data analysis software package have improved method consistency and data reproducibility (Klinkhammer et al., 2004). Further advances in the method also eliminate the need for costly, labor-intensive pretreatment of samples that results in significant calcite loss and a subsequently biased Mg/Ca measurement.

Water vapor transport across the Panama Isthmus is a dominant feature of tropical meteorology. Model sensitivity studies indicate a potential role for vapor transport in modulating deep ocean circulation and climate variability, but paleoceanographic data that directly address this question have been lacking. Until now, this climatically important region of the eastern Pacific remains largely untouched by the paleoceanographic community. This work employs a host of analytical tools, including a new method for Mg/Ca paleothermometry, to 1) Identify moisture sources for the Eastern Pacific warm pool (EPWP) region, and 2) Reconstruct temperature and salinity changes in the EPWP during the late Pleistocene, as well as earlier Pliocene intervals associated with the closure of the Panama Isthmus. Late Pleistocene paleosalinity records document the importance of cross-isthmus vapor transport, particularly on millennial scales, in an ice age climate with highly variable deep ocean circulation. These records demonstrate a role for the tropics in global ocean circulation and climate changes, closing the debate on whether cross-isthmus vapor transport is an active climate feedback. Pliocene reconstructions show a delayed surface ocean response in the Pacific (relative to the Caribbean) to the closure of the isthmus, suggesting a more gradual development of the inter-basin salinity gradient that helps sustain deep water formation in the North Atlantic.

Bibliography

Anand, P., Elderfield, H., and Conte, M. H. (2003) Calibration of Mg/Ca thermometry in planktonic foraminifera from a sediment trap time series. *Paleoceanography* **18,** 10.1029/2002PA000846.

Arthur, M. A., Srivastava, S. P., Kaminski, M., Jarrard, R., and Osler, J. (1989) Seismic stratigraphy and history of deep circulation and sediment drift development in Baffin Bay and the Labrador Sea. *Proceedings of the Ocean Drilling Program Scientific Results* **105**, Ocean Drilling Program, College Station, TX, 957-988.

Bard, E. (2002) Abrupt climate change over millennial time scales: climate shock. *Physics Today* **55,** 32-38.

Bassinot, F. C., Levi, C., Ghelen, M., Labeyrie, L., Melieres, F., and Elderfield, H. (2001) Improving Mg/Ca paleothermometer: Correction of dissolution effects on Mg/Ca ratio of foraminifera shells. Poster presentation, International Conference on Paleoceanography (sponsored by the Municipal Government of Hokkaido, The City of Sapporo, Hokkaido University, Ocean Research Institute (University of Tokyo), Japan Marine Science and Technology Center, Ship and Ocean Foundation, and IMAGES); Sapporo, Japan, September 16-22.

Baumgartner, A. and Reichel, E. (1975) The world water balance. Elsevier, New York, 179 pp.

Bé, A. W. H. and Lott, L. (1964) Shell growth and structure of planktonic Foraminifera. *Science* **145**(3634), 823-824.

Bé, A. W. H., Morse, J. W., and Harrison, S. M. (1975) Progressive dissolution and ultrastructural breakdown in planktonic foraminifera. *In* Dissolution of deep-sea carbonates, Sliter, W. V., Bé, A. W. H., and Berger, W. H. (eds.) Cushman Foundation for Foraminiferal Research, Special Publication No. 13, pp.27-55.

Bé, A. W. H. (1980) Gametogenic calcification in a spinose planktonic foraminifer, *Globigerinoides sacculifer* (Brady). *Marine Micropaleontology* **5**, 283-310.

Bemis, B. E., Spero, H. J., Bijma, J., and Lea, D. W. (1998) Reevaluation of the oxygen isotopic composition of planktonic foraminifera: Experimental results and revised paleotemperature equations. *Paleoceanography* **13,** 150-160.

Bender, M. L., Lorens, R. B., and Williams, D. F. (1975) Sodium, magnesium and strontium in the tests of planktonic foraminifera. *Micropaleontology* **21**(4), 448-459.

Benway, H. M., Haley, B. A., Klinkhammer, G. P., and Mix, A. C. (2003) Adaptation of a flow-through leaching procedure for Mg/Ca paleothermometry. *Geochemistry Geophysics Geosystems* **4**(2), 10.1029/2002GC000312.

Benway, H. M. and Mix, A. C. (2004) Oxygen isotopes, upper-ocean salinity, and precipitation sources in the eastern tropical Pacific. *Earth and Planetary Science Letters* **224,** 493-507.

Berger, W. H. (1970) Planktonic foraminifera: Selective solution and the lysocline. *Marine Geology* **8**, 111-138.

Bingham, F., Howden, S. D., and Koblinsky, C. J. (2002) Sea surface salinity measurements in the historical database. *Journal of Geophysical Research* **107**(C12), 10.1029/2000JC000767.

Broecker, W. S. and Peng, T. H. (1982) Tracers in the sea. Eldigio Press, Palisades, NY, 690 pp.

Broecker, W. S. (1989) The salinity contrast between the Atlantic and Pacific Ocean during glacial times. *Paleoceanography* **4**, 207-212.

Broecker, W., Bond, G., and Klas, M., Bonani, G., and Wölfli, W. (1990) A salt oscillator in the Glacial Atlantic? *Paleoceanography* **5**, 469-477.

Broecker, W. S. (1991) The great ocean conveyor. *Oceanography* **4,** 79-89.

Brown, S. J. and Elderfield, H. (1996) Variations of Mg/Ca and Sr/Ca ratios of planktonic foraminifera caused by post-depositional dissolution: Evidence of shallow Mg-dependent dissolution. *Paleoceanography* **11**(5), 543-551.

Chelton, D. B., Freilich, M. H., and Esbensen, S. K. (2000) Satellite observations of the wind jets off the Pacific Coast of Central America. Part II: Relationships and dynamical considerations. *Monthly Weather Review* **128,** 2,019-2,043.

Clark, P. U. and Mix, A. C. (2002) Ice sheets and sea level of the Last Glacial Maximum. *Quaternary Science Reviews* **21,** 1-7.

Craig, H., Gordon, L. I., and Horibe, Y. (1963) Isotopic exchange effects in the evaporation of water. *Journal of Geophysical Research* **68**, 5,079-5,087.

Craig, H. and Gordon, L. I. (1965) Isotopic oceanography: Deuterium and oxygen 18 variations in the ocean and the marine atmosphere. *In*: Tongiorgi, E. (Ed.), Stable Isotopes in Oceanographic Studies and Paleotemperatures, Spoleto, pp. 9-130.

Curry, W. B., Thunell, R. C., and Honjo, S. (1983) Seasonal changes in the isotopic composition of planktonic foraminifera collected in Panama Basin sediment traps. *Earth and Planetary Science Letters* **64**, 33-43.

Dansgaard, W. (1964) Stable isotopes in precipitation. *Tellus* **16**, 436-468.

Davis, K. J., Dove, P. M., and Yoreo, J. J. D. (2000) The role of Mg^{2+} as an impurity in calcite growth. *Science* **290**, 1,134-1,137.

Dekens, P. S., Lea, D. W., Pak, D. K., and Spero, H. J. (2002) Core top calibration of Mg/Ca in tropical foraminifera: Refining paleotemperature estimation. *Geochemistry Geophysics Geosystems* **3**(4), 10.1029/2001GC000200.

Delaney, M. L., Bé, A. W. H., and Boyle, E. A. (1985) Li, Sr, Mg, and Na in foraminiferal calcite shells from laboratory culture, sediment traps, and sediment cores. *Geochimica et Cosmochimica Acta* **49**, 1,327-1,341.

Driscoll, N. W. and Haug, G. H. (1998) A short circuit in thermohaline circulation: A cause for northern hemisphere glaciation? *Science* **282**, 436-438.

Elderfield, H., Bertram, C. J., and Erez, J. (1996) A biomineralization model for the incorporation of trace elements into foraminiferal calcium carbonate. *Earth and Planetary Science Letters* **142**, 409-423.

Emiliani, C. (1955) Pleistocene temperatures. *Journal of Geology* **63**, 538-578.

Erez, J. and Honjo, S. (1981) Comparison of isotopic composition of planktonic foraminifera in plankton tows, sediment traps and sediments. *Palaeogeography, Palaeoclimateology, Palaeoecology* **33**, 129-156.

Fairbanks, R. G., Sverdlove, M., Free R., Wiebe, P. H., and Bé, A. W. H. (1982) Vertical distribution and isotopic fractionation of living planktonic foraminifera from the Panama Basin. *Nature* **298**, 841-844.

Falkner, K. K., Klinkhammer, G. P., Ungerer, C. A., and Christie, D. M. (1995) Inductively coupled plasma mass spectrometry in geochemistry. *Annual Reviews of Earth and Planetary Sciences* **23**, 409-449.

Faul, K. L., Ravelo, A. C., and Delaney, M. L. (2000) Reconstructions of upwelling, productivity, and photic zone depth in the eastern equatorial Pacific Ocean using planktonic foraminiferal stable isotopes and abundances. *Journal of Foraminiferal Research* **30**(2), 110-125.

Feldberg, M. J. and Mix, A. C. (2003) Planktonic foraminifera, sea surface

temperatures, and mechanisms of oceanic change in the Peru and south equatorial currents, 0-150 ky BP. *Paleoceanography* **18**, doi:10.1029/2001PA000740.

Ganopolski, A. and Rahmstorf, S. (2001) Rapid changes of glacial climate simulated in a coupled climate model. *Nature* **409,** 153-158.

Groeneveld, J., Steph, S., Tiedemann, R., Nürnberg, D., Garbe-Schoenberg, D., and Sturm, A. (Submitted) Pliocene mixed-layer oceanography for Site 1241 using combined Mg/Ca and $\delta^{18}O$ analyses of *Globigerinoides sacculifer*. *Proceedings of the Ocean Drilling Program, Scientific Results* **202**, Ocean Drilling Program, College Station, TX.

Grootes, P. M. and Stuiver, M. (1997) Oxygen 18/16 variability in Greenland snow and ice with 10^3 to 10^5-year time resolution. *Journal of Geophysical Research* **102,** 26,455-26,470.

Haley, B. A. and Klinkhammer, G. P. (2002) Development of a flow-through system for cleaning and dissolving foraminiferal tests. *Chemical Geology* **185**, 51-69.

Hastings, D. W., Russell, A. D., and Emerson, S. R. (1998) Foraminiferal magnesium in *Globeriginoides sacculifer* as a paleotemperature proxy. *Paleoceanography* **13**(2), 161-169.

Haug, G. H. and Tiedemann, R. (1998) Effect of the formation of the Isthmus of Panama on Atlantic Ocean thermohaline circulation. *Nature* **393**, 673-676.

Haug, G. H., Hughen, K. A., Sigman, D. M., Peterson, L. C., and Röhl, U. (2001) Southward migration of the Intertropical Convergence Zone through the Holocene. *Science* **293,** 1,304-1,308.

Haug, G. H., Tiedemann, R., Zahn, R., and Ravelo, A. C. (2001) Role of Panama uplift on oceanic freshwater balance. *Geology* **29**, 207-210.

Hecht, A. D., Eslinger, E. V., and Garmon, L. B. (1975) Experimental studies on the dissolution of planktonic foraminifera. *In* Dissolution of deep-sea carbonates, Sliter, W. V., Bé, A. W. H., and Berger, W. H. (eds.) Cushman Foundation for Foraminiferal Research, Special Publication No. 13, pp 56-69.

Hostetler, S. W. and Mix, A. C. (1999) Reassessment of ice-age cooling of the tropical ocean and atmosphere. *Nature* **399**, 673-676.

Hovan, S. A. (1991) Late Cenozoic atmospheric circulation intensity and climatic history recorded by Eolian deposition in the eastern equatorial Pacific Ocean, Leg 138.

Proceedings of the Ocean Drilling Program Scientific Results **138**, Ocean Drilling Program, College Station, TX, 615-625.

Jha, P. and Elderfield, H. (2000) Variation of Mg/Ca and Sr/Ca in planktonic and benthic foraminifera from single test chemistry. *Eos Trans. AGU* **81** (48), Fall Meet. Suppl., Abstract OS11C-13.

Joussaume, S., Sadourny, R., and Vignal, C. (1986) Origin of precipitating water in a numerical simulation of the July climate. *Ocean-Air Interactions* **1**, 43-56.

Joyce, R. and Arkin, P. A. (1997) Improved estimates of tropical and subtropical precipitation using the GOES Precipitation Index. *Journal of Atmospheric and Oceanographic Technology* **10**, 997-1,011.

Kaneps, A. G. (1979) Gulf Stream: Velocity fluctuations during the late Cenozoic. *Science* **204**, 297-301.

Katz, A. (1973) The interaction of magnesium with calcite during crystal growth at 25-90°C and one atmosphere. *Geochimica et Cosmochimica Acta* **37**, 1,563-1,586.

Keir, R. S. (1984) Recent increase in Pacific $CaCO_3$ dissolution: A mechanism for generating old ^{14}C ages. *Marine Geology* **59**, 227-250.

Kessler, W. S. (2002) Mean three-dimensional circulation in the northeast tropical Pacific. *Journal of Physical Oceanography* **32,** 2,457-2,471.

Klinkhammer, G. P., Haley, B. A., Mix, A. C., Benway, H. M., and Cheseby, M. (2004) Evaluation of automated flow-through time-resolved analysis of foraminifera for Mg/Ca paleothermometry. *Paleoceanography* **19**, 10.1029/2004PA001050.

Koutavas, A., Lynch-Stieglitz, J., Marchitto, T. M., Jr., and Sachs, J. P. (2002) El Niño-like pattern in ice age tropical Pacific sea surface temperature. *Science* **297**, 226-230.

Lachniet, M. S. and Patterson, W. P. (2002) Stable isotope values of Costa Rican surface waters. *Journal of Hydrology* 260, 135-150.

Lea, D. W., Mashiotta, T. A., and Spero, H. J. (1999) Controls on magnesium and strontium uptake in planktonic foraminifera determined by live culturing. *Geochimica et Cosmochimica Acta* **63**(16), 2,369-2,379.

Lea, D. W., Pak, D. K., and Spero, H. J. (2000) Climate impact of late Quaternary equatorial Pacific sea surface temperature variations. *Science* **289**, 1,719-1,724.

Lea, D. W., Pak, D. K., Peterson, L. C., and Hughen, K. A. (2003) Synchroneity of tropical high latitude Atlantic temperatures over the last glacial termination. *Science* **301,** 1,361-1,364.

Lohmann, G. P. (1995) A model for variation in the chemistry of planktonic foraminifera due to secondary calcification and selective dissolution. *Paleoceanography* **10**, 445-457.

Magaña, V., Amador, J. A., and Medina, S. (1999) The Midsummer Drought over Mexico and Central America. *Journal of Climate* **12**, 1,577-1,588.

Maier-Reimer, E., Mikolajewicz, U., and Crowley, T. J. (1990) Ocean general circulation model sensitivity experiment with an open American Isthmus. *Paleoceanography* **5**, 349-366.

Manabe, S. and Stouffer, R. J. (1988) Two stable equilibria of a coupled ocean-atmosphere model. *Journal of Climate* **1**, 841-866.

Mapes, B. E., Warner, T. T., Xu, M., and Negri, A. J. (2003) Diurnal patterns of rainfall in northwestern South America. Part I: Observations and context. *Monthly Weather Review* **131**, 799-812.

Martínez, I., Keigwin, L., Barrows, T. T., Yokoyama, Y., and Southon, J. (2003) La Niña-like conditions in the eastern equatorial Pacific and a stronger Choco jet in the northern Andes during the last glaciation. *Paleoceanography* **18**, 10.1029/2002PA000877.

McCorkle, D. C., Martin, P. A., Lea, D. W., and Klinkhammer, G. P. (1995) Evidence of a dissolution effect on benthic foraminiferal shell chemistry: $\delta^{13}C$, Cd/Ca, Ba/Ca, and Sr/Ca results from the Ontong Java Plateau. *Paleoceanography* **10**, 699-714.

McManus, J. F., Francois, Gherardi, J. –M., Keigwin, L. D., and Brown-Leger, S. (2004) Collapse and rapid resumption of Atlantic meridional circulation linked to deglacial climate changes. *Nature* **428,** 834-837.

Merlivat, L. and Jouzel, J. (1979) Global climatic interpretation of the deuterium-oxygen 18 relationship for precipitation. *Journal of Geophysical Research* **84**, 5,029-5,033.

Mikolajewicz, U. and Crowley, T. J. (1997) Response of a coupled ocean/energy balance model to restricted flow through the central American Isthmus. *Paleoceanography* **12**, 429-441.

Mix, A. C., Pisias, N. G., Rugh, W., Wilson, J., Morey, A., and Hagelberg, T. K. (1995) Benthic foraminifer stable isotope record from Site 849 (0-5 Ma); local and global climate changes. *In* Pisias, N. G., Mayer, L. A., and Janecek, T. R. (Eds.), *Proceedings of the Ocean Drilling Program, Scientific Results* **138**, 371-412, Ocean Drilling Program, College Station, TX.

Mucci, A. and Morse, J. W. (1990) Chemistry of low-temperature abiotic calcites: Experimental studies on coprecipitation, stability, and fractionation. *Reviews in Aquatic Sciences* **3**, 217-254.

National Oceanographic Data Center's Ocean Climate Laboratory (1998) World Ocean Atlas 1998. **Vols. 2, 5**, *NOAA Atlas* (**NESDIS 28, 31**), U.S. Gov. Printing Office, Washington, D.C.

Nürnberg, D., Bijma, J., and Hemleben, C. (1996) Assessing the reliability of magnesium in foraminiferal calcite as a proxy for water mass temperatures. *Geochimica et Cosmochimica Acta* **60**(5), 803-814.

Nürnberg, D., Müller, A., and Schneider, R. R. (2000) Paleo-sea surface temperature calculations in the equatorial east Atlantic from Mg/Ca ratios in planktic foraminifera: A comparison to sea surface temperature estimates from $U^{k'}_{37}$, oxygen isotopes, and foraminiferal transfer function. *Paleoceanography* **15**(1), 124-134.

Oort, A. H. (1983) Global atmospheric circulation statistics, 1958-1973. NOAA Prof. Paper 14, 180 pp.

Peixoto, J. P. and Oort, A. H. (1992) Physics of Climate. American Institute of Physics, New York, 500 pp.

Peterson, L. C., Haug, G. H., Hughen, K. A., and Röhl, U. (2000) Rapid changes in the hydrologic cycle of the tropical Atlantic during the last glacial. *Science* **290,** 1,947-1,951.

Poveda, G. and Mesa, O. J. (2000) On the existence of Lloró (the rainiest locality on Earth): Enhanced ocean-land-atmosphere interaction by a low-level jet. *Geophysical Research Letters* **27**, 1,675-1,678.

Rahmstorf, S. (1995) Bifurcations of the Atlantic thermohaline circulation in response to changes in the hydrological cycle. *Nature* **378**, 145-149.

Rahmstorf, S. (1996) On the freshwater forcing and transport of the Atlantic thermohaline circulation. *Climate Dynamics* **12,** 799-811.

Rodríguez-Rubio, E., Schneider, W., and Abarca del Río, R. (2003) On the seasonal circulation within the Panama Bight derived from satellite observations of wind, altimetry and sea surface temperature. *Geophysical Research Letters* **30**(7), 10.1029/2002GL016794.

Rohling, E. J. and Bigg, G. R. (1998) Paleosalinity and $\delta^{18}O$: A critical assessment. *Journal of Geophysical Research* **103**, 1,307-1,318.

Rosenthal, Y. and Boyle, E. A. (1993) Factors controlling the fluoride content of planktonic foraminifera: An evaluation of its paleoceanographic applicability. *Geochimica et Cosmochimica Acta* **57**, 335-346.

Rosenthal Y., Lohmann, G. P., Lohmann, K. C., and Sherrell, R. M. (2000) Incorporation and preservation of Mg in *Globigerinoides sacculifer*: Implications for reconstructing the temperature and $^{18}O/^{16}O$ of seawater. *Paleoceanography* **15**(1), 135-145.

Rushdi, A. I., Chen-Tung, A. C., and Suess, E. (1998) The solubility of calcite in seawater solution of different magnesium concentrations at 25°C and 1 atm total pressure: A laboratory re-examination. *La Mer* **36**, 9-22.

Russell, A. D., Emerson, S., Nelson, B. K., Erez, J., and Lea, D. W. (1994) Uranium in foraminiferal calcite as a recorder of seawater uranium concentrations. *Geochimica et Cosmochimica Acta* **58**, 671-681.

Schmidt, G. A. (1999) Forward modeling of carbonate proxy data from planktonic foraminifera using oxygen isotope tracers in a global ocean model. *Paleoceanography* **14**, 482-497.

Schmidt, G. A., Bigg, G. R., and Rohling, E. J. (1999) Global Seawater Oxygen-18 Database. http://www.giss.nasa.gov/data/o18data/.

Schmidt, M. W., Spero, H. J., and Lea, D. W. (2004) Links between salinity variation in the Caribbean and North Atlantic thermohaline circulation. *Nature* **428,** 160-163.

Schmittner, A., Appenzeller, C., and Stocker, T. F. (2000) Enhanced Atlantic freshwater export during El Niño. *Geophysical Research Letters* **27**, 1,163-1,166.

Schmittner, A. and Clement, A. C. (2002) Sensitivity of the thermohaline circulation to tropical and high latitude freshwater forcing during the last glacial-interglacial cycle. *Paleoceanography* **17**, 10.1029/2000PA000591.

Schmittner, A., Meissner, K. J., Eby, M., and Weaver, A. J. (2002) Forcing of the deep ocean circulation in simulations of the Last Glacial Maximum.

Paleoceanography **17**, 10.1029/2001PA000633.

Shackleton, N. J., Backman, J., Zimmerman, H., Kent, D. V., Hall, M. A., Roberts, D. G., Schnitker, D., Baldauf, J. G., Desprairies, A., Homrighausen, R., Huddlestun, P., Keene, J. B., Kaltenback, A. J., Krumsiek, K. A. O., Morton, A. C., Murray, J. W., and Westberg-Smith, J. (1984) Oxygen isotope calibration of the onset of ice-rafting and history of glaciation in the North Atlantic region. *Nature* **307**, 620-623.

Shackleton, N. J., Hall, M., and Pate, D. (1995) Pliocene stable isotope stratigraphy of Site 846. *Proceedings of the Ocean Drilling Program Scientific Results* **138**, Ocean Drilling Program, College Station, TX, 337-357.

Shackleton, N. J., Hall, M. A., and Vincent, E. (2000) Phase relationships between millennial scale events 64,000 to 24,000 years ago. *Paleoceanography* **15,** 565-569.

Spero, H. J., Mielke, K. M., Kalve, E. M., Lea, D. W., and Pak, D. K. (2003) Multispecies approach to reconstructing eastern equatorial Pacific thermocline hydrography during the past 360 ky. *Paleoceanography* **18**, 10.1029/2002PA000814.

Steph, S., Tiedemann, R., Groeneveld, J., Sturm, A., and Nürnberg, D. (Submitted) Pliocene changes in tropical east Pacific upper ocean stratification: Response to tropical gateways? *Proceedings of the Ocean Drilling Program, Scientific Results* **202**, Ocean Drilling Program, College Station, TX.

Stott, L., Poulsen, C., Lund, S., and Thunell, R. (2002) Super ENSO and global climate oscillations at millennial time scales. *Science* **297**, 222-226.

Stuiver, M. and Reimer, P.J. (1993) Extended ^{14}C database and revised CALIB radiocarbon calibration program. *Radiocarbon* **35,** 215-230.

Thunell, R. C., Curry, W. B., and Honjo, S. (1983) Seasonal variation in the flux of planktonic foraminifera: time series sediment trap results from the Panama Basin. *Earth and Planetary Science Letters* **64**, 44-55.

Thunell, R. C. and Reynolds, L. A. (1984) Sedimentation of planktonic foraminifera: Seasonal changes in species flux in the Panama Basin. *Micropaleontology* **30**(3), 243-262.

Thunell, R., Tappa, E., Pride, C., and Kincaid, E. (1999) Sea-surface temperature anomalies associated with the 1997-1998 El Niño recorded in the oxygen isotope composition of planktonic foraminifera. *Geology* **27**, 843-846.

Tiedemann, R. and Franz, S. O. (1997) Deep-water circulation, chemistry, and terrigenous sediment supply in the equatorial Atlantic during the Pliocene, 3.3-2.6 Ma

and 5-4.5 Ma. *Proceedings of the Ocean Drilling Program Scientific Results* **154**, 299-318.

Tiedemann, R., Sturm, A., Steph, S., Stoner, J., and Lund, S. (Submitted) Astronomically calibrated time scales from 6-2.5 Ma and benthic isotope stratigraphies of sites 1236, 1237, 1239 and 1241. *Proceedings of the Ocean Drilling Program, Scientific Results* **202**, Ocean Drilling Program, College Station, TX.

Toggweiler, J. R., Dixon, K., and Broecker, W. S. (1991) The Peru upwelling and the ventilation of the South Pacific thermocline. *Journal of Geophysical Research* **96**, 20,467-20,497.

Tsuchiya, M. and Talley, L. D. (1998) A Pacific hydrographic section at 88°W: Water-property distribution. *Journal of Geophysical Research* **103**, 12,899-12,918.

Waelbroeck, C., Labeyrie, L., Michel, E., Duplessy, J. C., McManus, J. F., Lambeck, K., Balbon, E., and Labracherie, M. (2002) Sea-level and deep water temperature changes derived from benthic foraminifera isotopic records. *Quaternary Science Reviews* **21**, 295-305.

Weyl, P. K. (1968) The role of the oceans in climatic change: A theory of the ice ages. *Meterological Monographs* **8**, 37-62.

Wyrtki, K. (1966) Oceanography of the eastern equatorial Pacific Ocean. *Oceanography and Marine Biology Annual Review* **4**, 33-68.

Zaucker, F. and Broecker, W. S. (1992) The influence of atmospheric moisture transport on the fresh water balance of the Atlantic drainage basin: General circulation model simulations and observations. *Journal of Geophysical Research* **97**, 2,765-2,773.

Zaucker, F., Stocker, T. F., and Broecker, W. S. (1994) Atmospheric freshwater fluxes and their effect on the global thermohaline circulation. *Journal of Geophysical Research* **99**, 12,443-12,457.

Zhang, R. and Delworth, T. L. (2005) Simulated tropical response to a substantial weakening of the Atlantic thermohaline circulation. *Journal of Climate* **18**, 1853-1860.

Zheng, Y., van Geen, A., Anderson, R. F., Gardner, J. V., and Dean, W. E. (2000) Intensification of the northeast Pacific oxygen minimum zone during the Bølling-Allerød warm period. *Paleoceanography* **15**, 528-536.

APPENDIX 1: Listing of seawater $\delta^{18}O$ and salinity data from Chapter 2.

Cruise	Longitude (deg)	Latitude (deg)	Sample Depth (m)	Potential Temp. (°C)	Salinity (PSU)	$\delta^{18}O$ (‰ VSMOW)	Date of Collection	Average $\delta^{18}O$ (‰ VSMOW)	St Dev (‰ VSMOW)	Std Error (‰ VSMOW)
NEMO-3 2000	-81.995	-0.513	2	22.5	34.894	0.300	6/1/2000	0.317	0.03	0.02
NEMO-3 2000	-81.995	-0.513	2	22.5	34.894	0.300	6/1/2000			
NEMO-3 2000	-81.995	-0.513	2	22.5	34.894	0.350	6/1/2000			
NEMO-3 2000	-82.787	-1.853	2	22.5	35.051	0.390	5/30/2000	0.360	0.04	0.03
NEMO-3 2000	-82.787	-1.853	2	22.5	35.051	0.330	5/30/2000			
NEMO-3 2000	-86.705	4.615	2	28.4	32.079	-0.390	5/25/2000	-0.397	0.06	0.03
NEMO-3 2000	-86.705	4.615	2	28.4	32.079	-0.460	5/25/2000			
NEMO-3 2000	-86.705	4.615	2	28.4	32.079	-0.340	5/25/2000			
NEMO-3 2000	-83.610	7.860	2	28.5	32.147	-0.380	6/6/2000			
NEMO-3 2000	-86.460	0.022	2	23.4	35.005	0.280	5/28/2000	0.287	0.06	0.03
NEMO-3 2000	-86.460	0.022	2	23.4	35.005	0.230	5/28/2000			
NEMO-3 2000	-86.460	0.022	2	23.4	35.005	0.350	5/28/2000			
NEMO-3 2000	-95.281	15.656	2	28.8	34.524	0.200	5/18/2000	0.230	0.04	0.03
NEMO-3 2000	-95.281	15.656	2	28.8	34.524	0.260	5/18/2000			
NEMO-3 2000	-84.110	7.320	2	27.1	33.043	-0.110	6/5/2000	-0.110	0.02	0.01
NEMO-3 2000	-84.110	7.320	2	27.1	33.043	-0.090	6/5/2000			
NEMO-3 2000	-84.110	7.320	2	27.1	33.043	-0.110	6/5/2000			
NEMO-3 2000	-84.110	7.320	2	27.1	33.043	-0.130	6/5/2000			
NEMO-3 2000	-86.450	5.850	2	28.8	32.701	-0.170	5/24/2000	-0.140	0.05	0.03
NEMO-3 2000	-86.450	5.850	2	28.8	32.701	-0.080	5/24/2000			
NEMO-3 2000	-86.450	5.850	2	28.8	32.701	-0.170	5/24/2000			
NEMO-3 2000	-86.490	3.210	2	28.1	31.841	-0.260	5/26/2000	-0.280	0.03	0.02
NEMO-3 2000	-86.490	3.210	2	28.1	31.841	-0.270	5/26/2000			
NEMO-3 2000	-86.490	3.210	2	28.1	31.841	-0.310	5/26/2000			
NEMO-3 2000	-85.010	4.120	2	26.8	32.459	-0.150	6/4/2000	-0.165	0.02	0.02
NEMO-3 2000	-85.010	4.120	2	26.8	32.459	-0.180	6/4/2000			
NEMO-3 2000	-95.281	15.656	50	22.6	34.667	0.180	5/18/2000	0.170	0.02	0.01
NEMO-3 2000	-95.281	15.656	50	22.6	34.667	0.180	5/18/2000			
NEMO-3 2000	-95.281	15.656	50	22.6	34.667	0.150	5/18/2000			
NEMO-3 2000	-81.995	-0.513	100	16.5	35.107	0.410	6/1/2000	0.363	0.05	0.03
NEMO-3 2000	-81.995	-0.513	100	16.5	35.107	0.370	6/1/2000			
NEMO-3 2000	-81.995	-0.513	100	16.5	35.107	0.310	6/1/2000			

Cruise	Longitude (deg)	Latitude (deg)	Sample Depth (m)	Potential Temp. (°C)	Salinity (PSU)	$\delta^{18}O$ (‰ VSMOW)	Date of Collection	Average $\delta^{18}O$ (‰ VSMOW)	St Dev (‰ VSMOW)	Std Error (‰ VSMOW)
NEMO-3 2000	-82.787	-1.853	100	15.5	35.104	0.310	5/30/2000	0.293	0.04	0.02
NEMO-3 2000	-82.787	-1.853	100	15.5	35.104	0.250	5/30/2000			
NEMO-3 2000	-82.787	-1.853	100	15.5	35.104	0.320	5/30/2000			
NEMO-3 2000	-84.110	7.320	100	16.1	34.816	0.240	6/5/2000	0.268	0.02	0.01
NEMO-3 2000	-84.110	7.320	100	16.1	34.816	0.280	6/5/2000			
NEMO-3 2000	-84.110	7.320	100	16.1	34.816	0.280	6/5/2000			
NEMO-3 2000	-84.110	7.320	100	16.1	34.816	0.270	6/5/2000			
NEMO-3 2000	-86.450	5.850	100	14.4	34.877	0.240	5/24/2000	0.223	0.04	0.02
NEMO-3 2000	-86.450	5.850	100	14.4	34.877	0.180	5/24/2000			
NEMO-3 2000	-86.450	5.850	100	14.4	34.877	0.250	5/24/2000			
NEMO-3 2000	-86.705	4.615	100	14.4	34.942	0.280	5/25/2000	0.343	0.07	0.04
NEMO-3 2000	-86.705	4.615	100	14.4	34.942	0.410	5/25/2000			
NEMO-3 2000	-86.705	4.615	100	14.4	34.942	0.340	5/25/2000			
NEMO-3 2000	-83.610	7.860	100	16.6	34.833	0.230	6/6/2000	0.238	0.03	0.01
NEMO-3 2000	-83.610	7.860	100	16.6	34.833	0.270	6/6/2000			
NEMO-3 2000	-83.610	7.860	100	16.6	34.833	0.210	6/6/2000			
NEMO-3 2000	-83.610	7.860	100	16.6	34.833	0.240	6/6/2000			
NEMO-3 2000	-86.490	3.210	100	14.7	34.968	0.380	5/26/2000	0.350	0.04	0.03
NEMO-3 2000	-86.490	3.210	100	14.7	34.968	0.320	5/26/2000			
NEMO-3 2000	-86.460	0.022	100	16.7	35.098	0.530	5/28/2000	0.475	0.08	0.06
NEMO-3 2000	-86.460	0.022	100	16.7	35.098	0.420	5/28/2000			
NEMO-3 2000	-85.010	4.120	100	14.9	34.987	0.270	6/4/2000	0.267	0.02	0.01
NEMO-3 2000	-85.010	4.120	100	14.9	34.987	0.250	6/4/2000			
NEMO-3 2000	-85.010	4.120	100	14.9	34.987	0.280	6/4/2000			
NEMO-3 2000	-95.281	15.656	100	15.6	34.821	0.320	5/18/2000	0.285	0.05	0.03
NEMO-3 2000	-95.281	15.656	100	15.6	34.821	0.250	5/18/2000			
NEMO-3 2000	-95.281	15.656	150	13.7	34.856	0.290	5/18/2000			
NEMO-3 2000	-95.292	15.710	200	13.0	34.825	0.240	5/19/2000	0.217	0.04	0.02
NEMO-3 2000	-95.292	15.710	200	13.0	34.825	0.170	5/19/2000			
NEMO-3 2000	-95.292	15.710	200	13.0	34.825	0.240	5/19/2000			
NEMO-3 2000	-95.292	15.710	250	12.4	34.799	0.220	5/19/2000			
NEMO-3 2000	-95.280	15.581	300	12.1	34.775	0.270	5/19/2000	0.240	0.04	0.03
NEMO-3 2000	-95.280	15.581	300	12.1	34.775	0.210	5/19/2000			
NEMO-3 2000	-95.280	15.581	400	10.5	34.713	0.160	5/19/2000	0.120	0.04	0.02

Cruise	Longitude (deg)	Latitude (deg)	Sample Depth (m)	Potential Temp. (°C)	Salinity (PSU)	$\delta^{18}O$ (°/oo VSMOW)	Date of Collection	Average $\delta^{18}O$ (°/oo VSMOW)	St Dev (°/oo VSMOW)	Std Error (°/oo VSMOW)
NEMO-3 2000	-95.280	15.581	400	10.5	34.713	0.090	5/19/2000			
NEMO-3 2000	-95.280	15.581	400	10.5	34.713	0.110	5/19/2000			
EPIC 2001	-95.230	10.370	0-5	***	33.603	-0.014	9/18/2001			
EPIC 2001	-94.850	9.820	0-5	***	***	-0.070	9/19/2001	-0.035	0.05	0.04
EPIC 2001	-94.850	9.820	0-5	***	***	0.000	9/19/2001			
EPIC 2001	-94.850	10.030	0-5	***	33.635	0.003	9/23/2001			
EPIC 2001	-95.070	10.520	0-5	***	33.664	-0.006	9/24/2001			
EPIC 2001	-94.850	9.650	0-5	***	33.387	-0.038	9/25/2001			
EPIC 2001	-94.290	9.930	0-5	***	33.593	-0.029	9/27/2001			
EPIC 2001	-95.160	10.430	0-5	***	33.282	-0.168	9/28/2001			
EPIC 2001	-94.810	10.070	0-5	***	33.646	-0.016	9/29/2001			
EPIC 2001	-94.850	10.560	0-5	***	33.483	-0.065	9/30/2001			
EPIC 2001	-95.400	10.070	0-5	***	33.417	-0.075	10/1/2001			
EPIC 2001	-95.400	9.490	0-5	***	33.416	-0.058	10/2/2001			
EPIC 2001	-95.390	8.990	0-5	***	32.985	-0.137	10/2/2001			
EPIC 2001	-94.770	9.490	0-5	***	33.675	0.023	9/15/2001			
EPIC 2001	-95.000	10.980	0-5	***	33.678	0.045	9/16/2001			
EPIC 2001	-94.850	10.070	0-5	***	33.621	0.052	9/17/2001			
EPIC 2001	-95.030	10.560	0-5	***	33.619	0.033	9/20/2001			
EPIC 2001	-94.930	10.070	0-5	***	33.492	0.023	9/21/2001			
EPIC 2001	-94.480	9.780	0-5	***	33.735	0.064	9/22/2001			
EPIC 2001	-95.460	10.130	0-5	***	33.517	0.010	9/26/2001			
EPIC 2001	-95.390	8.500	0-5	***	33.547	0.012	10/2/2001			
EPIC 2001	-95.390	7.290	0-5	***	33.450	0.038	10/3/2001			
EPIC 2001	-95.390	6.830	0-5	***	33.548	0.023	10/3/2001	0.021	0.003	0.002
EPIC 2001	-95.390	6.830	0-5	***	33.548	0.018	10/3/2001			
EPIC 2001	-95.390	6.280	0-5	***	33.378	0.025	10/3/2001			
EPIC 2001	-95.390	5.780	0-5	***	33.325	0.018	10/3/2001			
EPIC 2001	-95.390	8.800	0-5	***	33.557	0.006	10/9/2001			
EPIC 2001	-95.390	5.240	0-5	***	33.447	0.154	10/4/2001			
EPIC 2001	-95.390	4.820	0-5	***	33.477	0.131	10/4/2001			
EPIC 2001	-95.390	4.220	0-5	***	33.646	0.230	10/4/2001			
EPIC 2001	-95.390	3.720	0-5	***	33.602	0.168	10/4/2001			
EPIC 2001	-95.390	3.170	0-5	***	33.528	0.150	10/4/2001			

Cruise	Longitude (deg)	Latitude (deg)	Sample Depth (m)	Potential Temp. (°C)	Salinity (PSU)	$\delta^{18}O$ (°/oo VSMOW)	Date of Collection	Average $\delta^{18}O$ (°/oo VSMOW)	St Dev (°/oo VSMOW)	Std Error (°/oo VSMOW)
EPIC 2001	-95.390	2.810	0-5	***	***	0.486	10/4/2001			
EPIC 2001	-95.390	2.650	0-5	***	33.445	0.136	10/4/2001			
EPIC 2001	-95.390	2.150	0-5	***	33.691	0.175	10/5/2001	0.167	0.01	0.01
EPIC 2001	-95.390	2.150	0-5	***	33.691	0.160	10/5/2001			
EPIC 2001	-95.390	1.700	0-5	***	33.832	0.173	10/5/2001			
EPIC 2001	-95.390	1.120	0-5	***	33.991	0.132	10/5/2001			
EPIC 2001	-95.390	0.580	0-5	***	34.236	0.239	10/5/2001			
EPIC 2001	-95.390	0.060	0-5	***	34.314	0.265	10/5/2001			
EPIC 2001	-95.390	-0.540	0-5	***	34.856	0.343	10/5/2001			
EPIC 2001	-95.420	-0.970	0-5	***	34.893	0.362	10/6/2001			
EPIC 2001	-95.390	0.070	0-5	***	34.382	0.277	10/6/2001		**Overall**	**Overall**
EPIC 2001	-95.390	3.860	0-5	***	33.679	0.187	10/7/2001		0.04	0.02
EPIC 2001	-95.390	5.540	0-5	***	33.434	0.107	10/8/2001			

APPENDIX 2: Listing of rainwater $\delta^{18}O$ data from Chapter 2.										
Cruise	Longitude (deg.) (<0 = deg. W)	Latitude (deg.) (<0 = deg. S)	Date of Collection	Time of Collection	Total Rainfall (in.) in rain gauge	Air Temp. (°C) (time of collection)	True Wind Speed (m/s) (time of collection)	True Wind Direction (deg) (time of collection)	$\delta^{18}O$ (°/oo VSMOW)	Comments
EPIC 2001	between -94.77 and -95.00	between 9.49 and 10.98	9/16/2001	0030 UT	0.49	27.5	3.9	328	-3.267	
EPIC 2001	-94.87	10.85	9/16/2001	1517 UT	0.90	26.1	0.4	249	-5.036	
EPIC 2001	-94.85	10.72	9/16/2001	2311 UT	0.60	27.5	2.3	268	-4.462	
EPIC 2001	-94.83	10.79	9/18/2001	2237 UT	0.40	26.8	4.4	205	-7.126	
EPIC 2001	-95.01	10.07	9/21/2001	1050 UT	0.51	26.1	1.8	61	-3.845	
EPIC 2001	-94.27	10.07	9/22/2001	1400 UT	0.21	26.6	6.8	188	-4.920	Hurricane Juliette
EPIC 2001	-94.85	9.77	9/23/2001	1227 UT	0.61	26.0	3.6	282	-4.612	Hurricane Juliette
EPIC 2001	-94.22	10.04	9/23/2001	2141 UT	***	25.8	9.2	203	-10.430	Hurricane Juliette
EPIC 2001	-95.10	10.49	9/24/2001	1116 UT	0.20	25.8	5.4	206	-2.638	Hurricane Juliette
EPIC 2001	between -94.85 and -95.07	between 9.65 and 10.52	9/24/2001	1412 UT	1.43	24.5	10.8	132	-4.406	Hurricane Juliette
EPIC 2001	-94.21	9.96	9/27/2001	1113 UT	0.24	26.1	4.4	253	-6.114	
EPIC 2001	-94.11	10.02	9/27/2001	1409 UT	0.51	25.0	10.5	335	-6.878	
EPIC 2001	-95.39	6.27	10/3/2001	1819 UT	0.65	25.2	4.6	215	-3.684	
EPIC 2001	-95.39	5.87	10/3/2001	2133 UT	0.27	25.2	7.2	199	-1.608	
EPIC 2001	-95.39	7.15	10/8/2001	2210 UT	0.50	24.2	2.4	195	-4.256	
EPIC 2001	-95.02	10.02	10/9/2001	2308 UT	0.28	26.0	4.0	220	-3.776	
Costa Rica (land-based)	-84.38	9.75	10/10/2001	0000 CR local time	***	***	***	***	-6.529	
Costa Rica (land-based)	-84.38	9.75	10/12/2001	1430 CR local time	***	***	***	***	-7.062	
Costa Rica (land-based)	-84.38	9.75	10/12/2001	1430 CR local time	***	***	***	***	-7.078	
Costa Rica (land-based)	-84.38	9.75	10/13/2001	1500 CR local time	***	***	***	***	-4.456	
Costa Rica (land-based)	-84.38	9.75	10/19/2001	1410 CR local time	***	***	***	***	-3.825	
Costa Rica (land-based)	-84.38	9.75	10/20/2001	1500 CR local time	***	***	***	***	-7.926	
Costa Rica (land-based)	-84.38	9.75	10/20/2001	1500 CR local time	***	***	***	***	-7.874	
Costa Rica (land-based)	-84.38	9.75	10/24/2001	1600 CR local time	***	***	***	***	-6.945	
Costa Rica (land-based)	-84.38	9.75	10/26/2001	1400 CR local time	***	***	***	***	-9.504	
Costa Rica (land-based)	-84.38	9.75	11/1/2001	0830 CR local time	***	***	***	***	-13.754	Hurricane Michelle
Costa Rica (land-based)	-84.38	9.75	11/1/2001	0830 CR local time	***	***	***	***	-13.740	Hurricane Michelle
Costa Rica (land-based)	-84.17	10.52	11/21/2001	1430 CR local time	***	***	***	***	-13.645	Hurricane Olga
Costa Rica (land-based)	-84.17	10.52	11/22/2001	0715 CR local time	***	***	***	***	-3.259	Hurricane Olga

Cruise	Longitude (deg.) (<0 = deg. W)	Latitude (deg.) (<0 = deg. S)	Date of Collection	Time of Collection	Total Rainfall (in.) in rain gauge	Air Temp. (°C) (time of collection)	True Wind Speed (m/s) (time of collection)	True Wind Direction (deg) (time of collection)	$\delta^{18}O$ (°/oo VSMOW)	Comments
Costa Rica (land-based)	-84.17	10.52	11/22/2001	0000 CR local time	***	***	***	***	-2.343	Hurricane Olga
Costa Rica (land-based)	-84.17	10.52	11/23/2001	0400 CR local time	***	***	***	***	-2.317	Hurricane Olga
ODP Leg 202	-86.45	5.84	5/21/2002	0130 local time	***	***	***	***	-5.492	
ODP Leg 202	-86.45	5.84	5/21/2002	0130 local time	***	***	***	***	-5.517	
ODP Leg 202	-86.45	5.84	5/22/2002	0130 local time	***	***	***	***	-2.327	
ODP Leg 202	-86.45	5.84	5/22/2002	0130 local time	***	***	***	***	-2.325	
ODP Leg 202	-86.45	5.84	5/22/2002	0130 local time	***	***	***	***	-2.305	
ODP Leg 202	-86.45	5.84	5/24/2002	0400 local time	***	***	***	***	-2.438	
ODP Leg 202	-86.45	5.84	5/24/2002	0400 local time	***	***	***	***	-2.473	
ODP Leg 202	-86.45	5.84	5/24/2002	0400 local time	***	***	***	***	-2.458	
ODP Leg 202	-86.45	5.84	5/24/2002	1600 local time	***	***	***	***	-4.212	
ODP Leg 202	-86.45	5.84	5/24/2002	1600 local time	***	***	***	***	-4.182	
ODP Leg 202	-86.45	5.84	5/24/2002	1600 local time	***	***	***	***	-4.211	
ODP Leg 202	-86.45	5.84	5/25/2002	0230 local time	***	***	***	***	-7.158	
ODP Leg 202	-86.45	5.84	5/25/2002	0230 local time	***	***	***	***	-7.120	
ODP Leg 202	-86.45	5.84	5/25/2002	0230 local time	***	***	***	***	-7.165	
ODP Leg 202	-86.45	5.84	5/25/2002	1400 local time	***	***	***	***	-4.003	
ODP Leg 202	-86.45	5.84	5/25/2002	1400 local time	***	***	***	***	-4.110	
ODP Leg 202	-86.45	5.84	5/25/2002	1400 local time	***	***	***	***	-4.063	
ODP Leg 202	-86.45	5.84	5/25/2002	1400 local time	***	***	***	***	-4.120	
ODP Leg 202	-86.45	5.84	5/25/2002	1400 local time	***	***	***	***	-4.073	
ODP Leg 202	-86.45	5.84	5/25/2002	1400 local time	***	***	***	***	-3.987	
ODP Leg 202	-83.61	7.86	5/26/2002	0900 local time	***	***	***	***	-5.836	
ODP Leg 202	-83.61	7.86	5/26/2002	0900 local time	***	***	***	***	-5.902	
ODP Leg 202	-82.48	7.40	5/29/2002	0530 local time	***	***	***	***	-3.319	

APPENDIX 3: Listing of age model information from Chapter 4.

Calendar age models for ME0005A-43JC and ODP 1242

AMS ^{14}C and calendar ages for ME0005A-43JC are listed below. Radiocarbon ages were generated at NOSAMS. All AMS 14C dates are based on the planktic foraminifera *N. dutertrei*. The Calib rev. 5.0.1 program (Stuiver and Reimer, 1993) was used to convert ^{14}C dates into calendar age (yrs. BP) assuming a reservoir age of 558 yrs., which is based on a regional average (Stuiver and Reimer, 1993) for the west coast of Central America. Age models are based on calibrated radiocarbon ages listed below (0-22 ka) and $\delta^{18}O_C$ stratigraphy (>22 ka) (Grootes and Stuiver, 1997; Shackleton et al., 2000). ME0005A-43JC and 1242 depths were first correlated, and then the same age model was applied to both cores.

AMS ^{14}C dates for ME0005A-43JC.							
Core	**Depth (cm)**	**NOSAMS Accession #**	**$\Delta^{14}C$**	**^{14}C AMS age (yrs. BP)**	**Error (yr)**	**2σ range (yrs. BP)**	**Calendar Age (yrs. BP)**
ME0005A-43JC	13	OS-42066	-324.9	3,100	±35	2,500-2,851	2,676
ME0005A-43JC	26	OS-42050	-462.5	4,940	±35	4,860-5,249	5,055
ME0005A-43JC	91	OS-42051	-728.8	10,450	±60	11,140-11,641	11,391
ME0005A-43JC	131	OS-42052	-819.9	13,700	±80	15,158-15,955	15,557
ME0005A-43JC	186	OS-42053	-893.2	17,900	±95	20,154-20,856	20,505
ME0005A-43JC	208	OS-42054	-908.6	19,150	±110	21,793-22,452	22,123

Calendar Age Model Tie Points

ME0005A-43JC depth (cm)	Age (ky BP)	Method
13	2.676	radiocarbon
26	5.055	radiocarbon
91	11.391	radiocarbon
131	15.557	radiocarbon
186	20.505	radiocarbon
208	22.123	radiocarbon
228	23.303	*G. ruber* $\delta^{18}O$ strat. (GISP2)
238	24.000	*G. ruber* $\delta^{18}O$ strat. (GISP2)
281	28.941	*G. ruber* $\delta^{18}O$ strat. (GISP2)
286	29.140	Benthic $\delta^{18}O$ strat. (Shackleton)
421	38.970	Benthic $\delta^{18}O$ strat. (Shackleton)
516	45.530	Benthic $\delta^{18}O$ strat. (Shackleton)
696	57.810	Benthic $\delta^{18}O$ strat. (Shackleton)
736	62.740	Benthic $\delta^{18}O$ strat. (Shackleton)
956	83.180	Benthic $\delta^{18}O$ strat. (Shackleton)

APPENDIX 4: Listing of core top isotope and Mg/Ca data from Chapter

Complete data listing for coretops (Fig. 4.2).					
Core top Latitude (deg.) < 0 = S	**Core top Longitude (deg.) < 0 = W**	***N. dutertrei* $\delta^{18}O_C$ (permil VPDB)**	***G. ruber* $\delta^{18}O_C$ (permil VPDB)**	***G. ruber* Mg/Ca (mmol/mol)**	**Mg/Ca Temp. (°C)**
7.856	-83.608	-0.16	-2.87		
7.317	-84.113	0.69	-2.78	4.34	27.1
5.846	-86.449	0.16	-2.30	4.31	27.0
4.614	-86.704	0.29		4.18	26.6
3.212	-86.486	0.21	-2.89	4.23	26.8
0.022	-86.463	1.05			
-0.513	-81.995	0.45	-1.40	3.33	24.1
-1.853	-82.787	0.61			

APPENDIX 5: Listing of downcore isotope and Mg/Ca data for ODP 1242 from Chapter 4. Bold Mg/Ca values indicate standard error > 0.03 mmol/mol. $\delta^{18}O_{sw}$ values have not been corrected for ice volume changes.

ODP 1242							
Depth (mcd)	Age (ky BP)	*N. dutertrei* $\delta^{18}O_C$ (permil PDB)	*G. ruber* $\delta^{18}O_C$ (permil PDB)	*G. ruber* Mg/Ca (mmol/mol)	Mg/Ca Temp. (°C)	$\delta^{18}O_{SW}$ (permil VSMOW)	Paleosalinity (PSU)
0.01	0.766	0.02		**4.49**	27.44		
0.05	1.222	-0.16	-2.75	4.02	26.21	-0.124	33.50
0.09	1.677	0.15	-2.66	4.07	26.34	-0.007	33.97
0.13	2.133	0.23	-2.68	**4.75**	28.06	0.332	35.33
0.17	2.315	0.20	-2.34				
0.21	2.498	-0.08	-2.37	**4.55**	27.58	0.542	36.17
0.25	3.154	0.22	-2.42	4.46	27.37	0.448	35.75
0.29	3.373	0.24	-2.03	3.98	26.09	0.571	36.24
0.33	3.592	0.34	-2.56	4.09	26.39	0.104	34.38
0.37	3.865	0.16	-2.49	**4.52**	27.52	0.409	35.60
0.41	4.138	0.05	-2.65				34.15
0.45	5.148	0.17	-2.73	**4.31**	26.98	0.057	
0.49	5.635	0.18	-2.26	3.63	25.08	0.131	34.44
0.53	5.967	0.25	-2.66	**4.19**	26.66	0.060	34.16
0.57	6.279	0.38	-2.67	4.29	26.94	0.108	34.27
0.61	6.591	0.41	-2.57	4.37	27.14	0.250	34.56
0.65	6.903	0.54	-2.55	4.43	27.30	0.303	34.73
0.69	7.001	0.45	-2.62	4.08	26.37	0.040	33.64
0.73	7.684	0.22	-2.67	4.08	26.39	-0.006	33.34
0.77	7.976	0.28	-2.58	3.87	25.78	-0.043	33.11
0.81	8.171	0.22	-2.22	4.04	26.26	0.417	34.87
0.85	8.269	0.10	-2.26	4.15	26.55	0.437	34.95
0.89	8.366	0.65	-2.25	3.77	25.49	0.226	34.06
0.93	8.513	0.41		**3.66**	25.16		

Depth (mcd)	Age (ky BP)	*N. dutertrei* $\delta^{18}O_C$ (permil PDB)	*G. ruber* $\delta^{18}O_C$ (permil PDB)	*G. ruber* Mg/Ca (mmol/mol)	Mg/Ca Temp. (°C)	$\delta^{18}O_{SW}$ (permil VSMOW)	Paleosalinity (PSU)
0.97	8.659	0.33	-2.36	**3.68**	25.21	0.058	33.27
1.01	8.727	0.02	-2.29	3.65	25.15	0.115	33.50
1.05	8.854	0.63	-2.22	3.98	26.10	0.383	34.49
1.09	9.088	0.50	-2.77				
1.13	9.322	0.79	-2.36	4.05	26.30	0.285	33.82
1.17	9.508	0.63	-2.52	4.05	26.30	0.125	33.02
1.21	9.634	0.52	-2.28	4.37	27.15	0.542	34.65
1.25	9.781	0.60	-2.51	**4.51**	27.48	0.381	33.92
1.29	9.927	0.69	-2.27	**4.17**	26.62	0.442	34.09
1.33	10.122	0.50	-2.54	4.01	26.18	0.080	32.52
1.37	10.317	0.85	-2.14	3.92	25.93	0.428	33.79
1.41	10.610	0.35	-1.3	3.45	24.52	0.974	35.82
1.50	11.097	1.14	-1.25	**3.59**	24.97	1.118	36.19
1.54	11.370	0.72	-1.43	3.98	26.09	1.171	36.32
1.58	11.484	0.76	-1.58	3.70	25.30	0.857	35.03
1.62	11.599	0.49	-1.82	4.04	26.28	0.821	34.88
1.66	11.838	0.79	-1.70	4.10	26.44	0.974	35.42
1.70	12.088	0.83	-1.44	3.89	25.86	1.113	35.89
1.74	12.328	0.88	-1.60	4.13	26.50	1.087	35.71
1.78	12.954	1.00	-1.53	3.90	25.87	1.025	35.22
1.82	13.475	0.87	-1.74	4.15	26.57	0.961	34.76
1.86	13.819	0.82	-1.36	3.92	25.93	1.208	35.47
1.90	14.173	0.78	-1.57	3.66	25.16	0.837	33.71
1.94	14.518	0.97	-1.56	3.82	25.65	0.950	34.00
1.98	14.622	0.98	-1.29	3.70	25.29	1.145	34.74
2.02	14.726	0.84	-1.62	3.75	25.45	0.848	33.51
2.06	15.247	0.91	-1.46	3.49	24.65	0.841	33.32
2.10	15.404	0.88	-1.37	3.59	24.94	0.992	33.89
2.14	15.560	1.19	-0.83	3.76	25.47	1.642	36.41

Depth (mcd)	Age (ky BP)	*N. dutertrei* $\delta^{18}O_C$ (permil PDB)	*G. ruber* $\delta^{18}O_C$ (permil PDB)	*G. ruber* Mg/Ca (mmol/mol)	Mg/Ca Temp. (°C)	$\delta^{18}O_{SW}$ (permil VSMOW)	Paleosalinity (PSU)
2.18	15.740	1.45	-1.16	3.23	23.77	0.958	33.63
2.22	16.082	1.11	-0.88	3.95	26.02	1.707	36.51
2.26	16.244	1.21	-1.15	**3.84**	25.70	1.370	35.12
2.30	16.460	1.07	-0.41	3.46	24.56	1.872	37.05
2.34	16.640	1.03	-0.77	3.70	25.28	1.663	36.17
2.38	17.027	1.44	-0.68	3.48	24.61	1.613	35.85
2.42	17.423	1.33	-0.7	3.46	24.55	1.580	35.60
2.46	17.810	1.58	-0.46	3.81	25.61	2.041	37.40
2.50	18.035	1.18	-0.88	3.73	25.37	1.571	35.48
2.54	18.260	1.41	-0.39	3.76	25.46	2.080	37.52
2.58	18.350	1.54	-0.88	3.18	23.62	1.207	33.99
2.62	18.440	1.42	-0.98	3.43	24.45	1.280	34.28
2.66	18.593	1.25	-0.96	3.02	23.02	1.002	33.13
2.70	18.737	1.32	-0.67	3.21	23.72	1.437	34.83
2.74	18.890	1.57	-0.6	3.33	24.12	1.591	35.32
2.78	19.340	1.62	-1.04	3.49	24.63	1.257	33.71
2.82	19.475	1.22	-0.92	3.40	24.33	1.315	33.86
2.86	19.610	1.62	-0.88	3.32	24.09	1.305	33.78
2.90	20.060	1.31	-1.08	2.89	22.56	0.786	31.66
2.94	20.240	1.61	-0.78	3.28	23.95	1.375	34.06
2.98	20.510	1.49	-0.93	3.04	23.11	1.050	32.80
3.01	20.656	1.43	-0.76	3.33	24.13	1.433	34.37
3.05	20.839	1.60	-0.85	2.94	22.72	1.049	32.84
3.09	21.022	1.64	-0.73	3.63	25.07	1.659	35.20
3.13	21.242	1.67	-0.79	3.52	24.72	1.526	34.66
3.17	21.754	1.59	-0.25	3.27	23.92	1.899	36.16
3.21	21.864	1.50	-0.41	**3.54**	24.81	1.925	36.26
3.25	21.974	1.46	-0.84	3.11	23.34	1.188	33.31
3.29	22.297	1.48	-0.79	3.42	24.42	1.463	34.45

Depth (mcd)	Age (ky BP)	*N. dutertrei* $\delta^{18}O_C$ (permil PDB)	*G. ruber* $\delta^{18}O_C$ (permil PDB)	*G. ruber* Mg/Ca (mmol/mol)	Mg/Ca Temp. (°C)	$\delta^{18}O_{SW}$ (permil VSMOW)	Paleosalinity (PSU)
3.33	22.592	1.48	-0.8	3.31	24.04	1.374	34.14
3.37	22.887	1.41	-1.02	3.58	24.91	1.335	33.98
3.41	23.094	1.61	-0.98	3.64	25.12	1.419	34.32
3.45	23.300	1.26	-0.86	3.57	24.90	1.493	34.61
3.49	23.475	1.68	-0.78	3.79	25.55	1.709	35.52
3.53	23.650	1.68	-1.08	3.66	25.18	1.332	34.05
3.57	24.000	1.67	-0.56	3.33	24.13	1.633	35.29
3.61	24.115	1.56	-0.81	3.81	25.61	1.691	35.56
3.65	24.230	1.60	-0.87	3.63	25.08	1.521	34.88
3.69	24.345	1.53	-0.94	3.51	24.69	1.370	34.28
3.73	24.460	1.67	-0.82	3.37	24.25	1.398	34.39
3.77	24.574	1.48		3.75	25.43		
3.81	24.862	1.78	-0.56	3.45	24.51	1.712	35.65
3.85	25.149	2.01	-1.00	3.71	25.31	1.439	34.64
3.89	25.493	1.59	-1.13	3.92	25.93	1.438	34.75
3.93	25.723	1.51	-0.91	3.45	24.52	1.364	34.50
3.97	25.953	1.78	-0.94	3.42	24.42	1.313	34.29
4.01	26.642	1.69	-0.93	3.45	24.50	1.340	34.48
4.05	27.791	1.42	-1.08	3.59	24.96	1.286	34.42
4.09	28.653	1.53	-0.78	3.69	25.25	1.646	36.22
4.13	29.140	1.28	-0.94	3.52	24.74	1.380	35.16
4.17	29.227	1.29	-1.18	3.43	24.46	1.082	33.97
4.21	29.322	1.44	-1.07	3.85	25.72	1.454	35.46
4.25	29.409	1.48	-0.67	3.76	25.47	1.802	36.85
4.29	29.642	1.62	-0.75	3.54	24.80	1.582	36.05
4.33	29.926	1.80	-0.93	3.96	26.04	1.661	36.44
4.37	30.210	1.71	-0.72	3.74	25.41	1.740	36.84

APPENDIX 6: Listing of downcore isotope and Mg/Ca data for ME0005A-43JC from Chapter 4. Bold Mg/Ca values indicate standard error > 0.03 mmol/mol. $\delta^{18}O_{sw}$ values have not been corrected for ice volume changes.

ME0005A-43JC							
Depth (cm)	Age (ky BP)	*N. dutertrei* $\delta^{18}O_C$ (permil PDB)	*G. ruber* $\delta^{18}O_C$ (permil PDB)	*G. ruber* Mg/Ca (mmol/mol)	*G. ruber* Mg/Ca Temp. (°C)	$\delta^{18}O_{SW}$ (permil VSMOW)	Paleosalinity (PSU)
1	0.492	0.26		4.21	26.73		
3	0.857	0.02	-2.47	3.87	25.77	0.065	34.26
5	1.222	-0.18		**3.44**	24.48		
6	1.404	0.10		3.53	24.75		
8	1.768	0.20	-2.51	3.89	25.85	0.041	34.16
10	2.133	0.46		4.35	27.08		
11	2.315	0.18	-2.55	4.17	26.61	0.160	34.64
13	2.680	0.24	-2.76	3.69	25.24	-0.336	32.66
15	3.045	0.12	-2.46	4.73	28.01	0.541	36.12
16	3.227	0.07	-2.58	3.98	26.10	0.023	34.05
18	3.592	0.39	-2.68	4.83	28.25	0.371	35.44
20	3.956	0.25	-2.56	4.71	27.96	0.431	35.68
21	4.138	0.06	-2.86	3.57	24.89	-0.509	31.92
23	4.503	0.10		3.99	26.12		
25	4.868	0.63	-2.41	4.49	27.43	0.470	35.80
26	5.050	0.18	-2.39	3.97	26.07	0.207	34.75
28	5.245	0.45	-2.65	4.08	26.36	0.007	33.95
30	5.440	0.43	-2.60	4.02	26.20	0.024	34.02
31	5.538	0.22	-2.18	4.04	26.26	0.457	35.75
33	5.733	0.35	-2.29	4.34	27.07	0.515	35.98
35	5.928	0.66	-2.38	4.20	26.68	0.344	35.30
36	6.025	0.50	-2.52	4.06	26.32	0.129	34.44
38	6.220	0.17	-2.49	4.10	26.44	0.184	34.66
40	6.416	0.46	-2.53	4.21	26.74	0.207	34.59

Depth (cm)	Age (ky BP)	*N. dutertrei* $\delta^{18}O_C$ (permil PDB)	*G. ruber* $\delta^{18}O_C$ (permil PDB)	*G. ruber* Mg/Ca (mmol/mol)	*G. ruber* Mg/Ca Temp. (°C)	$\delta^{18}O_{sw}$ (permil VSMOW)	Paleosalinity (PSU)
41	6.513	0.37	-2.54	3.84	25.69	-0.022	33.55
43	6.708	0.43	-2.15	4.15	26.56	0.549	35.72
45	6.903	0.72	-2.46	4.01	26.18	0.160	34.16
46	7.001	0.64	-2.70	4.16	26.60	0.007	33.51
48	7.196	0.60	-2.26	4.18	26.65	0.458	35.31
50	7.391	0.54	-2.35	**3.70**	25.30	0.087	33.79
51	7.488	0.35	-2.04	4.81	28.21	1.003	37.41
53	7.684	0.24	-2.43	3.90	25.86	0.123	33.85
55	7.879	0.55	-2.61	3.90	25.86	-0.057	33.05
56	7.976	0.37	-2.73	4.19	26.68	-0.006	33.26
58	8.171	0.74	-2.10	4.16	26.59	0.605	35.62
60	8.366	0.76	-2.24	3.96	26.03	0.349	34.56
61	8.464	0.58	-2.26	4.06	26.31	0.387	34.67
63	8.659	0.27	-2.37	3.34	24.16	-0.171	32.36
65	8.854	0.73	-1.88	3.91	25.90	0.682	35.69
66	8.952	0.61	-1.96	4.38	27.16	0.864	36.38
68	9.147	0.63	-1.97	3.99	26.11	0.635	35.38
70	9.342	0.39	-2.20	4.19	26.67	0.522	34.77
71	9.439	0.78	-2.36	4.31	26.99	0.429	34.28
73	9.634	0.40	-2.00	3.87	25.80	0.541	34.64
75	9.829	0.64	-2.02	4.04	26.25	0.615	34.86
76	9.927	0.64	-1.63	4.27	26.88	1.136	36.86
78	10.122	0.52	-2.28	3.91	25.89	0.280	33.32
80	10.317	0.77	-2.10	3.93	25.96	0.474	33.98
81	10.415	0.58	-1.95	3.92	25.92	0.616	34.46
83	10.610	0.43	-2.16	4.13	26.50	0.527	34.03
85	10.805	0.81	-1.84	3.69	25.24	0.584	34.14
86	10.902	0.90	-1.96	4.60	27.71	0.979	35.68
88	11.097	1.33	-1.74	3.77	25.49	0.736	34.66

Depth (cm)	Age (ky BP)	*N. dutertrei* $\delta^{18}O_C$ (permil PDB)	*G. ruber* $\delta^{18}O_C$ (permil PDB)	*G. ruber* Mg/Ca (mmol/mol)	*G. ruber* Mg/Ca Temp. (°C)	$\delta^{18}O_{SW}$ (permil VSMOW)	Paleosalinity (PSU)
90	11.292	1.07	-1.24	4.04	26.27	1.399	37.28
91	11.390	0.60	-1.28	4.12	26.50	1.407	37.27
93	11.599	0.68	-1.69	4.06	26.32	0.959	35.44
95	11.807	0.59	-1.45	3.91	25.91	1.114	35.98
96	11.911	0.90	-1.29	3.69	25.27	1.140	36.08
98	12.120	0.92	-1.37	3.76	25.48	1.104	35.86
100	12.328	0.82	-1.51	4.17	26.61	1.200	36.16
101	12.433	1.08	-1.41	4.04	26.26	1.227	36.23
103	12.641	0.97	-1.44	3.85	25.74	1.088	35.59
106	12.954	1.15		3.91	25.90	0.932	34.85
108	13.162	0.95	-1.63				
111	13.475	0.83	-1.85	4.02	26.20	0.774	34.02
113	13.684	1.06	-1.66	3.83	25.66	0.852	34.17
116	13.996	0.89	-1.56	3.99	26.14	1.052	34.69
118	14.205	0.48	-1.61	3.95	26.01	0.975	34.26
121	14.518	0.48	-1.66	3.68	25.24	0.764	33.26
123	14.726	0.74	-1.37	3.90	25.88	1.187	34.87
126	15.039	0.58	-1.06	4.04	26.26	1.577	36.39
128	15.247	0.84	-1.28	3.82	25.65	1.230	34.92
131	15.560	1.46	-0.85	4.03	26.24	1.782	37.01
133	15.740	1.14	-0.77	3.16	23.53		
136	16.010	1.48	-0.78	3.96	26.04	1.811	37.00
138	16.190	1.53	-0.63	3.72	25.35	1.817	36.95
141	16.460	1.34	-0.74	3.41	24.40	1.509	35.60
143	16.640	1.28	-1.00	3.58	24.92	1.358	34.99
146	16.910	1.33	-0.93	3.78	25.51	1.550	35.64
148	17.090	1.42	-0.79	3.61	25.01	1.586	35.70
151	17.360	1.44	-0.90	3.55	24.84	1.441	35.04
153	17.540	1.49	-0.83	3.35	24.19	1.375	34.78

Depth (cm)	Age (ky BP)	*N. dutertrei* $\delta^{18}O_C$ (permil PDB)	*G. ruber* $\delta^{18}O_C$ (permil PDB)	*G. ruber* Mg/Ca (mmol/mol)	*G. ruber* Mg/Ca Temp. (°C)	$\delta^{18}O_{SW}$ (permil VSMOW)	Paleosalinity (PSU)
156	17.810	1.53	-0.72	3.39	24.32	1.512	35.29
158	17.990	1.45	-1.06	3.42	24.40	1.189	33.96
161	18.260	1.63	-0.85	3.29	23.97	1.310	34.44
163	18.440	1.56	-1.06				
166	18.710	1.47	-0.98	3.11	23.36	1.053	33.29
168	18.890	1.53	-0.71	3.13	23.44	1.339	34.32
171	19.160	1.45	-0.89	3.19	23.65	1.203	33.57
173	19.340	1.58	-0.96	3.07	23.20	1.039	32.84
176	19.610	1.44	-0.70	3.27	23.90	1.445	34.34
178	19.790	1.58	-0.87	3.32	24.09	1.315	33.78
181	20.060	1.34	-1.09	3.12	23.39	0.949	32.32
183	20.240	1.66	-0.58				
186	20.510	1.67	-1.05	3.29	23.99	1.114	33.06
188	20.604		-0.89	3.09	23.27	1.124	33.14
191	20.745	1.37	-0.95	3.37	24.24	1.266	33.70
193	20.839	1.63	-0.70				
196	20.981	1.54	-1.02	3.29	23.98	1.142	33.13
198	21.075	1.89	-0.88	3.22	23.75	1.234	33.50
201	21.216	1.55	-0.55	3.17	23.57	1.526	34.66
203	21.310	1.77	-0.26	3.23	23.79	1.862	36.01
206	21.796	1.54	-0.74	3.44	24.47	1.524	34.66
208	22.120	1.65		3.47	24.58		
211	22.297	1.62	-0.60	3.40	24.36	1.641	35.16
213	22.415	1.59	-0.57	3.47	24.57	1.715	35.46
216	22.592	1.43	-0.44	3.48	24.60	1.851	36.04
218	22.710	1.51	-0.91	3.60	24.98	1.460	34.48
221	22.887	1.67	-1.04	3.74	25.42	1.422	34.33
223	23.005	1.46	-1.01	3.48	24.61	1.283	33.77
226	23.182	1.51	-0.91	3.81	25.60	1.589	35.00

Depth (cm)	Age (ky BP)	*N. dutertrei* $\delta^{18}O_C$ (permil PDB)	*G. ruber* $\delta^{18}O_C$ (permil PDB)	*G. ruber* Mg/Ca (mmol/mol)	*G. ruber* Mg/Ca Temp. (°C)	$\delta^{18}O_{SW}$ (permil VSMOW)	Paleosalinity (PSU)
228	23.300	1.13	-1.27				
231	23.440	1.53	-0.51	3.73	25.38	1.943	36.41
233	23.533	2.06	-0.75	3.39	24.33	1.485	34.62
236	23.673		-0.64	3.57	24.89	1.711	35.56
238	23.767	1.48	-0.43	3.74	25.40	2.027	36.83
241	23.907	1.74	-0.62	3.76	25.48	1.854	36.18
243	24.000	1.66	-0.37	3.76	25.47	2.102	37.17
246	24.390	1.93	-0.87	3.46	24.55	1.410	34.44
248	24.650	1.89	-0.72	3.51	24.69	1.590	35.16
251	25.040	1.85	-0.69	3.37	24.26	1.530	34.96
256	25.690	1.87	-0.81				
261	26.340	1.74	-1.12				
266	26.990	1.71	-0.86	3.68	25.21	1.558	35.47
271	27.640	1.47		3.67	25.21		
276	28.290	1.58	-1.27	3.59	24.97	1.098	33.87

APPENDIX 7: Listing of isotope and Mg/Ca data from Chapter 5. Bold Mg/Ca values indicate standard error > 0.03 mmol/mol. $\delta^{18}O_{sw}$ values have not been corrected for ice volume changes.

Site	Depth (mcd)	Age (Ma)	Species	$\delta^{18}O_c$ (VPDB)	Mg/Ca (mmol/mol)	Mg/Ca Temp. (deg. C)	$\delta^{18}O_{sw}$ (permil VSMOW)	Paleosalinity (PSU)
ODP 1241	92.12	3.546	*G. ruber*	-2.04	3.59	24.97	0.328	35.31
ODP 1241	92.32	3.552	*G. ruber*	-1.61	3.61	25.01	0.766	37.06
ODP 1241	92.52	3.558	*G. ruber*	-1.99	3.63	25.07	0.399	35.60
ODP 1241	92.72	3.565	*G. ruber*	-1.94				
ODP 1241	92.92	3.571	*G. ruber*	-1.95	3.79	25.54	0.537	36.15
ODP 1241	93.12	3.577	*G. ruber*	-1.87	3.70	25.30	0.567	36.27
ODP 1241	93.32	3.584	*G. ruber*	-1.87	3.46	24.55	0.410	35.64
ODP 1241	93.52	3.590	*G. ruber*	-1.74	3.24	23.83	0.390	35.56
ODP 1241	93.72	3.596	*G. ruber*	-1.89	3.60	24.97	0.478	35.91
ODP 1241	93.92	3.602	*G. ruber*	-2.01	3.41	24.39	0.237	34.95
ODP 1241	94.12	3.608	*G. ruber*	-2.04	3.59	24.97	0.328	35.31
ODP 1241	94.32	3.614	*G. ruber*	-1.83	3.80	25.58	0.665	36.66
ODP 1241	94.52	3.620	*G. ruber*	-1.85	3.28	23.94	0.303	35.21
ODP 1241	94.72	3.627	*G. ruber*	-1.71	**3.35**	24.20	0.498	35.99
ODP 1241	94.92	3.633	*G. ruber*	-1.71	2.95	22.76	0.198	34.79
ODP 1241	95.12	3.639	*G. ruber*	-1.92				
ODP 1241	95.32	3.645	*G. ruber*	-1.97	3.32	24.08	0.213	34.85
ODP 1241	95.52	3.651	*G. ruber*	-1.91	3.76	25.47	0.562	36.25
ODP 1241	95.72	3.657	*G. ruber*	-1.77				
ODP 1241	95.92	3.663	*G. ruber*	-1.61	**3.39**	24.31	0.620	36.48

Site	Depth (mcd)	Age (Ma)	Species	$\delta^{18}O_c$ (VPDB)	Mg/Ca (mmol/mol)	Mg/Ca Temp. (deg. C)	$\delta^{18}O_{sw}$ (permil VSMOW)	Paleosalinity (PSU)
ODP 1241	96.12	3.669	*G. ruber*	-1.77	**2.93**	22.69	0.123	34.49
ODP 1241	96.32	3.675	*G. ruber*	-1.86				
ODP 1241	96.52	3.681	*G. ruber*	-1.94	3.45	24.52	0.334	35.34
ODP 1241	96.72	3.687	*G. ruber*	-1.84	3.40	24.35	0.399	35.60
ODP 1241	96.92	3.693	*G. ruber*	-1.96	3.56	24.85	0.383	35.53
ODP 1241	134.08	4.737	*G. obliquus*	-1.65	3.36	24.23	0.564	36.26
ODP 1241	134.28	4.742	*G. obliquus*	-1.68	3.24	23.81	0.446	35.78
ODP 1241	134.48	4.746	*G. obliquus*	-1.57				
ODP 1241	134.68	4.751	*G. obliquus*	-1.75	3.52	24.72	0.566	36.26
ODP 1241	134.88	4.755	*G. obliquus*	-1.85	3.92	25.92	0.716	36.86
ODP 1241	135.09	4.760	*G. obliquus*	-1.69	3.28	23.96	0.467	35.87
ODP 1241	135.29	4.765	*G. obliquus*		3.31	24.06		
ODP 1241	135.49	4.769	*G. obliquus*	-1.67	3.50	24.68	0.638	36.55
ODP 1241	135.69	4.774	*G. obliquus*	-1.74	3.03	23.08	0.234	34.94
ODP 1241	135.89	4.780	*G. obliquus*	-1.65	3.21	23.72	0.457	35.83
ODP 1241	136.09	4.785	*G. obliquus*	-1.54	3.20	23.66	0.555	36.22
ODP 1241	136.29	4.791	*G. obliquus*	-1.71	3.09	23.28	0.306	35.22
ODP 1241	136.49	4.796	*G. obliquus*	-1.59	3.16	23.54	0.480	35.92
ODP 1241	136.70	4.802	*G. obliquus*	-1.64	3.07	23.22	0.363	35.45
ODP 1241	136.90	4.808	*G. obliquus*	-1.45	3.17	23.56	0.624	36.50
ODP 1241	137.10	4.813	*G. obliquus*	-1.63	2.93	22.68	0.261	35.04
ODP 1241	137.30	4.819	*G. obliquus*	-1.59	3.43	24.44	0.668	36.67
ODP 1241	137.50	4.824	*G. obliquus*	-1.68	3.41	24.39	0.567	36.27
ODP 1241	137.70	4.830	*G. obliquus*	-1.53	3.32	24.07	0.650	36.60
ODP 1241	137.90	4.835	*G. obliquus*	-1.69	3.55	24.82	0.647	36.59

Site	Depth (mcd)	Age (Ma)	Species	$\delta^{18}O_c$ (VPDB)	Mg/Ca (mmol/mol)	Mg/Ca Temp. (deg. C)	$\delta^{18}O_{sw}$ (permil VSMOW)	Paleosalinity (PSU)
ODP 1241	138.11	4.841	*G. obliquus*	-1.40				
ODP 1241	138.31	4.847	*G. obliquus*	-1.38	3.46	24.54	0.898	37.59
ODP 1241	138.51	4.852	*G. obliquus*	-1.54	3.40	24.35	0.699	36.80
ODP 1241	138.71	4.858	*G. obliquus*	-1.74	3.22	23.74	0.372	35.49
ODP 1241	138.91	4.863	*G. obliquus*	-1.70	3.33	24.11	0.489	35.96
ODP 1241	139.11	4.869	*G. obliquus*	-1.60	3.48	24.61	0.693	36.77
ODP 1241	139.31	4.875	*G. obliquus*	-1.44	3.56	24.87	0.907	37.63
ODP 1241	139.51	4.880	*G. obliquus*	-1.69	3.50	24.67	0.615	36.46
ODP 1241	139.72	4.885	*G. obliquus*	-1.44	3.28	23.94	0.713	36.85
ODP 1241	139.92	4.890	*G. obliquus*	-1.32				
ODP 1241	140.12	4.895	*G. obliquus*	-1.34				
ODP 1241	140.18	4.897	*G. obliquus*	-1.54	3.49	24.62	0.755	37.02
ODP 1241	140.32	4.900	*G. obliquus*					
ODP 1241	140.38	4.902	*G. obliquus*	-1.54	3.84	25.69	0.978	37.91
ODP 1241	140.58	4.907	*G. obliquus*	-1.83	3.22	23.73	0.280	35.12
ODP 1241	140.79	4.912	*G. obliquus*	-1.71	3.80	25.58	0.785	37.14
ODP 1241	140.99	4.917	*G. obliquus*	-1.75	3.46	24.55	0.530	36.12
ODP 1241	141.19	4.922	*G. obliquus*	-1.72	3.22	23.75	0.394	35.58
ODP 1241	141.39	4.927	*G. obliquus*	-1.78	3.64	25.10	0.615	36.46
ODP 1241	141.59	4.932	*G. obliquus*	-1.81	3.88	25.82	0.735	36.94
ODP 1241	141.79	4.936	*G. obliquus*	-1.44	3.43	24.43	0.815	37.26
ODP 1241	141.99	4.941	*G. obliquus*	-1.63	3.46	24.54	0.648	36.59
ODP 1241	142.19	4.946	*G. obliquus*	-1.91	3.49	24.63	0.387	35.55
ODP 1241	134.08	4.737	*G. extremus*	-1.56	3.44	24.48	0.706	36.824
ODP 1241	134.28	4.742	*G. extremus*	-1.53	3.52	24.73	0.788	37.152

Site	Depth (mcd)	Age (Ma)	Species	$\delta^{18}O_c$ (VPDB)	Mg/Ca (mmol/mol)	Mg/Ca Temp. (deg. C)	$\delta^{18}O_{sw}$ (permil VSMOW)	Paleosalinity (PSU)
ODP 1241	134.48	4.746	*G. extremus*	-1.57	3.30	24.03	0.602	36.408
ODP 1241	134.68	4.751	*G. extremus*	-1.50				
ODP 1241	134.88	4.755	*G. extremus*	-1.67	3.34	24.15	0.527	36.108
ODP 1241	135.09	4.760	*G. extremus*	-1.54				
ODP 1241	135.29	4.765	*G. extremus*	-1.56	3.54	24.79	0.770	37.08
ODP 1241	135.49	4.769	*G. extremus*	-1.61	3.75	25.43	0.854	37.42
ODP 1241	135.69	4.774	*G. extremus*	-1.61				
ODP 1241	135.89	4.780	*G. extremus*	-1.72	3.51	24.72	0.596	36.38
ODP 1241	136.09	4.785	*G. extremus*	-1.64	3.43	24.44	0.618	36.47
ODP 1241	136.29	4.791	*G. extremus*	-1.44	3.50	24.66	0.863	37.45
ODP 1241	136.49	4.796	*G. extremus*	-1.65				
ODP 1241	136.70	4.802	*G. extremus*	-1.45				
ODP 1241	136.90	4.808	*G. extremus*	-1.60				
ODP 1241	137.10	4.813	*G. extremus*	-1.57				
ODP 1241	137.30	4.819	*G. extremus*	-1.59				
ODP 1241	137.50	4.824	*G. extremus*	-1.62				
ODP 1241	137.70	4.830	*G. extremus*	-1.67				
ODP 1241	137.90	4.835	*G. extremus*	-1.50				
ODP 1241	138.11	4.841	*G. extremus*	-1.50	3.34	24.16	0.699	36.80
ODP 1241	138.31	4.847	*G. extremus*	-1.63				
ODP 1241	138.51	4.852	*G. extremus*	-1.68				
ODP 1241	138.71	4.858	*G. extremus*	-1.77				
ODP 1241	138.91	4.863	*G. extremus*	-1.92				
ODP 1241	139.11	4.869	*G. extremus*	-1.89				
ODP 1241	139.31	4.875	*G. extremus*	-1.64				

Site	Depth (mcd)	Age (Ma)	Species	$\delta^{18}O_c$ (VPDB)	Mg/Ca (mmol/mol)	Mg/Ca Temp. (deg. C)	$\delta^{18}O_{sw}$ (permil VSMOW)	Paleosalinity (PSU)
ODP 1241	139.51	4.880	*G. extremus*	-1.74				
ODP 1241	139.72	4.885	*G. extremus*	-1.60				
ODP 1241	139.92	4.890	*G. extremus*	-1.36	3.09	23.29	0.658	36.63
ODP 1241	140.12	4.895	*G. extremus*	-1.19	3.43	24.45	1.070	38.28
ODP 1241	140.18	4.897	*G. extremus*		3.49	24.62		
ODP 1241	140.32	4.900	*G. extremus*					
ODP 1241	140.38	4.902	*G. extremus*		3.84	25.69		
ODP 1241	140.58	4.907	*G. extremus*	-1.80	3.22	23.73	0.310	35.24
ODP 1241	140.79	4.912	*G. extremus*	-1.72				
ODP 1241	140.99	4.917	*G. extremus*					
ODP 1241	141.19	4.922	*G. extremus*	-1.71	3.53	24.75	0.612	36.45
ODP 1241	141.39	4.927	*G. extremus*	-1.31	3.56	24.87	1.037	38.15
ODP 1241	141.59	4.932	*G. extremus*	-1.75				
ODP 1241	141.79	4.936	*G. extremus*	-1.66	3.43	24.43	0.595	36.38
ODP 1241	141.99	4.941	*G. extremus*	-1.51	3.46	24.54	0.768	37.07
ODP 1241	142.19	4.946	*G. extremus*		3.49	24.63		
ODP 1242	182.60	~1.4 (approx.)	*G. ruber*	-2.34	4.35	27.09	0.470	35.88
ODP 1242	182.84	N/A	*G. ruber*	-2.36	4.16	26.59	0.345	35.38
ODP 1242	182.89	N/A	*G. ruber*	-2.35	**4.81**	28.20	0.691	36.76
ODP 1242	183.08	N/A	*G. ruber*	-2.38	5.13	28.92	0.811	37.24
ODP 1242	183.13	N/A	*G. ruber*	-1.98	5.03	28.70	1.165	38.66
ODP 1242	183.32	N/A	*G. ruber*	-2.19	**4.57**	27.63	0.732	36.93
ODP 1242	183.80	N/A	*G. ruber*	-2.25	4.70	27.95	0.739	36.96
ODP 1242	184.04	N/A	*G. ruber*	-2.50	**4.72**	27.99	0.497	35.99
ODP 1242	184.22	N/A	*G. ruber*	-2.50	4.58	27.66	0.428	35.71

Site	Depth (mcd)	Age (Ma)	Species	$\delta^{18}O_c$ (VPDB)	Mg/Ca (mmol/mol)	Mg/Ca Temp. (deg. C)	$\delta^{18}O_{sw}$ (permil VSMOW)	Paleosalinity (PSU)
ODP 1242	184.46	N/A	*G. ruber*	-2.13	4.17	26.62	0.582	36.33
ODP 1242	184.70	N/A	*G. ruber*	-2.08	**4.53**	27.54	0.823	37.29
ODP 1242	184.94	N/A	*G. ruber*	-1.99	**4.97**	28.57	1.128	38.51
ODP 1242	185.42	N/A	*G. ruber*		**4.75**	28.06		
ODP 1242	185.61	N/A	*G. ruber*	-2.13	4.71	27.97	0.863	37.45
ODP 1242	185.85	N/A	*G. ruber*	-1.95	**4.16**	26.59	0.655	36.62
ODP 1242	186.09	N/A	*G. ruber*	-1.73	4.48	27.41	0.846	37.38
ODP 1242	186.33	N/A	*G. ruber*	-1.90				
ODP 1242	186.57	N/A	*G. ruber*	-1.63	4.47	27.39	0.842	37.37
ODP 1242	186.81	N/A	*G. ruber*	-1.88	4.35	27.09	0.630	36.52
ODP 1242	187.05	N/A	*G. ruber*	-1.73	4.11	26.46	0.548	36.19
ODP 1242	187.24	N/A	*G. ruber*	-1.81	4.35	27.09	0.700	36.80
ODP 1242	187.48	N/A	*G. ruber*	-1.79	4.07	26.35	0.565	36.26
ODP 1242	187.72	N/A	*G. ruber*	-1.64	4.37	27.14	0.580	36.32
ODP 1242	187.96	N/A	*G. ruber*	-1.60	4.47	27.39	0.472	35.89
ODP 1242	188.20	N/A	*G. ruber*	-2.07	4.15	26.56	0.229	34.92
ODP 1242	188.44	N/A	*G. ruber*	-2.07	**4.53**	27.54	0.433	35.73
ODP 1242	188.87	N/A	*G. ruber*	-1.87	**4.15**	26.56	0.329	35.32
ODP 1242	189.35	N/A	*G. ruber*	-1.87				
ODP 1242	189.56	N/A	*G. ruber*	-2.44	**4.69**	27.92	0.243	34.97
ODP 1242	189.59	N/A	*G. ruber*		4.11	26.46		
ODP 1242	190.47	N/A	*G. ruber*		**4.83**	28.25		
ODP 1242	190.95	N/A	*G. ruber*	-2.13	**4.91**	28.43	0.859	37.44
ODP 1242	191.19	N/A	*G. ruber*	-2.30	**4.77**	28.11	0.722	36.89
ODP 1242	191.43	N/A	*G. ruber*	-2.17	4.42	27.26	0.675	36.70

Site	Depth (mcd)	Age (Ma)	Species	$\delta^{18}O_c$ (VPDB)	Mg/Ca (mmol/mol)	Mg/Ca Temp. (deg. C)	$\delta^{18}O_{sw}$ (permil VSMOW)	Paleosalinity (PSU)
ODP 1242	191.73	N/A	*G. ruber*	-2.11	4.76	28.09	0.908	37.63
ODP 1242	191.97	N/A	*G. ruber*	-2.01	**4.95**	28.52	1.098	38.39
ODP 1242	192.21	N/A	*G. ruber*	-1.97	**4.83**	28.25	0.981	37.92
ODP 1242	192.38	N/A	*G. ruber*	-1.92	**4.72**	27.99	0.877	37.51
ODP 1242	192.62	N/A	*G. ruber*	-1.92	4.53	27.54	0.683	36.73
ODP 1242	192.86	N/A	*G. ruber*	-1.73	4.54	27.56	0.877	37.51
ODP 1242	193.10	N/A	*G. ruber*	-1.53	4.46	27.36	0.736	36.94
ODP 1242	193.34	N/A	*G. ruber*	-1.66	4.48	27.41	0.616	36.46
ODP 1242	193.58	N/A	*G. ruber*	-1.80	4.31	26.98	0.287	35.15
ODP 1242	193.77	N/A	*G. ruber*	-1.90	4.25	26.83	0.055	34.22
ODP 1242	194.01	N/A	*G. ruber*	-1.50	4.46	27.36	0.866	37.46
ODP 1242	194.25	N/A	*G. ruber*	-2.01	4.29	26.93	0.166	34.66
ODP 1242	194.97	N/A	*G. ruber*	-2.06	**4.23**	26.78	-0.015	33.94
ODP 1242	195.21	N/A	*G. ruber*	-1.98	3.99	26.13	0.230	34.92
ODP 1242	195.40	N/A	*G. ruber*	-2.55	4.58	27.66	-0.022	33.91
ODP 1242	196.12	N/A	*G. ruber*	-2.15	**4.16**	26.59	0.555	36.22
ODP 1242	205.94	N/A	*G. ruber*	-1.58	3.79	25.56	0.111	34.44
ODP 1242	206.38	N/A	*G. ruber*	-1.39	**4.53**	27.54	0.813	37.25
ODP 1242	208.94	N/A	*G. ruber*	-1.75	3.73	25.38	0.103	34.41
ODP 1242	209.42	N/A	*G. ruber*	-1.99	**4.81**	28.20	0.651	36.60
ODP 1242	209.90	N/A	*G. ruber*	-1.97				
ODP 1242	210.42	N/A	*G. ruber*	-1.89	4.23	26.78	0.555	36.22
ODP 1242	210.92	N/A	*G. ruber*	-1.54	4.09	26.40	0.626	36.50
ODP 1242	211.40	N/A	*G. ruber*	-1.46	4.42	27.26	0.985	37.94
ODP 1242	211.93	N/A	*G. ruber*	-1.22	4.14	26.54	0.775	37.10

Site	Depth (mcd)	Age (Ma)	Species	$\delta^{18}O_c$ (VPDB)	Mg/Ca (mmol/mol)	Mg/Ca Temp. (deg. C)	$\delta^{18}O_{sw}$ (permil VSMOW)	Paleosalinity (PSU)
ODP 1242	212.41	N/A	*G. ruber*	-1.49	3.62	25.05	0.195	34.78
ODP 1242	212.89	N/A	*G. ruber*	-1.48	3.81	25.61	0.321	35.28
ODP 1242	213.43	~1.6 (approx.)	*G. ruber*	-1.40	**4.37**	27.14	0.720	36.88